SLAC-R-611
February 2003

LCLS
THE FIRST EXPERIMENTS

September 2000

Stanford Linear Accelerator Center, Stanford, University, Stanford, CA 94309
Work supported in part by the Department of Energy contract DE-AC03-76SF00515.

Table of Contents

First Scientific Experiments for the LCLS

The Scientific Advisory Committee (SAC) for the Linac Coherent Light Source (LCLS) has selected six scientific experiments for the early phase of the project. The LCLS, with proposed construction in the 2003-2006 time frame, has been designed to utilize the last third of the existing Stanford Linear Accelerator Center (SLAC) linac. The linac produces a high-current 5-15 GeV electron beam that is bunched into 230 fs slices with a 120 Hz repetition rate. When traveling through a sufficiently long (of order of 100 m) undulator, the electron bunches will lead to self amplification of the emitted x-ray intensity constituting an x-ray free electron laser (XFEL). If funded as proposed, the LCLS will be the first XFEL in the world, operating in the 800-8,000 eV energy range. The emitted coherent x-rays will have unprecedented brightness with 10^{12}-10^{13} photons/pulse in a 0.2-0.4% energy bandpass and an unprecedented time structure with a design pulse length of 230 fs. Studies are under way to reduce the pulse length to tens of femtoseconds.

This document presents descriptions of the early scientific experiments selected by SAC in the spring of 2000. They cover a wide range of scientific fields. The experimental teams consist of many internationally recognized scientists who are excited about the unprecedented x-ray capabilities of LCLS that surely will lead to new scientific frontiers. More generally, this document serves to forward the scientific case for an accelerator-based XFEL source, as requested by the BESAC subpanel on Novel Coherent Light Sources, chaired by Stephen R. Leone.

Two general classes of experiments are proposed for the LCLS. The first class consists of experiments where the x-ray beam is used to probe the sample without modifying it, as is done in most experiments at current synchrotron sources. In the second class, the LCLS beam is used to induce non-linear photo-processes or matter in extreme conditions. The same source can be used for both types of experiments by utilizing six-orders-of-magnitude changes in photon flux density by focusing the LCLS beam, and by exploiting the strong dependence of the photo-absorption cross section on photon energy and atomic number.

The first five experiments,

- **Atomic Physics Experiments**
- **Plasma and Warm Dense Matter Studies**
- **Structural Studies on Single Particles and Biomolecules**
- **Femtochemistry**
- **Studies of Nanoscale Dynamics in Condensed Matter Physics**

are based on the design parameters of the LCLS (given in Table 1, next page) specified in the *Linac Coherent Light Source (LCLS) Design Study Report: The LCSL Design Study Group*, prepared for the U.S. Department of Energy by SLAC in 1998. Some of the experiments assume that the x-ray beam can be focused to 100 x 100 nm with 50% of full photon flux, which is today's state of the art.

TABLE 1. Design parameters of the LCLS.

Wavelength range	15 Å	1.5 Å
Peak sat. power	11 GW	9 GW
# coherent photons/pulse	2.2×10^{13}	2.2×10^{12}
Energy bandwidth	0.42%	0.21%
Pulse width (FWHM)	230 fs	230 fs

The order in which the experiments are described does not reflect their relative priority but rather indicates a thread of connectivity and dependency. All LCLS experiments involve the interaction of a high-power x-ray beam with atoms, and so the first experiment is aimed at understanding this process at a fundamental level. This basic knowledge is important for the second experiment, which uses the high power of the LCLS to create an interesting state of matter, so-called "warm dense matter," and proposes to probe it by a second delayed LCLS pulse. The third experiment is tied to the first two in that it depends on the time scale over which a biological molecule disintegrates after it is hit by the LCLS beam. Radiation damage is one of the main obstacles today in determining the structure of proteins that cannot be crystallized. The experiment is based on the use of LCLS pulses that are fast enough to determine the structure by x-ray scattering before radiation damage sets in. The fourth experiment goes to the very heart of chemistry, aiming at obtaining molecular pictures, i.e., atomic positions, bond length and angles, during chemical reactions or transformations at femtosecond time scales, an area of research previously reserved for ultrafast lasers. Finally, experiment number five pushes the envelope in probing ordering phenomena in hard and soft condensed matter on the important nanometer length scale, which cannot be seen by optical photons, over a broad range of time scales. Nanoscale dynamics is not only scientifically interesting, but it constitutes the competitive arena of advanced technological devices.

The above five experiments, even at this early proposal stage, already instill dreams of improved XFEL characteristics, for example, shorter pulse lengths. Just as the application of conventional lasers has been accompanied by R&D on lasers themselves, there needs to be an R&D program to explore new accelerator and optics concepts with LCLS. This is the goal of the sixth experiment,

- **X-ray Laser Physics.**

The history of and experience with three generations of synchrotron radiation sources has taught us that the above experiments are at best the tip of the iceberg of scientific opportunities. It is safe to predict that we have not yet thought of the most important experiments that eventually will be done with this new class of radiation sources—x-ray free electron lasers!

- Gopal K. Shenoy and Joachim Stöhr, Co-Chairs,
LCLS Scientific Advisory Committee

Atomic Physics Experiments

R. R. Freeman, *University of California, Davis, CA*
P. H. Bucksbaum, *University of Michigan, Ann Arbor, MI*
K. Kulander, *Lawrence Livermore National Laboratory, Livermore, CA*
L. Young, *Argonne National Laboratory, Argonne, IL*
R. Falcone, *University of California, Berkeley, CA*

I. SUMMARY

All Linac Coherent Light Source (LCLS) applications involve x-ray free electron laser (XFEL)-atom interactions, so understanding basic atomic physics is one of the most important early tasks. Warm dense matter starts with atomic absorption. Even the transmission, diffraction, and attenuation optics necessary to transport and condition the beam will involve basic interactions between atoms and the intense LCLS beam. The intensity and wavelength regime of LCLS place it apart from third-generation sources, and some of the x-ray science will be different. We are in a good position to estimate how basic effects like photoionization might change, but experiments are needed to confirm the calculations, to sort out the relative importance of competing processes, and to lay the foundation for any materials science experiments with the x-rays. We propose investigating this in controlled experiments, using both the focused and unfocused LCLS beam, at both design wavelengths (15 Å and 1.5 Å).

In particular, we propose five initial experiments. The first one aims to directly observe multiple core hole formation in an atom. This is a novel phenomenon that could not be addressed in the past due to limitations in x-ray flux density. The second experiment extends nonlinear optics into the x-ray regime for the first time. It involves multiphoton ionization of a K-shell electron, which can be readily observed by characteristic x-ray emission with a photon energy that exceeds the LCLS pump energy. The third experiment exploits the unique features of LCLS to produce energetic clusters with high charge states that will undergo giant coulomb explosion. This experiment is of key importance in understanding energy transfer and radiation damage of the LCLS beam in clusters, molecules and particles (see proposal on biomolecules). Advanced research topics include studies of radiation and possibly lasing from XFEL-excited matter and the formation of highly excited laser plasmas (see proposal on plasmas and warm dense matter).

II. BACKGROUND AND MOTIVATIONS

A. Proposed experimental investigations

1. Direct observation of multiple core hole formation in an atom by the LCLS beam

This is a novel phenomenon, since conditions necessary to produce multiple core holes by direct multiple photon excitation have not existed prior to the LCLS. The experimental signature for this is production of “hypersatellite” Auger electrons with energies significantly higher than those associated with single hole states.

2. Direct observation of multiphoton ionization of a K-shell electron

This would extend nonlinear optics into the x-ray regime for the first time. Here the process is identified through characteristic line radiation, where the photon energy exceeds the LCLS energy.

3. Observation of giant Coulomb explosions in atomic clusters (GCEC)

This exploits the unique features of the LCLS to produce more energetic clusters with higher charge states. Coulomb explosion energies and charge states are measured directly by observing the exploding ion fragments. Time-resolved radiation from the clusters will also be used to diagnose the cluster conditions.

Advanced research topics leading from these initial experiments include:

1) Studies of radiation and possibly lasing from XFEL-excited matter

2) Formation of highly excited laser plasmas

Details and calculations relating to these experiments will be presented in the feasibility section of this document.

B. Science justification

The LCLS produces copious numbers of photons with energies above the characteristic scale of atomic photoionization—more than an order of magnitude, in fact, above the ionization potential for any atom. Therefore, LCLS-atom interactions differ significantly from the interactions of intense optical or ultraviolet laser beams with atomic targets. Although beams of x-rays with this energy and intensity have never been produced before, we still have a pretty good idea what new physics to expect from studies with weak incoherent x-ray sources. We stress, however, that the basic physics of this regime has never been explored, and therefore verification of fundamental ideas is a paramount scientific objective. This verification will serve several immediate needs in addition to basic physics. First, it may lead to simple absolute diagnostics of LCLS beam parameters, such as intensity and coherence. Second, it will help to validate models of more complex XFEL-matter interactions in important new systems like warm dense plasmas. Last, we must understand the fundamental atomic origins of damage mechanisms and nonlinearities in beam conditioning optical elements of all kinds, including vacuum windows, attenuators, mirrors, gratings, and zone plates. Our scientific program is aimed at the basic physics of these mechanisms in single atoms and in clusters. We are concentrating on those effects that are *distinct from physics observed at third-generation synchrotron light sources*.

Photoionization of atomic inner shells with x-rays has long been studied with second- and third-generation light sources in the weak-field limit [1]. There, the photon interacts predominantly with a single electron to create a single inner-shell vacancy. Direct production of multivacancy states occurs as a consequence of electron correlation within the atom and is evident as weak satellite structure in the x-ray absorption near-edge structure (XANES) and extended x-ray absorption fine structure (EXAFS) [2]. Indirect production of multivacancy states occurs through relaxation of a core hole via Auger and shake-off processes, where either the initially created vacancy “bubbles up” successively through the outer shells or an additional electron is shaken off due to the sudden change in the core potential [3,4]. With the intensities available with the LCLS, one is able, for the first time, to control the production of *multiple* vacancies in a *specified* inner shell. This is in contrast to the usual situation, where atomic decay processes dictate the

final state of the ion. Substantial work has accumulated on the spectroscopy of atoms with multiple inner-shell vacancies due to utility of these states in plasma diagnostics and their copious (albeit uncontrolled) production via fast heavy ion impact on gases [5].

III. SCIENTIFIC OBJECTIVES

Our near-term objectives are to observe, study, and quantify a number of fundamental atomic processes, which have not been accessible at previous x-ray sources or laser light sources.

A. Single-atom inner-shell multiple ionization

Optical lasers with the intensity and pulse duration of the unfocused LCLS beam are capable of multiple ionization, and careful studies of this have revealed the presence of both sequential and nonsequential (i.e., cooperative) processes. Analogous effects will occur with the LCLS beam, with several important differences, which must be studied and verified.

- *Inner-shell multiple photoionization dominates.* The cross sections for inner-shell photoionization are typically much higher than those for the valence shell at x-ray or XUV wavelengths, so the photoionization will occur "inside-out." The photoionization rate Γ, even for the unfocused LCLS, will exceed the inverse of the pulse duration $1/\tau$ in many atoms. Therefore, a substantial fraction can be created with multiple vacancies in a single shell, that fraction far exceeding the weak-field, high-energy shake-off limit of 10^{-4}. These multiple inner-shell vacancies in complex atoms will cascade decay to extremely high charge states, for example the most probable charge state for the decay of a double K-vacancy state [KK] in argon is +8.

- *Rapid relaxation*. Since optical lasers typically ionize the valence shell, the atom is likely to be left in its ionic ground state. Studies of VUV fluorescence emission from ions formed by ultraviolet lasers at the LCLS duration and intensity have revealed that this photoionization mechanism begins to change at shorter wavelengths to favor the production of excited state ions [6]. The precise nature of the change is still a matter of controversy; explanations include coherent excitation of multiple electrons or even whole shells of electrons in the atom [6]. At x-ray wavelengths, inner-shell ionization is preferred, so excited state ions are the rule rather than the exception. The Rhodes mechanism of multiple ionization within a shell may be greatly suppressed, however, due to the tendency towards Auger relaxation, which typically occurs in 0.1 fs. Therefore, studies that are sensitive to the competition between multiple excitation and rapid relaxation are of utmost importance.

- *Coherent multiphoton effects*. Nonlinear optics has always been the province of lasers, but the LCLS will present some new challenges and opportunities to study nonlinear effects in inner cores of atoms. Furthermore, if we can find a simple nonlinear effect to study, this could be a simple and reliable diagnostic of some of the temporal properties of the beam. Perhaps the easiest physical phenomenon to observe is two-photon photoionization. This is nonresonant, so the precise wavelength of the XFEL is relatively unimportant. It also has a very simple and easily observed signature: the production of characteristic x-rays from the atom at an energy *greater* than the XFEL is proof of energy pooling of the laser photons. This effect could even be observed with a small branching ratio and in the presence of considerable background.

- *Inversion of ordinary materials.* The second revolution in laser technology occurred in the early 1970s, when it was appreciated that the workhorse nitrogen and ruby lasers could be used as the excitation source to produce more exotic lasers. The LCLS presents the opportunity for

serious studies of x-ray laser mechanisms in many materials, where this form of energy deposition and transport may be important. The reason is that LCLS excitation produces a natural inversion, since ions are almost never produced in their ground electronic states. Careful studies of the fluorescence and Auger emissions should reveal the conditions necessary to reach lasing thresholds in these systems.

- *X-ray lasers.* We can expand studies of inversion and threshold to full-blown investigations of laser-pumped x-ray laser systems at the LCLS.

B. Molecular and cluster effects

Laser-cluster interactions have been fruitful sites of new physics and physical chemistry over the past decade. Experiments on rare gas clusters illuminated by lasers with pulse duration and intensity comparable to the *focused* LCLS revealed rapid charging and heating of the clusters, followed by disassembly in a Coulomb explosion [7]. The clusters are themselves very bright and short sources of x-ray radiation. In addition, the high energy of the exploding fragments has enabled experiments on table-top fusion and may have additional applications as well [8]. The LCLS will be a unique tool for cluster research because of the very high probability for multiple ionization of the cluster atoms and the high energy of the departing ions. If the average Auger multiplicity is two electrons per ion, then we expect a xenon atom to be ionized about ten times during the pulse for a 15 Å laser.

C. Generalization to materials damage

Fundamental work on atoms and clusters can be generalized to studies of damage in bulk materials. The general experimental chamber that we will need for the atomic physics could be modified to study the mechanisms for energy deposition and energy transport in condensed phase materials, and the data collected would be useful for designing optical elements for the beam or finding the correct conditions for plasma experiments.

D. Plasma formation

The multiple ionization and hot electron generation lead to unique plasma conditions. Simulations of warm dense plasmas will benefit from energy and multiplicity data collected in our experiment, and we place a high priority on providing this for other experiments at the LCLS.

E. Anticipated impact

The results of our studies will provide critical data for the design of any future experiments involving laser-matter interactions at LCLS intensities. We can envision no serious attempt to develop this x-ray science without a program on fundamental laser-atom interactions. In addition, several areas of atomic physics will benefit. First, the whole field of collective excitation of atomic electrons by lasers will become much more clear through the addition of LCLS data at 15 Å. We will certainly shed light on, if not resolve, the controversy about the mechanism for collective excitation seen at 248 nm. The field of cluster dynamics will also enter a new regime with our experiments. X-ray lasers may be studied in much greater detail than previously, where they could only be produced at relatively long wavelengths or at short

wavelength using NOVA-class lasers. And finally, we expect to validate many of the assumptions of wavelength scaling in multiphoton laser-atom physics.

The LCLS is a *unique* tool for most of these studies. Its combination of intensity, coherence, wavelength, and pulse duration, cannot be duplicated with other laboratory sources.

IV. EXPERIMENTAL DETAILS

A. Feasibility assessment

1. Experiment 1: Multiple core hole formation

Multiple core hole formation will be observed in a gas target of neon. The atomic requirement is a relatively high photoionization cross section, simple noncorrosive monatomic target. We choose the neon K-shell for the first test because of the relative simplicity of its spectroscopy [5,9] and the wealth of information available on photoionization in the weak-field limit [10-12] but emphasize that the concepts are applicable to all atoms. The physical process is pictured as follows: Two photons are sequentially or simultaneously absorbed by the K-shell of neon to form two vacancies within a time scale shorter than the relaxation time (τ_{Auger} = 2.5 fs). Nonradiative (Auger) relaxation dominates the radiative channel at low Z and in neon by a factor of 100. Thus, starting with a single K vacancy, KLL Auger decay produces primarily Ne^{2+}, as observed in earlier work where it was 94% of the yield [13] with a 6% branch to the Ne^{3+} due to double Auger decay processes, KLLL. By analogy, a double K vacancy state would produce Ne^{4+} as a clean and detectable signature.

Energetically, production of a double K vacancy state is not allowed by single photon absorption at energies near the K-edge. There is an energy threshold for production of multiple K holes that is somewhat higher than twice the K-binding energy. For neon, the threshold for ejection for the second electron via a sequential ionization is estimated from the tables of Maurer and Watson [5] to be 993 eV. Thus, one may be able to distinguish a simultaneous vs. a sequential multiple ionization process by its photon energy dependence. For a simultaneous process, it may be sufficient for the photon energy to be (870 + 993)/2 = 932 eV, whereas for a sequential process one would assume that the photon energy would have to exceed the highest photon energy required, 993 eV. Ion yields via time-of-flight spectroscopy would be a simple diagnostic, if the direct ionization channel dominates, as is the case with the focused LCLS beam. (At high photon energies (40 times K binding energy), the probability of [KK] production approaches the high-energy shake-off limit, 6 x 10^{-4}.) Recent measurements using the cold target recoil ion momentum spectroscopy technique on supersonic jets of neon to study multiple-ionization mechanisms of optical high-intensity lasers may eventually be useful to delineate detailed mechanisms [14].

In practice, it is difficult to produce cleanly a single K vacancy with photon excitation at energies where [KL] vacancies are possible, in neon for E> 915 eV. The primary photoexcitation produces [KL] as an energy-dependent branch of up to 10%, which in turn produces a background of 0.5% of Ne^{4+}. When [KK] is not dominant (unfocused beam as shown in Table 1 below), electron spectroscopy is preferable because the hypersatellite transitions due to [KK] are well separated from the "satellite" transitions due to [KL] and diagram lines due to [K]. For [KK] in neon, the energies of the hypersatellite Auger transitions range from 812-880 eV [15], whereas the diagram and satellite transitions range from 730-806 eV [10].

These can be easily distinguished in a standard energy-dispersive electron spectrometer. One option is to scan a cylindrical mirror analyzer electron spectrometer with $\Delta E/E_{pass}$ = 2%, E_{pass} =

100 eV; collection efficiency = 1%, for an overall collection/detection efficiency of 0.5% at a resolution of 0.25% for 800 eV kinetic energy electrons. Drawbacks include no simultaneous detection of multiple energies and limited angular information, as all azimuthal angles are detected. Advantages are easy setup and versatile energy range. Another option is an energy-dispersive spherical sector spectrometer equipped with a position-sensitive detector. Here the collection efficiency is 4×10^{-5} for a resolution 0.35%. Drawbacks include more complex setup and smaller collection efficiency. Advantages include angular resolution and multiplex energy detection. For the unfocused beam and an event rate of up to 7.5×10^{7} /pulse, one obtains 3000 counts/pulse over the entire energy range in the spectrometer from [KK] production. Note that these high rates are achievable only because the neon target density can be very high without cluster formation. The densities for heavier rare gases would need to be scaled down by factors of 10 to 1000.

If we focus the beam (demagnification factor of 3×10^{4}), we easily saturate the transition and the photoionization rate will exceed the Auger decay rate. The hollow atom component will be predominant rather than the small fraction (10^{-4}) that is typically observed with weak-field synchrotron radiation. The field strength (2000 V/Å) will be comparable to the binding energies of the core electrons. At intermediate intensities, as would be achievable with suitable beam attenuators, the field strengths could be made comparable to valence electrons, and one may observe recapture of a slow outgoing K-electron by the field and rescattering on the 2p valence shell of neon to produce multiple ionization. Complex mechanisms could be operative; electron and ion spectroscopy would be needed to identify the final states in the interaction. Theory would be needed as a guide. In any event, a wealth of intriguing multiple electron dynamics await discovery in this new regime of high-field, short-wavelength interactions with atoms.

TABLE 1. Parameters of the unfocused and focused beam.

Parameter	Unfocused (10 μm x 30 μm)	Focused (100 nm x 100 nm)
LCLS energy range	850-1000 eV	850-1000 eV
Photons/pulse	2×10^{13} γ/pulse	1×10^{13} γ/pulse
Beam area	3×10^{-6} cm^2	1×10^{-10} cm^2
Pulse width	233 fs	233 fs
LCLS intensity	2.9×10^{31} γ/s/cm^2	4.3×10^{35} γ/s/cm^2
Ne photoionization σ (K edge, 14.2 Å, 870 eV)	3×10^{-19} cm^2	3×10^{-19} cm^2
Instantaneous ionization rate/atom	10^{13}/s	1.3×10^{17}/s
Auger relaxation rate	4×10^{14}/s	4×10^{14}/s
Probability per atom for multiple ionization during relaxation time	2.5×10^{-2}	1
Density of pulsed jet target 1 mm from nozzle	1×10^{16} /cm^3	1×10^{16} /cm^3
Interaction volume (area x length)	3×10^{-7} cm^3	10^{-11} cm^3
Number of atoms experiencing direct multiple core hole formation	7.5×10^{7}/pulse	10^{5}

2. Experiment 2: Multiphoton ionization

Nonresonant two-photon photoionization of the L-shell will be observed in atomic krypton near the threshold for this transition, at 850 eV. Either the x-ray or Auger emission from n=3 to n=2 can be detected, at an energy of about 1.5 keV. This is well above the energy of any photons or electrons that can be produced from single-photon absorption or scattering of the LCLS beam, so it is a very clean signature. However, background from higher energy photons (third-order free electron laser and spontaneous emission) must be minimized. Here are the results of some simple calculations: The two-photon absorption cross section can be estimated from the fact that the matrix element involves two dipole couplings divided by a dephasing rate. The latter is dominated by the energy mismatch between the photon energies and the resonant state splittings, which are different by approximately a factor of two.

Let us try to be semiquantitative about this. I estimate the two-photon cross section as:

$$\sigma_{2\gamma} \sim \sigma_\gamma^2 \tau \sim (10^{-18})^2(10^{-17}) = 10^{-53}\text{cm}^4\text{s, and}$$

$$\Gamma_{2\gamma} = \sigma_{2\gamma} I^2 = (10^{-53}\text{cm}^4\text{s})(10^{31}\gamma/\text{cm}^2\text{s})^2 = 10^8 \text{s}^{-1}.$$

In one pulse we have 2 x 10^{-5} two-photon absorptions per atom, or about two million of these unusual events per shot for a target thickness of 10^{11} atoms. The events could either be detected through the Auger decay channel in an energy-dispersive electron spectrometer or through the x-ray channel using a variable-line spaced grating spectrograph. Although the branching ratio of $\Gamma_{Rad}/\Gamma_{Auger}$ is only 0.02 for the Kr L-shell, simple solid-state detectors can be employed to detect the radiation. For the x-ray channel, assuming a typical acceptance-limited efficiency of 10^{-4}, we should be able to detect 4 photons per laser pulse. For the Auger channels, assuming an acceptance limited efficiency of 4 x 10^{-5}, we should be able to detect 80 electrons per laser pulse. If the focused beam were employed, the two-photon absorption rate, αI^2, would increase by 10^8.

Resonance-enhanced two-photon absorption can also be observed if the LCLS output can be set at the appropriate energy. Resonant structure in two-photon absorption is well known in valence shell spectroscopy, with enhancements of many orders of magnitude. The analogous enhancement is expected and predicted for inner-shell transitions in atomic neon [16]. Resonance structures corresponding to 1s $\rightarrow$ 2p, 3p, 4p in neon between 840 and 870 eV are predicted to rise 2 to 15 orders of magnitude above the nonresonant background of 10^{-55} cm^{4}s. The two-photon absorption rate would increase in proportion to the cross section and decrease due to mismatch of the bandwidth of the LCLS radiation with the line shape of the resonance ($\alpha(\Delta E_{LCLS}^2 + \Delta E_{transition}^2)^{-1/2}$, which is a factor of 10^{-1} for neon 1s excitation). For these transitions, the signature of two-photon absorption would be photoelectrons at the appropriate kinetic energy, which, unlike the nonresonant transitions in Kr above, is near the photon energy. These would need to be distinguished by relatively high-resolution electron spectroscopy as is possible using the equipment described above. However, we should note that one expects resonant structure in Kr L-shell two-photon absorption, 2p $\rightarrow$ np, nf transitions, and these will have signature electrons at energies far above the photon energy. These resonant structures may be important for future applications of the LCLS as the two-photon rate can exceed the one-photon rate for the quoted intensities.

3. Experiment 3: LCLS proposal to observe GCEC

The LCLS will present a serious problem to all of its users, a problem inherent in its usefulness: it will deposit large amounts of energy on surfaces of materials in very short times. Common

experience with high-powered light sources of other types suggests that, on surfaces of materials, damage will be a constant concern. The science of material damage by high-intensity light is in its infancy, even with the advent of serious use of lasers in material processing.

The mechanism of material damage is presumed to be ionization-initiated electron seeding followed by avalanche breakdown within the absorption depth of the light. Just how this happens and the controlling factors are now only poorly understood. It is the purpose of this series of controlled experiments to understand the role of the generation of fast electrons during ionization and their consequences. In Experiments 1 and 2 of this proposal, we have discussed the study of how the inner shells control the energy distribution during ionization. In this experimental campaign, we propose to systematically study the impact of released charges upon otherwise ordered, neutral matter.

To construct a quantifiable experiment, we will generate, using recently developed super cooling and expansion nozzles, clusters of xenon atoms that will be controlled in size from a few thousand, up to nearly 10^{12} . These clusters will be produced in the same apparatus as that used in Experiments 1 and 2, and the mass spectrometers will be appropriately adjusted to analyze the resulting fragments when the clusters are broken apart by the ionization process.

The unique characteristics of the LCLS light play a pivotal role here.

- The number of useful photons is enormous: between 10^{12} and 10^{13} photons/pulse.
- The time duration is small (200 fs) yielding a peak flux of nearly 10^{25} photons/sec/(10 x 30 μm)^2 ~ 10^{31} photons/sec/cm^2 unfocused.

Since ionization cross sections for the heavier elements at 15 Å are on the order of 10^{-19} cm^2, during the pulse time of 200 fs, each atom exposed to the unfocused beam will undergo approximately (10^{31} x 10^{-19} x 10^{-13}) ~ 1 ionization event. That is, the ionization will saturate. Now, each atom is being ionized from an inner shell, with the dominant relaxation mechanism due to Auger recombination. Thus, each ionized atom creates two or more electrons in the unfocused beam. (We point out here that, if we focus the LCLS beam to 0.01 μm, then each atom in the cluster will be classically ionized nearly 10,000 times over. What is unique about this situation is that the atom will continue to ionize, since the Auger rates (~ 0.1 fs) are nearly 1000 times faster than the ionization rate. Thus, each atom will ionize until it strips down to the core level of the initial ionization event.)

A ball of charge is produced that contains on the order of 10^9 nuclei that are at least in the first ionization stage. This will represent a plasma of sufficient density that no optical photon could have penetrated to have produced it in the first place. But since the LCLS is lasing at 15 Å, the ball is easily penetrated and completely ionized.

The ionized electrons are created with Auger energies (at least several kilovolts) and many of them escape, resulting in a positive Coulomb ball, before the electrostatic potential grows strong enough to hold them back. If the ball is assumed to have a radius of 10^{-5} cm, then electrons will leave until the electrostatic potential of the uncovered positive ions rises to several kilovolts at that radius. This will occur for net positive charges of approximately 10^9. This is a net charge of 10^{-10} Coulombs. The resulting ball will explode in a unpredictable manner, but one that is guaranteed to produce fast nuclei. It is this mechanism that we wish to investigate and that constitutes the fundamental process by which damage occurs on surfaces during irradiation by high-intensity x-rays.

4. LCLS operations needs

This proposal is designed to investigate the inner core ionization mechanisms of atoms during extremely high-intensity, single-photon irradiation. The investigations described under III. Scientific Objectives are all experiments requiring the measurement of rare events in the presence of a large background. To accomplish this, we are requesting that:

- The LCLS beam parameters be set to the 15 Å nominal wavelength. This choice is mandated by the substantially larger inner-shell ionization cross sections at 15 Å than at 1.5 Å. The planned experiments do not require any on-line tunability of output wavelength, although we would like to be able to acquire data at several specified energies to observe above and below threshold effects.
- The first-order undulator radiation be isolated from the third-order radiation and the spontaneous background. This could be accomplished with a pinhole to eliminate the spontaneously radiated halo followed by a grazing-incidence mirror such that the angle of incidence is less than the critical angle for the first harmonic and greater for the third harmonic.
- The beam optics in this experiment line be capable of operation either unfocused, where much of what is proposed can be performed, yet capable of being focused to at least a minimum spot size of 0.1 μm. We point out that should the beam be capable of focusing to 0.01 μm, complete saturation of the Compton cross section would be possible. These proposed experiments have estimated cross sections that are at least 10^4 larger than the Compton cross section.
- The experimental apparatus be in a position relative to the LCLS that the unfocused beam size is on the order of 10 x 30 μm. The LCLS parameter specifications suggest that this mandates having the apparatus within meters of the LCLS output port, since this experiment will require the maximum flux available on the LCLS and will be executed in a high-vacuum environment. At 15 Å, it is not clear at this point how to isolate the experimental vacuum vessel from the LCLS vacuum. Since the apparatus has to be placed close to the machine to obtain the required flux, the proposed vacuum connection to the LCLS will have to be carefully designed to mitigate the effects of vacuum failures within the experimental region.
- The pulse width be made as short as possible. Although our calculations show that these proposed experiments can be successful at the current LCLS design parameter of 233 fs, the probability of gaining higher quality data increases in direct proportion to the decrease in the pulse length of the 15 Å light.

5. Instrumentation needs

The basic instrumentation needs for this experiment are built upon the requirements for any atomic physics experiment that attempts to measure the resultant photon/electron/ion yield after the interaction of a photon beam with atoms. The difficulty here and what distinguishes it so dramatically from previous ionization-type experiments, is the short-wavelength nature of the radiation, the large instantaneous flux of photons, and the need to measure particles and photons in a time-gated fashion in synchronization with the light from the LCLS.

- An effective beam attenuator, perhaps along the lines described in the LCLS design study report, will have to be fielded and tested. Our experiment requires the ability to control the total flux delivered to the target chamber on-line. There is no need to adjust the intensity on a shot-by-shot basis. Instrumentation that accompanies this attenuator is a diagnostic of the

total flux entering the experimental chamber, which is highly reproducible. This instrument will need the essential characteristic of measuring the total flux without generating unwanted ionization within the experimental vessel.

- A trigger system, based upon fluorescence or charge detection from the LCLS beam itself, must be developed. This device must have high-temporal resolution (~ 100 fs), stability, and yield no unwanted photons or charged particles. Earlier generations of these kinds of devices are well known, though their implementation in this environment has not been demonstrated.
- Gated, dispersive x-ray detectors are needed that are capable of measuring x-rays in the range of 100 eV-15 keV. These devices, the first several generations of which have been developed by U.S. Department of Energy (DOE) laboratories, would need to have time resolution on the order of picoseconds and trigger stability with the LCLS pulse.
- For the fastest x-ray measurements, either or both an x-ray streak camera and time-correlated x-ray photon counting electronics will be required. These instruments are crucial for the detection of the signature x-ray emissions in the presence of large scattered x-ray backgrounds.
- Precision, gated electron and ion detectors, with energy resolution and high background rejection, are needed. Again, much of this technology exists in the DOE laboratories but will need upgrading and modification. The electron detectors, for example, must be capable of measuring electrons with energy of 10 to 1000 eV with a resolution 2%. The time gating, timed by the LCLS pulse, is necessary to discriminate against unwanted background electron sources.
- This experiment will confront directly a problem inherent to all of the experiments on the LCLS that attempt to measure scattered x-rays of charged particles: The beam from the LCLS will be of such a short wavelength and so intense that, even if a small fraction of the beam hits any portion of the experimental apparatus (including the entrance and exit ports), the chamber will be swamped by background events. Thus, an explicit program to develop beam transport and dumping of precision heretofore never attempted must be initiated.
- The experimental apparatus will be a large volume, ultrahigh vacuum vessel with state-of-the-art differential pumping systems to accommodate the pulse gas nozzle for the production of atoms and clusters synchronized to the LCLS beam. The efficient, high-throughput pumping system will be necessary to ensure reduced background ionization events and to permit the anticipated direct vacuum connection to the LCLS proper.

6. R&D in support of construction

The needs for R&D for this experiment come in two distinct categories: 1) modeling/calculations and 2) a laboratory-based laser-plasma facility for instrument development.

The need for calculations (relativistic, Hartree-Fock) are necessary for the accurate prediction of the energies of ejected electrons in the cases of interest and of the precise wavelength of the signature x-rays of the processes under investigation. This experiment will be difficult under the best of circumstances, so having an accurate map of the expected energies and wavelengths of marker events will be important. The capability of this kind of modeling and calculation exists on the supercomputers of the DOE laboratories, and several of our team are experts in this arena. Support for their time to perform and analyze these results is an important ingredient for this experiment.

The experimental program has enough new technology (in addition to the LCLS itself), with enough systems integration of sophisticated detectors, that an experimental set up demonstration is all but required. We propose that a laboratory-scale, laser-plasma source of 15 Å x-rays with essentially the same pulse length structure and repetition rate as the LCLS be built. The source would make use of the new generation of high repetition rate, high average power, subpicosecond visible lasers to produce 15 Å radiation from heavy materials. Much work over the years has shown that the length of the light pulses emitted from these plasmas can be made as short as those expected from the LCLS, so we can test our photon counting, x-ray streak cameras, electron energy analyzers, and timing equipment. Naturally we cannot expect to research the high-intensity ionization phenomenon itself with this apparatus, but we can greatly mitigate the experimental risks associated with the LCLS experiment.

V. REFERENCES

[1] V. Schmidt, *Electron Spectrometry of Atoms using Synchrotron Radiation* (Cambridge University Press, New York, 1997).

[2] M. Deutsch and M. Hart, Phys. Rev. A **29,** 2946 (1984).

[3] M.O. Krause, M.V. Vestal, W. H. Johnson, and T.A.Carlson, Phys. Rev. **133,** 385 (1964).

[4] A.G. Kochur, V.L. Sukhorukov, A.I. Dudenko, and Ph.V. Demekhin, J. Phys. B **28,** 387 (1995).

[5] R.J. Maurer and R.L. Watson, At. Data Nucl. Data Tables **34,** 185 (1986).

[6] K. Boyer and C.K. Rhodes, J. Phys. B **18,** L633 (1994).

[7] T. Ditmire, J.W.G. Tisch, E. Springate, *et al.*, Nature **386,** 54 (1997).

[8] T. Ditmire, J. Zweiback, V.P. Yanovsky, *et al.*, Nature **398,** 489 (1999).

[9] D.L. Mathews, B.M. Johnson, and C.F. Moore, At. Data Nucl. Data Tables **15,** 41 (1975).

[10] M.O. Krause, T.A. Carlson, and Moddeman, J. Phys .(Paris) Colloq. **32,** C4 (1971).

[11] T.A. Carlson and M.O. Krause, Phys. Rev. **140,** A1057 (1965).

[12] N. Saito and I.H. Suzuki, Phys. Scr. **45,** 253 (1992).

[13] A.G. Kochar, A.I. Dudenko, V.L. Sukhorukov, and I.D. Petrov, J. Phys. B **27**, 1709 (1994) and refs. therein.

[14] R. Moshammer *et al.*, Phys. Rev. Lett. **84,** 447 (2000).

[15] M.H. Chen, Phys. Rev. A **44,** 239 (1991).

[16] S. Novikov, J. Phys. B, in press (2000).

Plasma and Warm Dense Matter Studies

R. W. Lee, R. C. Cauble, and O. L. Landen, *Lawrence Livermore National Laboratory, Livermore, CA, USA*
J. S. Wark, *Oxford University, Oxford, UK*
A. Ng, *University of British Columbia, British Columbia, Canada*
S. J. Rose, *Rutherford Appleton Laboratory, Chilton, Oxon, UK*
C. Lewis and D. Riley, *Queen's University Belfast, Belfast, Northern Ireland*
J.-C. Gauthier and P. Audebert, *Laboratoire pour l'Utilisation des Lasers, Paris, France*

I. SUMMARY

The construction of a short-pulse, tunable x-ray laser source will be a watershed for plasma-based and warm dense matter research. The areas we will discuss below can be separated broadly into warm dense matter research, laser probing of near solid density plasmas, and laser-plasma spectroscopy of ions in plasmas.

The area of warm dense matter refers to that part of the density-temperature phase space where the standard theories of condensed matter physics and/or plasma statistical physics are invalid. Thus, warm dense matter refers, on the one hand, to states from liquid to greater than solid density with temperatures comparable to the Fermi energy. On the other hand, it also refers to those states of matter that are plasma-like, but are too dense and/or too cold to admit to standard solutions used in plasma physics. This is the region where plasmas become strongly coupled so that perturbation approaches fail, as no small expansion parameters exist. Moreover it is the region where the temperature of a solid nears or exceeds the Fermi temperature, thus indicating the failure of standard cold condensed matter approaches. Warm dense matter, therefore, defines a region between solids and plasmas, a regime that is found in planetary interiors, cool dense stars, and in every plasma device where one starts from a solid, e.g., laser-solid-matter-produced plasma, as well as all inertial fusion schemes. Experiments in the warm dense matter regime represent the most straightforward application of the Linac Coherent Light Source (LCLS), as it uses the beam to directly serve as the heating mechanism in a manner that is elegant yet unachievable with other sources.

The study of dense plasmas has been severely hampered by the fact that laser-based methods have been unavailable. The single most useful diagnostic of local plasma conditions, e.g., the temperature (T_e), the density (n_e), and the ionization (Z), has been Thomson scattering. However, the fact that the critical electron density where visible light will not propagate is ~ 10^{22} cm^{-3} indicates that all dense plasmas cannot be probed. The LCLS will remove this impediment by making high-density plasmas accessible for the first time. Moreover, as plasma becomes denser, one reaches regimes where ideal plasma theories break down and this will certainly occur in cool dense plasmas. Thus, by probing different scattering angles one can move from noncollective to collective regimes where plasma theory remains to be tested.

Laser-based plasma spectroscopic techniques other than Thomson scattering have been used with great success to determine the line shapes of atomic transitions in plasmas, study the population kinetics of atomic systems embedded in plasmas, and look at redistribution of radiation. However, as with Thomson scattering, the possibilities end at plasmas with electron densities >

10^{21} since light propagation through the medium is severely altered by the plasma. This will change when the LCLS becomes available. The entire field of high-Z plasma kinetics from laser-produced plasma will then be available to study with the tunable source. As an example, one can study the underlying mechanisms that are currently used to produce soft x-ray lasers. Probing the kinetics of ion stages to test the gain of a potential laser scheme represents one of the most exacting tests of our ability to understand the kinetics of ions embedded in plasmas.

All of these areas will be discussed below with a view to explaining the difficulties of, and providing an outline for, plasma-based experiment at the LCLS.

II. BACKGROUND

Since the late 1960s plasma-based research has moved toward higher density regimes. The advent of laser-produced plasmas and laser-based plasma diagnostics has fueled interest in the formation of plasmas at densities nearing solid density. There are two separate areas where LCLS can play a critical role in moving this field substantially forward. The first is in the area of warm dense matter research, while the second is in the area of plasma spectroscopic techniques that will be made possible.

We note that whether we are interested in creating warm dense matter, performing Thomson scattering, or probing a plasma, the LCLS provides a major advance on any capability that exists with third-generation sources. The key to the advance is the tunable, narrow-band x-ray source with a very short pulse duration. Since the individual pulse intensity is the essential quantity for all the plasma-based research, the comparison of the LCLS to current synchrotron sources is best summarized by comparing peak spectral brightness. Indeed, one finds a 10-order-of-magnitude enhancement that will make the LCLS a successful source for plasma-based research. The utility of the high repetition rate of other sources, e.g., the Advanced Photon Source or the European Synchrotron Radiation Facility, are not useful here since we require a single photon pulse to either heat, scatter, or probe matter that is transient. Indeed, the creation of solid matter that is at a temperature greater than 1 eV while not expanding requires the LCLS.

Further, to measure the Thomson signal in a dense plasma or the warm dense matter regime requires a Thomson probe, here the LCLS, with a temporal duration that is short compared to the evolution of the system but long enough to probe the plasma collective modes. The LCLS, with a nominal 200 fs pulse duration, will be able to probe the electron feature arising from the collective behavior of the electrons. For an electron density of 10^{22} cm^{-3} one finds that 1 fs is sufficient for collective response. However, the ion collective behavior will take on the order of 100 fs leading to the possibility that the collective ion acoustic modes will not be sampled appropriately. The evolution of the system will proceed on the order of a picosecond. This indicates that any probe of the system must have a pulse duration on the ps time scale. As will be seen below, the LCLS makes this possible,

Finally, the spectroscopic probing of high-energy-density plasmas requires a short-pulse, high-energy source. For the source to be useful as a spectroscopic probe requires a spectrally tunable source for which the number of photons per mode must be on the order of unity. The photons per mode measure the probe' s ability to dominate a radiative transition, which is required to provide observable signal. Due to the high peak brightness the LCLS is extremely well matched to this task.

Thus, in all the proposed plasma-based research, the LCLS will provide an important new advance on the existing sources. Where we are currently scratching the surface, the LCLS will open the way for in-depth study of both high-energy-density plasmas and warm dense matter.

A. Warm dense matter

The LCLS, with its short-duration pulse containing a substantial number of high-energy photons, can be used to generate solid matter at temperatures of 10 eV, i.e., warm dense matter. The interest in the warm dense matter regime arises because in dense plasmas the atoms and/or ions will start to behave in a manner that is intrinsically coupled to the plasma. That is, the plasma starts to exhibit long- and short-range order due to the correlating effects of the atoms/ions. This intriguing regime, where the plasma can no longer be considered a thermal bath and the atoms are no longer well described by their isolated atom behavior, provides a tremendous challenge to researchers. In the limit of dense cool plasmas one obviously arrives at the threshold of condensed matter. Here the problem has changed from a perturbative approach to ground-state methods where complete renormalization of the atom/ion and its environment is essential.

From the prospective of plasma studies the defining quantity is the coupling parameter Γ, which is the ratio of the interatomic potential energy to the thermal energy given by the equation:

$$\Gamma = \frac{Z^2 e^2}{r_0 kT} \ ,$$

where Z is the ion charge and r_o is the interparticle spacing given in terms of the electron density n_e as:

$$r_0 = \left(\frac{3Z}{4\pi n_e} \right)^{1/3} .$$

The regions of interest span the density-temperature phase space going from modestly coupled (Γ 1) to strongly coupled ($\Gamma > 1$), while bridging the transition regimes between solid to liquid to plasma.

In Fig. 1 we show schematically the region of the temperature-density plane where warm dense matter studies are important. Here we show the temperature (T) in eV versus the density (ρ) in g/cm^3 both for hydrogen, a low Z element, and aluminum, a moderate Z element. The region where the theoretical uncertainties are largest are those where the standard theoretical approaches fail and experiments are exceedingly difficult. These areas are broadly indicated by the blue-gray overlay. Thus, we can understand that the difficulty arises theoretically from the fact that this is a regime where there are no obvious expansion parameters, as the usual perturbation expansions in small parameters used in plasma phase theories are no longer valid. Further, there becomes an increased importance on density dependent effects, e.g., pressure ionization, as the surroundings start to impinge on the internal structure of the ion or atom. Experimentally, the study of warm dense matter is difficult, as the isolation of samples in this regime is complicated. Indeed, although the plasma evolution of *every* ρ-T path that starts from the solid phase goes through this regime and plays an important role in its evolution, trying to isolate warm dense matter remains a major challenge.

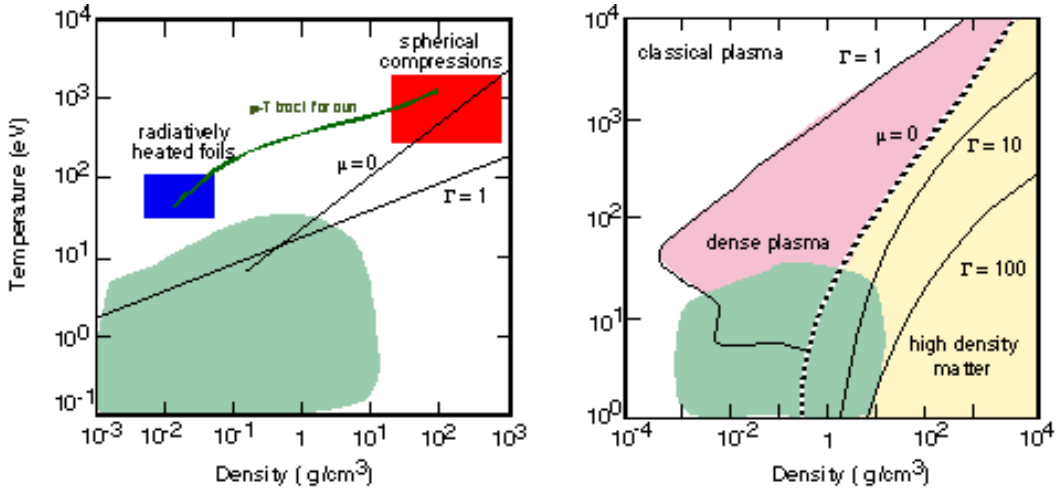

FIG. 1. The temperature-density phase diagram for hydrogen on the left and aluminum on the right. The relevant regimes are noted, as are the various values of the coupling Γ. The regions of greatest uncertainty are roughly noted as the green areas. Also indicated is the region where degeneracy will become important: it is the region to the right of the line where the chemical potential μ = 0.

The study of warm dense matter offers the possibility of exploring new frontiers in diverse areas, including strongly coupled plasma physics, high-temperature condensed matter physics, planetary science, and astrophysics, as well as high-pressure chemistry. Moreover, in many areas of research the transition from a cold dense solid to tenuous hot plasma occurs in a time-dependent manner, being important to the physical description of the system and its evolution. Examples are numerous, with the most obvious being the density– temperature (ρ-T) track of inertial fusion targets, laser-produced plasma sources, and shock-heated systems.

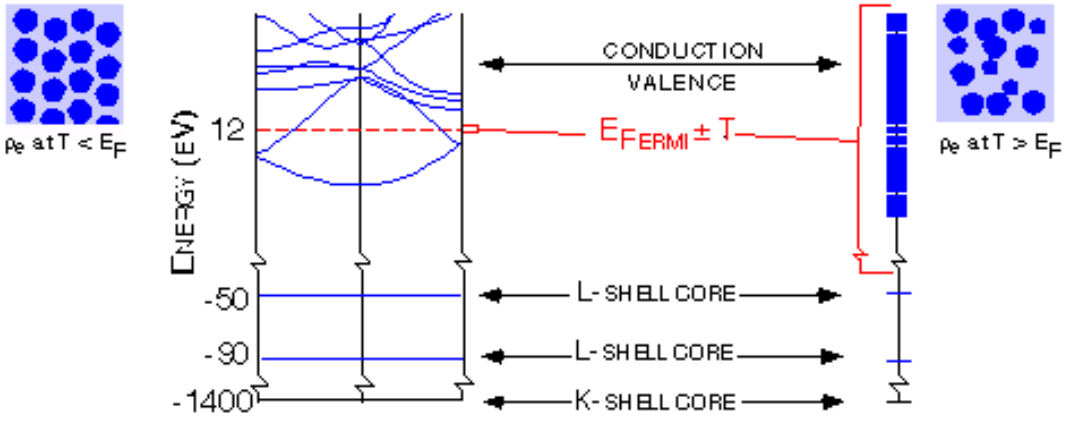

FIG. 2. A schematic energy-level diagram indicating the difficulties with treating the warm dense matter regime. The electron density distributions, ρ_e, for both low and high temperature relative to the Fermi energy is shown on the upper left and right, respectively.

However, from a condensed matter perspective, strong coupling is not the relevant measure, as the matter is fully structured and correlated. In a condensed matter system the issue becomes the

temperature of the system relative to the Fermi energy, E_{Fermi}. In the case where the $T < E_{Fermi}$, the normal methods of condensed matter theory will work, as only a few valence/conduction bands need to be taken into account. However, when $T > E_{Fermi}$ the number of bands that are required to describe the system become enormous. In addition to the sheer number of bands, one must also include both excited core states and ionized species in the description, as multiple species are required. This is shown schematically in Fig. 2.

The importance of warm dense matter studies is threefold.

• First, with new experimental sources such as the LCLS, we will be able, for the first time, to probe the warm dense matter regime. Thus, a field of research that was once daunting will be turned into fertile ground for exciting research at the leading edge.

• Second, with the advance of theoretical methods future predictions will be made that will require verification by experimental data. Thus, progress will only be possible in this complex regime when theory and experiments can be compared.

• Third, there are important mission-oriented research requirements, e.g., astrophysical- and weapons-related studies, that come directly into the area of warm dense matter. Indeed the regimes of largest errors and uncertainties in many of the applied research areas of, for example, chemistry and physics come in the warm dense regime.

To provide an overview of this new field we now outline some of the critical issues in obtaining information in the regime of warm dense matter.

First, the data we expect to obtain from warm dense matter experiments are mainly equation of state (EOS) data. The equation of state is a thermodynamic description of matter—pressure-density-temperature—that is a description of how matter reacts to any change in one of those three variables. The EOS is, in effect, a description of matter; it is the component of a problem that specifies, e.g., whether one is using uranium or air. There are regimes where we believe that we can accurately depict the EOS of a material. For instance, an ideal gas, possibly with plasma effects, describes extremely high-temperature matter; condensed matter theory works well for normal room-temperature conditions; Thomas-Fermi theory describes extreme densities. Warm dense matter, on the other hand, is in the complex regime in the middle. Note that the topics that affect the EOS are precisely those that affect the microscopic description of matter. Thus, the populations of all the energy-level bound and/or free electrons need to be accounted for. The state of ionization, i.e., whether electrons are free or bound, is an extremely complex topic when the plasma is correlated with the ionic structure. Indeed, the conductivity, the opacity, and other properties of the systems all depend on similar levels of understanding. Therefore, the EOS data provides a test of our fundamental understanding of these systems.

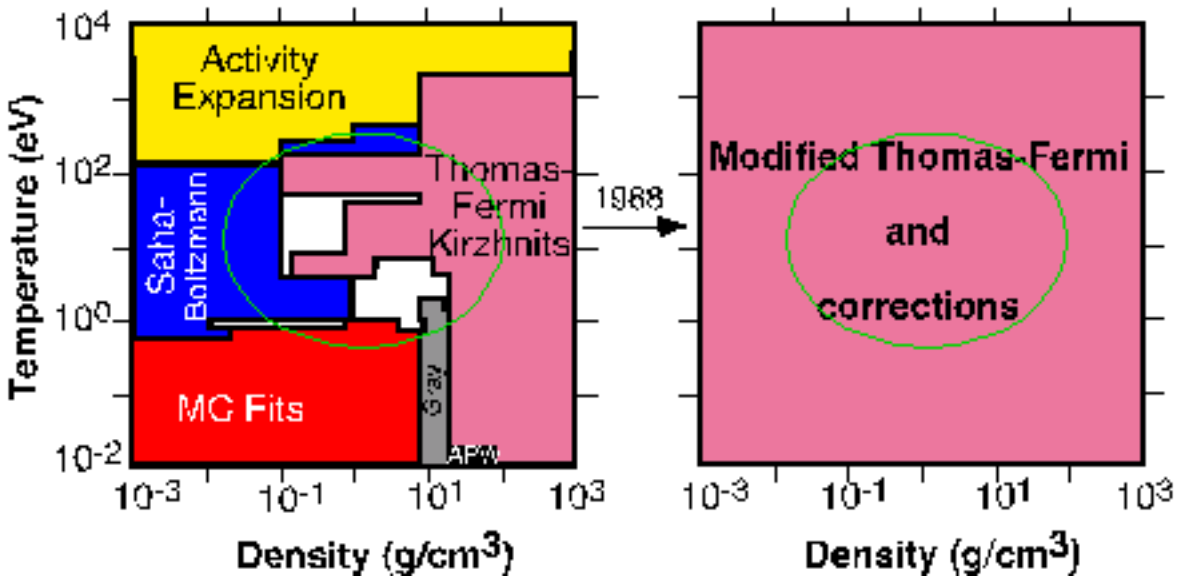

FIG. 3. The phase diagram for copper as constructed from all the various theoretical models. Note that the oval in green indicates the warm dense matter regime where large parts have no valid description or are on the boundaries of validity. The phase diagram on the right indicates the solution to the problem: cover the problem over.

The development of a warm dense matter equation of state can be seen in Fig. 3, where we show a temperature-density phase diagram for copper. The EOS in the various different regions of the phase diagram is calculated with different approximations. However, the region inside the oval is the warm dense matter regime and is a combination of disparate approximate schemes [1] at the limit of their applicability. Moreover, and importantly, some of the warm dense matter regime has no known valid theoretical constructs. From the view of applications in hydrodynamics simulations, the situation, indicated by the left-hand phase diagram of Fig. 3, proved untenable for two reasons. First, to construct an EOS using the numerous approximations took over a month. Second, and more importantly, the EOS thus generated could not be made a smooth function over the entire phase space, due to the fact that the schemes are reaching their limits at the boundaries. This latter problem led to numerical instabilities in hydrodynamic simulations and thermodynamic inconsistency. To resolve this problem, in the late 1980s a new form of single approximation EOS was devised [2] that, although not coming to grips with the warm dense matter regime, sped up the production of EOS tables and allowed hydrodynamic simulations to run—albeit providing questionable answers at times. This ploy has been likened to pulling a tarp over the abyss, leaving us with no warm dense matter EOS.

There is also an astrophysical interest in warm dense matter. Large planets and low-mass stars exist in a state that can be described as warm dense matter. This is true whether the major constituents are hydrogen and helium or more complicated compounds. A correct description of a brown dwarf requires consideration of elements at Mbar pressures over a range of high densities and temperatures. Theories of formation of planetary bodies rely on structure models that are in turn determined by fundamentals like EOS and constrained by observations. While there are good observations of the large solar planets, extrasolar planets are more difficult. By far the largest uncertainty in the structure of extrasolar planets is the EOS, which is the EOS of warm dense matter [3].

Finally, warm dense matter plays the role of a transient state that matter passes through en route from a condensed to a plasma state in some applications. Inertially confined laser fusion is an example of such a "transient" state where warm dense matter is demonstrably important. The pressure as a function of time needed to implode an inertial confinement fusion target (a shell made of low-Z materials containing a mixture of deuterium and tritium) will induce a number of shocks with steadily increasing pressure. The first shock in a design for the National Ignition Facility (NIF) calls for a pressure of about 1 Mbar (100 GPa). These are precisely the conditions recently examined in laser-shock-driven deuterium experiments. That is, a pressure of 1 Mbar, density of 1 g/cm^3, a 6-fold compression, and temperature of ~ 1.1 eV, about 1/5 of the Fermi temperature [4]. This strongly coupled, partially degenerate – warm dense – matter was found to have a much higher compressibility due to dissociation than had been predicted. When a new equation of state for warm dense hydrogen isotopes was constructed to replicate the new data, new predictions of the fusion yield from NIF targets differed markedly from the old ones. It was found that the yield was up to a factor of 30 higher depending on assumptions made about the stability of the implosion [5]. Although one empirical model of the hydrogen equation of state predicted the large compressibility, simulations and the fundamental theories did not. Indeed, there was no way to know the answer without actually performing the experiment. In Fig. 4 we show the Hugoniots, i.e., the locus of points reached by a single shock, for both D_2 (left-hand side) and Be (right-hand side) on a pressure-density phase diagram. The D_2 is essentially the same as the fuel that would be used in the intertial confinement fusion (ICF) implosions and the figure indicates that the measured compression will be substantially increased over the current model. However, it also shows that the best simulation capabilities do not reproduce the data while a simple empirical model based on the observations does. This is an indication of the fundamental difficulty of treating the warm dense matter regime. Moreover, we show in the right-hand side of Fig. 4 the Hugoniot for beryllium, which is used as the pusher to drive the fuel to high density, where one can see that the current EOS does not agree with several other predictions that include shell ionization. Thus, the need for an experimental capability for warm dense matter is clear.

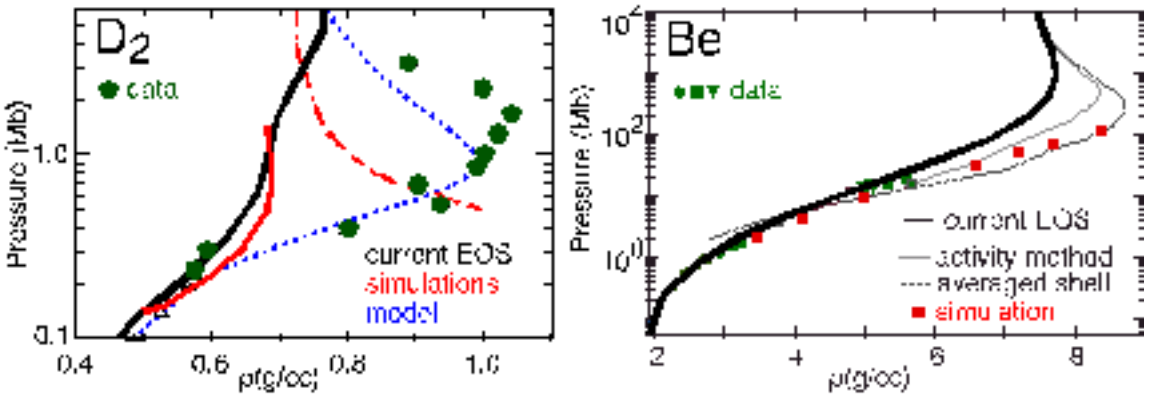

FIG. 4. The pressure– density phase diagram of D_2 on the left and Be on the right showing the Hugoniots. The standard equation of state which corresponds to the current model is shown as the balk curve, the measurements are shown as green points, ands the theoretical curves are shown as gray in the Be plot, red indicates simulations, and the blue curve in the D_2 graph is a simple linear mixing model.

To illustrate that the regimes where the theories do not agree are important to the future of ICF implosions, we show in Fig. 5 the temperature-density tracks for an ICF implosion. In the figure we provide the track for both the fuel and the Be pusher. On both tracks the highlighted area indicates those parts of the track where the warm dense matter effects will play a role, and it is clear that these form a large part of the time history of the implosion.

It has been exceedingly difficult to perform experiments in the warm dense matter regime, which is why we know so little about it. As a first step, one must create a well-characterized warm dense matter state. The second step is gaining information on the state through experiments. The first step has been the problem. Warm dense matter is not a limiting case of matter, e.g., high or low temperature. When created in a laboratory environment, it does not tend to remain in a specified thermodynamic state for very long, making characterization difficult. The only other imaginable method to produce the kind of warm dense matter of interest here might be to use sub-30-fs laser pulses on sub-100-Å-thick foils and perform thermodynamic measurements on a few-fs timescale over extremely small spatial dimensions. To be able to do this on comparatively macroscopic samples (with LCLS) will be a boon.

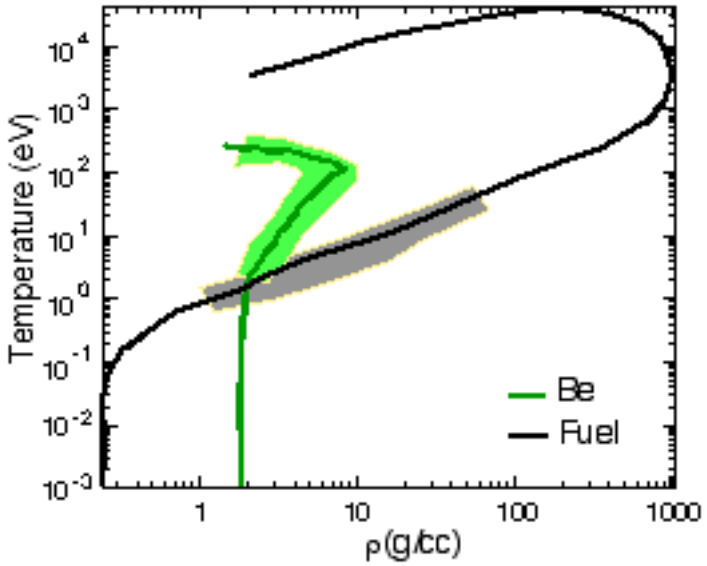

FIG. 5. The track in temperature-density phase space of the Be pusher and the D_2 fuel for an ICF implosion. The areas on the curves (gray for D_2 and light green for Be) indicate the part of the track where the warm dense matter effect will play a role.

B. Plasma spectroscopic studies

There is great interest in the higher temperature dense plasma regime. Here the problem arises from the production of high-temperature plasmas at electron densities in excess of 10^{22} cm^{-3}. In any experiment where a high-intensity, e.g., $I \quad 10^{12}$ W/cm^2, laser irradiates a solid target, there will be a region of the solid that is hot and near solid densities. Lasers with wavelengths > 0.25 μm do not directly heat the solid as they cannot propagate beyond the critical density ~ 10^{21} cm^{-3} x (1 μm / λ_{laser})^2 [6]; however, heat flow from the surface efficiently generates the hot dense medium [6]. The spectroscopic information derived from these plasmas provides, on the one hand, diagnostic information about the plasma itself, while on the other hand, we can use spectroscopy to investigate our understanding of the mechanism at play in the creation of the

plasma and the interaction of the atoms/ions with the plasma in which it is embedded. Here the LCLS provides two related and intriguing possibilities. First, there is the possibility to perform Thomson scattering on plasmas at solid density [7, 8]. Second, we can explore the laser pump-probe techniques for high-density plasmas that have been used in low-density plasmas to measure line shapes, observe radiation redistribution, and determine the kinetics processes [9,10].

1. Thomson scattering

Thomson scattering provides an *in situ* measurement of the temperature, density, charge state, and collective behavior of the plasma. Indeed, the Thomson scattering cross-section diagnostic is directly related to the dynamic structure factor, $S(k, \omega)$, of the plasma and thus provides insight into the theoretical predictions from different theories. In recent years, it is fair to say that each effort at diagnosing a higher density plasma, i.e., higher than 10^{20} cm^{-3}, using Thomson scattering has led to new and important discoveries [11]. These efforts have, of course, been few because the constraints on the experiments are substantial. Here we believe that the LCLS will provide a major advance in diagnosing dense plasmas. This is clearly a complement to the concept of creating warm dense matter, as Thomson scattering can provide a diagnostic of the warm dense matter conditions. However, a precondition for the interpretation of the scattering data is that there is a valid theoretical model for the $S(k,\omega)$ in the high-density regime, which in itself will be a challenge. The tunable nature of the LCLS, the high-energy bandwidth, the short pulse duration and, importantly, the large peak photon flux make this source the only one that can address Thomson scattering of transient plasmas.

2. Laser pump probe techniques

The mechanisms involved in the formation of a plasma and the details of the kinetic processes can be illuminated by using a laser as a pump to selectively populate levels and thus redistribute radiation. In a particularly intriguing possibility, one will be able to study the formation of laboratory x-ray lasers that currently depend on kinetics processes [12]. Thus, one could disentangle the plasma production from the inversion-forming processes that lead to the x-ray lasing. It is clear that numerous aspects of plasma spectroscopy have been severely constrained by a lack of data. The LCLS will provide a substantial improvement in the development of our understanding of intrinsic line shape formation, level shifts, radiation transfer, and detailed kinetics processes.

In both of these areas the LCLS will provide information that would not be obtainable with any other source. The combination of the short pulse length, tunable wavelength, repetition rate, and energy per pulse will make the data derived from LCLS plasma-based experiments a major advance in our knowledge in this area.

III. SCIENTIFIC OBJECTIVES

The objective of plasma-based experiments on the LCLS will be to probe regimes of the temperature and density phase space that cannot be accessed in any other manner. Indeed, it is the combination of several different aspects of the LCLS that allows the probing of matter at extreme conditions. That is, the short pulse duration, the high spectral energy, the high energy per pulse, and the relatively narrow bandwidth make the LCLS unique both for creating extreme warm dense matter conditions and providing a probe of extreme states of matter.

A. Creating and probing the warm dense matter regime

The first scientific objective comes in the area of warm dense matter research. This regime is accessed in all laboratory experiments where one creates a plasma from solid or near-solid density targets. However it is difficult to study this part of the plasma creation process in isolation. Rapid temporal variations, steep spatial gradients, and uncertain energy sources lead to indecipherable complexity. Indeed, although there has been much interest in this regime, witnessed by the literature on strongly coupled plasmas, there has been little progress [13]. The interest generated in laboratory experiments is mirrored in the astrophysical literature where the warm dense matter regime is found, for example, in the structural formation of large planets and brown dwarfs [14-18].

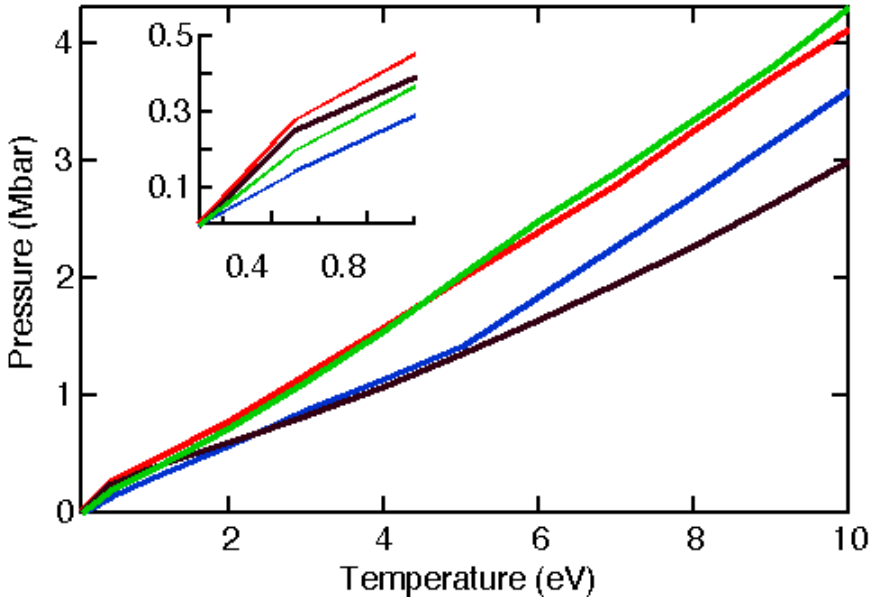

FIG. 6. The isochore for aluminum in the warm dense matter regime for four theoretical models that all provide predictions that agree with the experimental point along the principal Hugoniot. The inset shows the low-pressure, low-density region expanded. Data derived from the LCLS will assist in motivating theoretical developments for this important regime.

The fact that the LCLS will allow the creation and probing of the warm dense matter regime in the laboratory, as discussed briefly below, will provide a set of data that will spark the field. The idea is simple but the impact will be vast, as the data obtained in the generation of warm dense matter along an isochore (i.e., a track of constant density), with subsequent probing along the release isentrope (i.e., a track of constant entropy), will be unique and critically important for progress in the field. The importance of this data derives from the fact that to date the only possible method of generating warm dense matter is by shocking the material. The shock method provides information along the principal Hugoniot, that is, the locus of points in the pressure-density space that are accessed by a single shock—one point for each shock. Although this has been quite useful, it is a very limited set of data providing little information on the general behavior in the warm dense matter regime. Indeed, the amount of data that is currently available is so proscribed that one finds insufficient constraints on theoretical development. This can be

illustrated by the curves in Fig. 6 where several predictions for an isochore of aluminum are presented in the temperature and density phase space. Note that the four theories shown in the figure *all* predict theoretical Hugoniots that fit the experimentally determined Hugoniots, but all differ rather dramatically along the isochore. As aluminum is the most studied material, Fig. 6 can be interpreted as the minimum degree of uncertainty in this field of research and makes it obvious that there is a need for experimental data in this region [14].

B. Plasma spectroscopic studies

The LCLS will be employed in plasma-based experiments to address the foundation of plasma creation in transition to hot dense matter, providing a truly unique method to probe the spectroscopy of hot dense matter. The probing of dense plasmas, whether warm or hot, will move to a new level of sophistication with the use of LCLS-based Thomson scattering, while the active probing of hot dense plasma will be advanced using the LCLS by extending the methods of laser fluorescence spectroscopy that are employed in low-density plasmas with visible lasers to high-density using the x-ray laser source [15].

1. Thomson scattering

We propose to extend the power of spectrally resolved Thomson scattering to the x-ray regime, for direct measurements of the ionization state, density, temperature, and the microscopic behavior of strongly coupled plasmas and warm dense solids [8]. This would be the first direct measurement of microscopic parameters of solid-density matter, which could be used to properly interpret measurements of material properties, such as thermal and electrical conductivity, EOS, and opacity found in astrophysical environments as well as in virtually all plasma production devices.

Thomson scattering is characterized by the scattering parameter α, proportional to the ratio of the laser probe scale-length, λ_L, to the Debye length, λ_D, and the scattering angle Θ:

$$\alpha = \lambda_L/4\pi\lambda_D\sin(\Theta/2) = 1/k_L\lambda_D \sin(\Theta/2). \qquad (1)$$

For $\alpha < 1$, spectrally resolved incoherent Thomson scattering provides information on the velocity *v*, hence temperature, and the directed flow of free electrons from the Doppler shifts experienced by scattered probe photons. For $\alpha > 1$, the collective scattering regime, the scattering is sensitive to temporal correlations between electron motion separated by more than a Debye length, hence the scattering is dominated by ion-acoustic and electron plasma wave resonances, the latter set by the Bohm-Gross dispersion relation [6]. The frequency shift of the resonance is dependent on density through the plasma frequency, while the width of the resonances yields information on the wave damping rates. In the intermediate regime, i.e., near $\alpha = 1$, the form of the high-frequency electron plasma component depends strongly on both the electron temperature and density, providing a robust internal measurement of these basic plasma parameters, confirmed by spectroscopy.

In Fig. 7 we show the T-n_e regimes accessible by Thomson scattering with $\alpha = 2$ for various wavelength probes λ_L. Such Thomson scattering accesses regimes in which the Debye length is of order of the probe wavelength. By switching from a visible laser probe at 5000 Å to an x-ray probe at, e.g., 1.5 Å, we can effectively probe plasmas with Debye lengths of the order of the interparticle spacing or shorter (1 Å). Stated differently, for a given plasma temperature, we should be able to access a density that is 6-7 orders of magnitude higher than previously

attempted. In particular, Fig. 7 shows that the solid-density regime at ~$3x10^{23}$ cm^{-3} crosses the strongly coupled plasma regime precisely where it is accessible by 1.5-12 Å Thomson scattering.

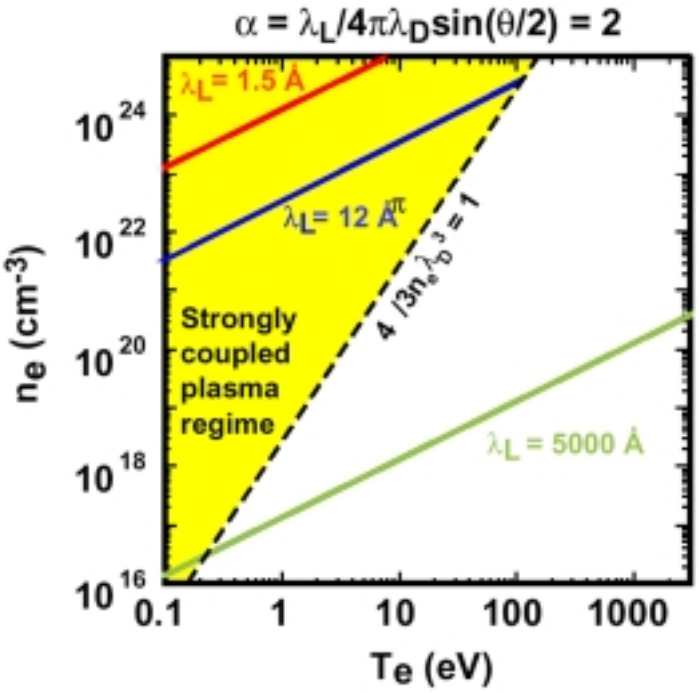

FIG. 7. The temperature and electron density phase space indicating the non-ideal plasma regime by the yellow area. Here we define the non-ideal plasma region as that region having less than one particle per Debye sphere, thus leading to a breakdown in the Debye screening concept. The black dashed line indicates one particle per Debye sphere. Further, we indicate by solid lines the temperature and density at which the scattering parameter α is 2. One can easily observe that for the LCLS, whether at 1.5 Å or 12 Å, the dense regime is accessible, while for the nominal visible laser at 5000 Å, one does not access the regime. Note that the figure does not indicate the Fermi temperature and thus is independent of material; however, the figure does not indicate the region at low temperature where condensed matter theories will be applicable.

For spectrally resolved visible or x-ray Thomson scattering, one does not necessarily need a fully coherent laser for the following reasons:

• First, the experiments proposed here provide valuable, new information on solid-density plasmas by just resolving the high-frequency Thomson scattered components, hence only probe line widths of order v/c are required, corresponding to $\Delta\lambda/\lambda \sim 0.003$ for probing matter at a few eV. These probe line widths can be provided by the LCLS.

• Second, incoherent Thomson scattering ($\alpha < 1$) requires little or no probe transverse coherence, since the scattering from individual electrons for at least ideal plasmas is uncorrelated. In the collective scattering regime ($\alpha > 1$), scattering is sensitive to time-correlated electron motion between two positions separated by the probing scale length λ_s. For moderately collisional plasmas with an electron-ion collision frequency ν_{ei}, the plasma wave propagation distance as set by collisional damping is v/ν_{ei}. Substituting for a typical value of electron-ion collision frequency to plasma frequency $\nu_{ei}/\omega_p = 1/2\pi$, the plasma wave propagation distance can be

rewritten as $2\pi\lambda_D$. Since, by equation 1, $\lambda_L \quad \lambda = 2\pi\alpha\lambda_D$, it follows that the plasma wave propagation distance will be of order λ/α, hence $< \lambda$, within the transverse coherence length of the LCLS.

• Third, the fraction of scattered photons will be substantial. For example, for $n_e = 3x10^{23}$ cm^{-3}, a Thomson scattering cross section of $\sigma = 6.6 \times 10^{-25}$ cm^{-2}, and a path length, *x*, of 0.01 cm in the material of interest, the fraction scattered, $n_e\sigma x$, is approximately 0.002. This level of scattered photons is roughly equivalent to that recorded successfully in space or spectrally resolved fluorescence measurements. Moreover, this is orders of magnitude larger than the usual $10^{-(6\text{-}10)}$ fractions obtained for visible Thomson scattering at lower densities. When this scattered fraction is coupled to an estimated system detection efficiency of 10^{-4} , one finds that the number of scattered photons is 10^{-7} of the incident LCLS photon flux per pulse. Thus, assuming 10^{12} photons per pulse yields a total scattered signal of $> 10^5$ photons.

A schematic of the expected generic scattered spectrum features is shown in Fig. 8. Coherent scattering from tightly bound electrons (Z_{tb} per atom) will provide an unshifted peak at the probe wavelength whose intensity is proportional to Z_{tb}^2. Incoherent Compton scattering from weakly bound electrons (Z_{wb} per atom) should provide a second peak downshifted in energy by the order of $h\nu/mc^2$, with an intensity proportional to Z_{wb}. Thomson scattering from free electrons (Z_f per atom) should provide a dispersed spectrum centered on the Compton peak, with a spectrally integrated intensity varying as Z_f. The form of the spectrum will in, general depend, on the free electron density, n_e, free electron and/or Fermi temp-erature T_{Fermi} and electron-ion collisionality ν_{ei}. Hence, by spectrally resolving the scattered x-rays we would gain access, for the first time, to an unparalleled source of information on warm dense matter.

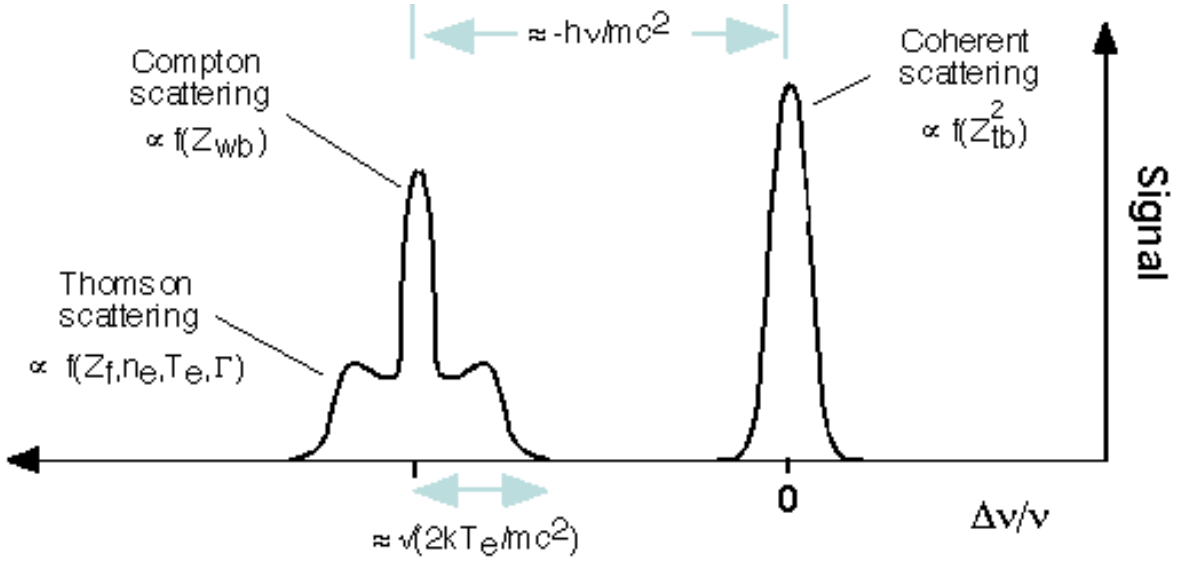

FIG. 8. Schematic of the spectrally resolved x-ray scattering spectrum expected, with information provided by each feature noted. The definition of weakly bound and tightly bound electrons depend on their binding energy relative to the Compton energy shift. Those with binding energies (ionization potentials) less than the Compton shift are categorized as weakly bound.

For example, we should be able to infer Z_f, Z_{tb}, and Z_{wb} from the relative importance of coherent, incoherent, and free electron scattering contributions. This would allow us to discriminate between different ionization balance models used to define the EOS of these plasmas [16]. We

should be able to infer the free electron temperature and density (and hence ionization state since the ion density is effectively hydrodynamically frozen) from the shape of the Thomson scattered spectrum for $\alpha \quad 1$, further shedding light on the equilibrium states of warm dense matter. We should be able to infer the plasma collisionality from the shape of the free electron spectral peak for $\alpha > 1$, allowing us to test the validity of various strongly coupled statistical physics models.

In addition, for strongly coupled plasmas, one of the more intriguing possibilities is the establishment of long-range coherence even in the plasma state. If coherent plasma wave modes exist, then the Thomson scattering contribution should increase as the square of the number of coherent scatterers. More generally, by extending Thomson scattering to the x-ray and solid-density regimes, there is a excellent chance of uncovering novel phenomena.

We note in closing that there is the intriguing possibility of using part of the LCLS beam, for example the spontaneous background, to warm a sample and then use the LCLS to probe it with Thomson scattering. This is in distinction to the idea that we create the plasma using a standard long-pulse laser system. The experiments using the LCLS as the heater and probe are much more demanding, as the number of free electrons may decrease by at least an order of magnitude. Note that the number of free electrons is a matter of great controversy in this regime as the definition of "free" is open to debate [17]. Further, the need to delay the heater from the probe by x-ray optics creates additional losses of ~ 10^{-4} yielding the total number of detected photons per shot on the order of ~1. While this is still detectable, and with the high repetition rate of the LCLS one can easily obtain spectrally dispersed data, the first experiments in both the warm dense matter regime and the plasma Thomson scattering at higher temperatures should be the independently pursued.

2. Laser pump probe techniques

Since the creation of high-density laser-produced plasmas, there have been virtually no quantitative *in situ* measurements of the kinetic rates or the populations. This is a major impediment to progress, as population kinetics of highly stripped ions is a complex problem. The complexity derives from the large number of states that must be considered in a model and the detail to which one must incorporate these states. The situation is made more difficult yet due to the fact that these plasmas tend to have rapid time evolution and large spatial gradients [6].

Indeed, much of the effort to improve the situation has been focused on target design and advanced diagnostic development; however, the difficulties in determining the level populations or the kinetic rates remains. Therefore the interest, which comes from all areas involved with dense plasma studies and its underlying theoretical problems, e.g., laboratory x-ray laser generation, laser plasma production, astrophysics, and inertial fusion, has never been met with substantial improvements in experiments.

The import of the LCLS for high-energy-density plasma experiments is that one can use the LCLS to pump individual transitions in a plasma creating enhanced population in the excited states that can be easily monitored. The idea has been used in studying lower density plasmas with visible lasers and can, with the LCLS, be employed to advance the study of high-density plasmas [18].

Variations on the idea of pumping individual transitions in high-energy-density plasma include the selective pumping of the wings of a line transition to observe redistribution within the line profile and pumping of selected transitions to attempt to understand the inversion mechanisms for the production of laboratory x-ray lasers. In all of these applications, the tests of the theoretical developments in the areas of atomic processes, kinetics model creation, line shape

formation, and x-ray gain studies would be the first of their kind as there are currently no available probes.

There are several constraints on the LCLS as a laser probe of the high-energy-density regime. First, the probe must be tunable, which is easily satisfied. Second, the line width of the pump must be such that it can pump entire line profiles and also be capable—for studies of redistribution within line profiles—of pumping parts of the line profile. Again, these condition are readily met by the proposed LCLS. Finally, we need to have a pump that can move enough population from one state to another so that the population changes can be monitored. This last requirement can be verified by looking at the radiative pumping rate, R_{LU}, due to the LCLS compared to the spontaneous emission rate, A_{UL}, of the transition being pumped. This is proportional to the number of photons per mode and is given by [19]

$$\frac{R_{LU}}{A_{UL}} = 6.67x10^{-22}\frac{g_U}{g_L}\lambda_{\mathring{A}}^5 I_o^{laser}\left(\frac{W}{cm^2}\right)\frac{[,]}{\delta_\lambda \Delta_\lambda} \qquad (2)$$

where the g's are the statistical weights of the upper and lower states, and λ_L and I_o are the LCLS wavelength and intensity. The δ_λ and Δ_λ are the bandwidths of the LCLS and the line shape of the transition being pumped, while [,] represents the minimum of the two. Two important insights emerge when evaluating equation 2. First, if we conservatively assume $I_o \sim 10^{14}$ and $[,]/\delta_\lambda\Delta_\lambda \sim 0.001$, we find that the ratio is approximately 1 for λ_L of 10 Å. This number is at least 10^3 larger than can be obtained by using a plasma source to pump a transition. Second, the ratio does not increase with decreasing LCLS wavelength, indicating that large numbers of photons per mode will not be available as we move toward shorter wavelengths. This is due to the fact that the spontaneous rate has a strong inverse dependence on wavelength. Of course, matching, or at least controlling, the LCLS bandwidth can have salutary effects as indicated by equation 2.

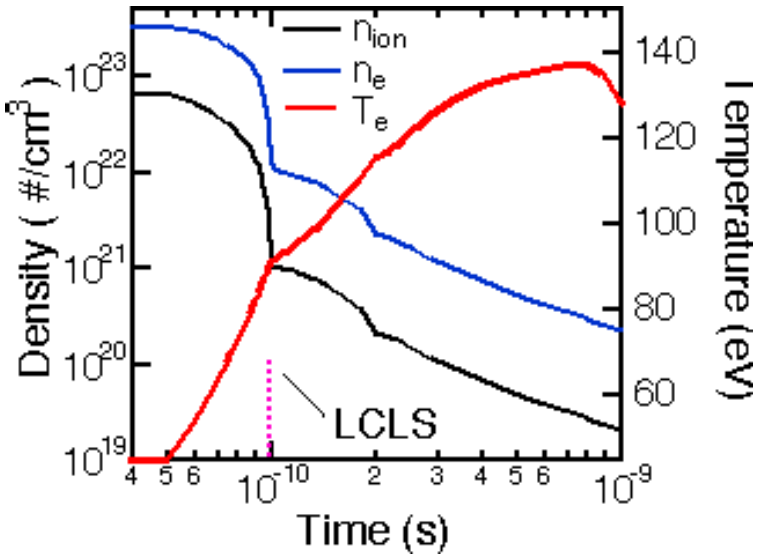

FIG. 9. The plasma conditions for the center of an aluminum foil that starts at solid density and expands. The electron and total ion density are indicated on the left axis, while the temperature in eV is indicated on the right-hand axis versus time in seconds. Note that the LCLS pulse which, for this example, is tuned to the He-like $1s^2$-1s3l transition, irradiates the plasma at ~ 0.995 x 10^{-10} seconds.

The possibilities provided by plasma spectroscopic probing are illustrated with the simulation of an aluminum layer tamped on both sides with a thin layer of CH plastic irradiated by x-rays [20]. An undiluted radiation field emitted from the rear side of a thin, 1000 Å, Au target impinges on

the Al foil, heating it uniformly. The Au foil is irradiated by a single 1 ns, temporally square-shaped pulse of 0.52 μm light at an intensity of 1.6×10^{14} W/cm^2 [21]. The interest in this type of heating source derives from the fact that the x-rays generated by the laser-produced plasma will volumetrically heat the sample, and, due to the CH tamping, will provide a plasma with relatively small gradients. Because the overall conversion efficiency from the laser energy to x-ray energy emerging from the rear-side of the Au foil is on the order of 10%, this provides a substantial radiation source [22]. The plasma conditions of the expanding Al foil are shown in Fig. 9 where the electron density, total atom density, and temperature are shown as a function of time. In addition, the temporal location of the LCLS is shown in the figure

As shown in Fig. 10, the effect of the LCLS on the level populations is dramatic. Here we show the population for the Li-like stage through fully stripped (bare nucleus) ion stages. As the vast majority of the population is in the He-like ground state, the effect of the LCLS pump is to move the population to the He-like excited sates and then on to the H-like ion stage and the bare nucleus. In Fig. 10 the solid lines indicate the populations with the LCLS on, while the dashed lines indicate the same populations when the LCLS is not turned on. Note that there are essentially no bare nuclei in the plasma when there is no LCLS.

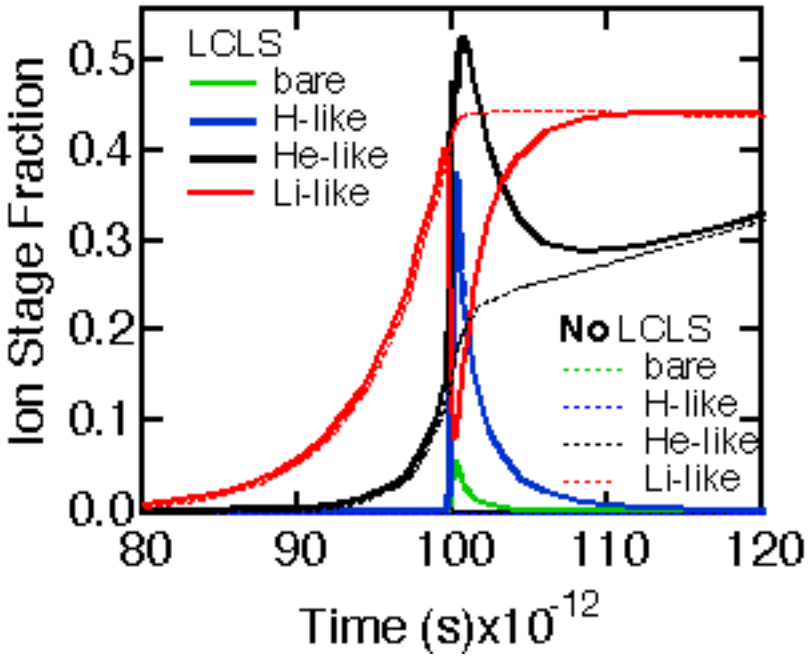

FIG. 10. The ion stage populations, expressed as a fraction of the total ion population, versus time, both with and without the LCLS pumping the He-like Al 1-3 transitions. Note that there is substantial population movement and the H-like and bare nuclei stage are significantly enhanced at the expense of the He-like stage. Further, note that although the LCLS pump is ~200 fs in duration the effects of the pump are observed for ~ 20 ps.

The emission spectrum will be observable and it is shown in Fig. 11 at two times in the evolution of the plasma, one near the initiation of the LCLS pulse and the other at 18 ps later. The most notable feature is that there is a substantial increase in the hydrogenic transitions. For example, the Lyman-α line at ~ 1724 eV, which is unobservable in the He-like background emission without the LCLS pump, rises well above the background with the LCLS pump. Further, the structure of the He-like resonance series starting at ~1598 eV and ending at the bound-free

continuum near 2086 eV is substantially changed by the LCLS pumping. Indeed the Li-like satellite transitions seen on the low-energy side of the He-like $1s^2$-1s2l transitions are substantially enhanced. Note that the effect of the pumping is convolved with the changes in the plasma as indicated both by the changes in the emission levels and the time evolution of the plasma shown in Fig. 10. The major effect of the pump, although it is tuned to a particular transition, is to cause photoionization due to the pump strength. The ionization of the Li-like stage and the pumping of population from the He-like ground state up to the H-like ion stage cause a slow recombination decay back towards the He-like ground state.

It is clear from the emission spectra shown in Fig. 11 that one could use a fraction of the LCLS pump to generate observable signals. The detailed information that can be obtained from these measurements would provide unique constraints on the complex processes necessary to construct a complete kinetics model for the highly charged ions. Indeed, we chose to use as an example the K-shell spectra as it is easily interpretable; however, the generation of L-shell and M-shell models are also of importance and raise the level of complexity substantially. Thus, one can understand the need for experiments that can provide basic information on the processes necessary to build kinetics models.

This calculation is only one of many that are of interest to the study of plasma spectroscopic processes. Indeed the use of the LCLS to pump part of a line transition to observe redistribution within a line profile is another important avenue for study [22], while the testing of the kinetics of gain in collisionally pumped x-ray lasers can be performed by substituting the LCLS for the collisional pump [23].

IV. EXPERIMENTAL REQUIREMENTS

A. Laser-based plasma production

Performing plasma-based studies using the LCLS requires several critical components but none more obvious than a method of generating the plasmas to be studied. In the one case where we study warm dense matter, we could generate the plasma with the LCLS. But in all other studies, the LCLS functions as a probe of a plasma that must be produced by some other mechanism. The simplest way to generate diverse plasmas is to employ at least two laser systems. The first would be a high-energy laser that can produce high-energy-density, i.e., hot dense plasmas; the second would be a short-pulse laser that produces fast electron/fast ion-heated plasmas. The short-pulse laser system could also be used to provide the needed Fourier-domain interferometry that will be used to probe the warm dense matter samples [24].

1. Specifications of the high-energy laser system

To explore the high-energy-density regime, one needs a high-energy and high-intensity laser system consisting of two beams of > 100 Joules in 1 ns with a wavelength of ~500 nm and ~250 nm. Further, there is the need for an additional beam for lower density probing, e.g., a 250 nm probe beam with picosecond capability. Synchronization of this larger laser system with the LCLS is critical. Costing of such a system can be obtained.

2. Specification of the short-pulse laser system

There is a need for an additional short-pulse capability to ensure that the fs time domain is covered. Here one requires the short pulse to perform Fourier domain interferometry as a

diagnostic. In addition, one can use the short-pulse laser to generate short, bright bursts of x-rays for additional absorption experiments on plasmas created by the LCLS. Finally, the generation of an intense source of high-energy electrons can be of use to both create and excite plasmas that would be probed by the LCLS.

B. LCLS parameters

It seems that the parameters of the LCLS useful for plasma-based studies tend to have wavelengths greater than 1.5 Å. This is dictated by the favorable pumping of the bound-bound transitions in this wavelength regime and by the need to warm matter uniformly in the warm dense matter experiments.

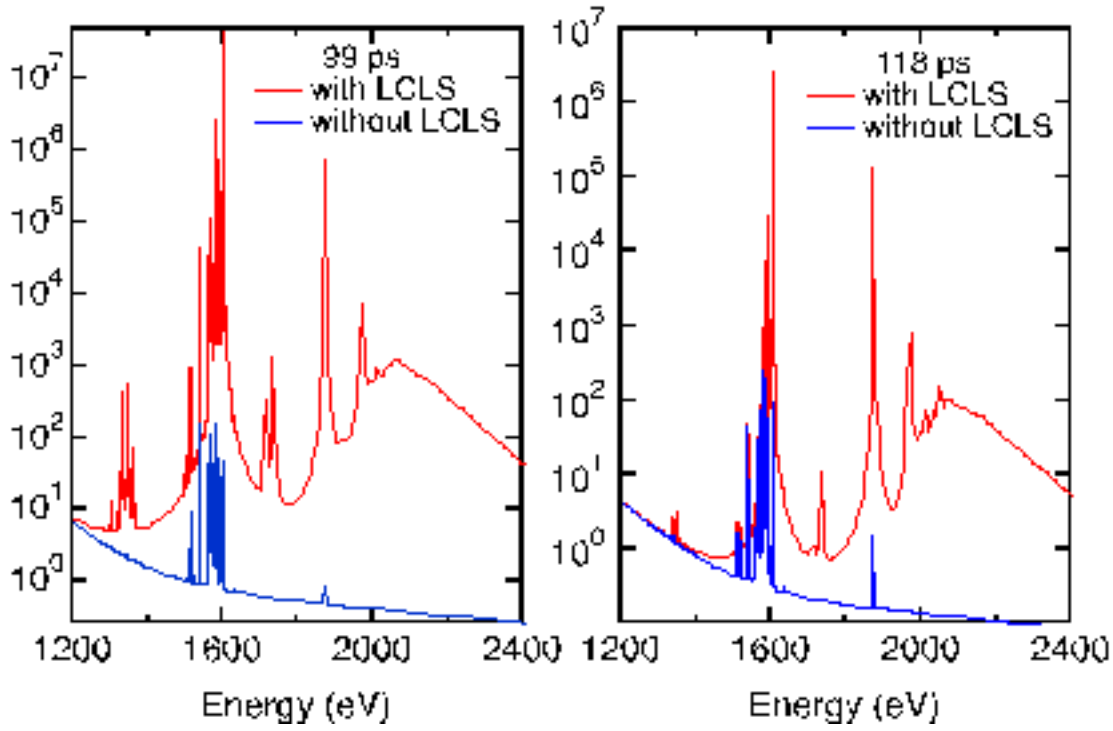

FIG. 11. The logarithm of the emissivity versus spectral energy for two times in the evolution of an exploding aluminum foil. The emission from the plasma with no LCLS pump is shown in blue while the red spectra indicate the emission when the LCLS pumps the He-like n =1 to n = 3 transition. The He-like emission, from, e.g., n =2, 3 and 4 at 1598 eV, 1868 eV, and 1963 eV, respectively, increases substantially, while the H-like n=2 emission at 1724 eV arises with the pump.

For the warm dense matter experiments, it would be useful to use the spontaneous emission to heat the sample. As there is a substantial fraction of the energy in the spontaneous background and it has the same temporal behavior, one could easily use this to gain additional heating of the samples. Indeed , if one could focus the spontaneous emission to a reasonable spot size, say 20 μm, then this would provide additional heating.

Further, for the experiments we have discussed here, the nominal 233 fs pulse length has been assumed. However, for the higher density experiments, the idea that one could saturate a transition is possible, *if* the LCLS had a shorter pulse with somewhat higher intensity. Thus, it would be of interest to have a shorter pulse LCLS.

For those experiments where the LCLS is used either to probe via Thomson scattering or to pump distinct levels, the spontaneous background and the higher order harmonics must be removed from the beam before interaction with the plasma. This clearly requires filtering.

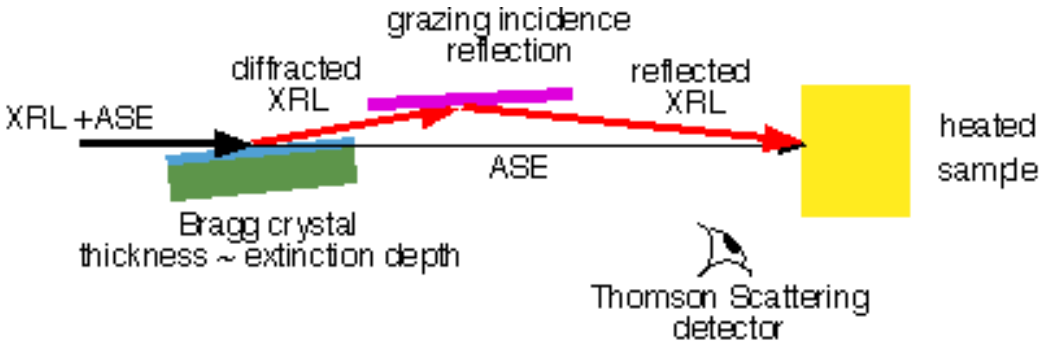

(a.)

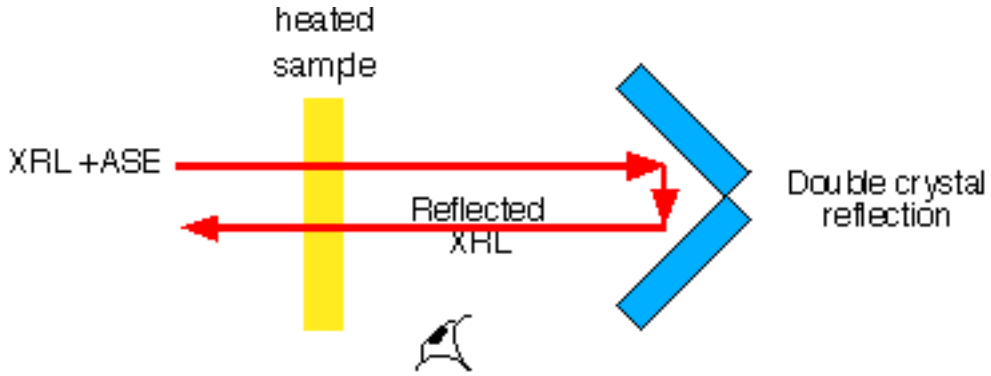

(b.)

FIG. 12. Two schematic experimental setups, a. and b., illustrating the need for x-ray optics in order to use the LCLS to heat and probe a sample.

C. Optics

Optical components that can select out the lasing part of the LCLS beam from the spontaneous background and higher order harmonic will be needed for the plasma-based experiments. In an example of a demanding experiment, we show in Fig. 12 two possible methods for using the LCLS to both heat a sample to the warm dense matter regime and perform Thomson scattering from the sample The schematic in Fig. 12(a.) requires one to have the LCLS laser diffracted from a crystal while passing the remainder of the beam through to a sample. The diffracted part of the beam is then relayed to the sample and acts as a Thomson scattering probe. Thus, one would require, e.g., 8 keV diffraction and relay optics with high throughput. In the second part of the figure, 12(b.), we pass the entire beam through the sample and use a double-crystal arrangement to selectively diffract the laser back toward the sample to act as a Thomson scattering probe. Here we require a double crystal with high throughput to reflect the beam back to the sample. Optics of this type will be essential for plasma-based experiments.

D. Instrumentation

First, one will require an accurate measure of the LCLS flux as it enters and leaves the experimental area. In the case of the warm dense matter experiments, this will be crucial to verification of the deposited energy. Further, in the warm dense matter, plasma probing, and pumping experiments, one will need to control the intensity onto target. Thus, controllable beam attenuation will be needed.

Next, the LCLS will require a synchronization system that can drive ancillary laser systems and the time-resolving detection diagnostics. This would have to be on the order of the LCLS pulse length, i.e., about 200 fs.

All of these spectroscopy experiments assume that one has time-gated, spectrally dispersing x-ray detectors capable of measuring x-rays in the range of 800 eV-15 keV. Advances on the current state of the art will be necessary as we are currently limited to 30 ps in gating technology and about 1 ps in streak-camera technology.

Finally, we note that plasma-based experiments will occur in a vacuum chamber that allows the plasma-creating laser to be focused to high intensity. Coupling the LCLS beamline to the laser target chamber will be a challenging task. The creation of plasmas brings the destruction of targets and the associated problems of debris and/or vaporized targets. These must be accommodated in the experimental design.

V. REFERENCES

[1] See, e.g., K.S. Trainor, J. Appl. Phys., **54**, 2372 (1983).

[2] R.M. More *et al*., Phys. Fluids, **31**, 3059 (1988).

[3] T. Guillot, Science **286**, 72 (1999).

[4]L.B. Da Silva *et al.*, Phys. Rev. Lett. **78**, 483 (1997); G. W. Collins *et al.,* Science **281**, 1178 (1998).

[5] T.R. Dittrich e*t al.,* Phys. Plasmas **6**, 2164 (1999).

[6] For general references to the concepts of laser-produced plasmas and plasma physics see the *Handbook of Plasma Physics*, **3**, "Physics of Laser Plasmas" M.N. Rosenbluth and R.Z. Sagdeev, eds., (Elsevier, Amsterdam, 1991).

[7] H.-J. Kunze, in *Plasma Diagnostics*, edited by W. Lochte-Holtgreven (North-Holland, Amsterdam, 1968).

[8] J. Sheffield, *Plasma Scattering of Electromagnetic Radiation* (Academic, New York, 1975) and references therein.

[9] C.A. Back *et al.*, Phys. Rev. Lett. **63**, 1471 (1989); Phys. Rev. A **44**, 6730 (1991); and J. Koch *et al.*, Appl. Phys. B **58**, 7 (1994). Note that to date in higher density plasmas only the total emitted fluorescence has been studied in photopumping experiments of ion emitters.

[10] For example see A.Bar-Shalom *et al.*, Phys. Rev. A **38**, 1773 (1988) and K.B. Fournier *et al.*, JQSRT **65**, 231 (2000).

[11] S.H. Glenzer *et al.*, Phys. Rev. Lett. **82**, 97 (1999).

[12] See *X-Ray Lasers*, G. Tallents, ed.,.(IOP, Bristol,1990); AIP Proceedings X-ray Lasers, **49** (1994); and the *X-ray Lasers*, Conference series #151, 122 (IOP Publishing, Bristol, 1996) for general papers.

[13] See the papers in *Strongly Coupled Coulomb Systems*, G.J. Kalman, ed., (Plenum, New York, 1998) and the references therein.

[14] F.J. Rogers and D.A. Young, Phys. Rev. E **56**, 5876 (1997) and the references therein.

[15] The field of laser induced fluorescence is currently limited to neutral or near-neutral species. For recent examples see: D. Voslamber, Rev. Sci. Inst. **71**, 2334 (2000); J. Amorim *et al.*, J. Phys. D **33**, R51 (2000); R.E. Neuhauser *et al.*, Rev. Sci. Inst. **70**, 3519 (1999).

[16] D.A. Liberman, Phys. Rev. B 20, 4981 (1979) and F.J. Rogers, Phys. Plasmas **7**, 51 (2000).

[17] The controversy on the definition of free versus bound electrons is closely connected with the role of ionization potential depression, continuum lowering, and level shifts near the continuum. See the discussions in ref. [16].

[18] See as examples: D.D. Burgess and C.H. Skinner, J. Phys. B **7**, L297 (1974) and G. T. Razdobarin *et al.*, Nucl. Fusion **19**, 1439 (1979).

[19] R. C. Elton, *X-ray Lasers* (Academic Press, San Diego, 1990).

[20] H.A. Scott and R.W. Mayle, Applied Phys. B **59**, 35 (1994) and can be obtained from the website http://www.llnl.gov/def_ sci/cretin.

[21] D. Kania *et al.* Phys. Rev. A **46**, 7853 (1992); J. Koch *et al.*, JQSRT **54**, 227 (1995); J. Moreno *et al.*, Phys. Rev. E **51**, 4897 (1995).

[22] C. Mossé *et al.*, JQSRT **58**, 803 (1997) and Phys. Rev. A **60**,1005 (1999).

[23] S.H. Glenzer *et al.*, JQSRT **65**, 253 (2000) and Phys. Rev E **62,** (2000).

[24] See, for example, P. Volfheyn *et al.*, Phys. Plasma **6**, 2269 (1999).

Structural Studies on Single Particles and Biomolecules

J. Hajdu, *Uppsala University, Uppsala, Sweden*
K. Hodgson, *Stanford Synchrotron Radiation Laboratory, Stanford, CA, USA*
J. Miao, *Stanford Synchrotron Radiation Laboratory, Stanford, CA, USA*
D. van der Spoel, *Uppsala University, Uppsala, Sweden*
R. Neutze, *Uppsala University Uppsala, Sweden*
C.V. Robinson, *Oxford University, South Parks Road, Oxford, UK*
G. Faigel, *Research Institute for Solid State Physics, Budapest, Hungary*
C. Jacobsen, *State University of New York at Stony Brook, Stony Brook, NY, USA*
J. Kirz, *State University of New York at Stony Brook, Stony Brook, NY, USA*
D. Sayre, *State University of New York at Stony Brook, Stony Brook, NY, USA*
E. Weckert, *HASYLAB at DESY, Hamburg, Germany*
G. Materlik, *HASYLAB at DESY, Hamburg, Germany*
A. Szöke, *Lawrence Livermore National Laboratory, Livermore, CA, USA*

I. SUMMARY

Today, the bottleneck in the atomic resolution imaging of biological systems is a fundamental need for crystals. This limits the scope of detailed structural analysis to macromolecules and macromolecular assemblies that can be crystallized. Many biologically important target complexes are difficult or impossible to crystallize. As a consequence, there are large and systematically blank areas in structural biology. Only a handful of membrane protein structures are known, structural studies on large assemblies are problematic, and there is no hope of reaching high resolution with currently available methods on nonrepetitive and nonreproducible structures (e.g., cells). X-ray free electron lasers like the Linac Coherent Light Source (LCLS) have the potential of changing this.

The main difficulty in biomolecular imaging at high resolutions is due to radiation damage [1,2]. We describe detailed calculations, which explore the parameter space (pulse length, integrated intensity, wavelength) within which biomolecular imaging may be possible with x-rays before damage-induced movements destroy the sample. These calculations show a substantially extended limit in radiation tolerance with intense x-ray pulses in the femtosecond time domain. The predicted radiation tolerance to hard x-rays in this regime is several orders of magnitude higher [3] than theoretical limits in conventional x-ray experiments [1,2]. At the outer extremes of these limits (not reached by LCLS in the first phase of its operation), scattering to high resolution may be recorded from large single macromolecular structures, viruses, nanocrystals, and nanoclusters of proteins without the need to amplify scattered radiation through Bragg reflections. Nevertheless, very important new experiments can be performed initially with the LCLS, even as an ongoing machine R&D program progresses toward approaching these limits. Averaging procedures can be applied to extend resolution when a reproducible sample scatters a sufficiently large number of photons for its orientation to be determined. Large samples scatter more x-rays (even if they have no internal symmetry), and thus their orientation is easier to determine than the orientation of smaller molecules. In the first instance, nanocrystals, nanoclusters of proteins, and individual virus particles will be studied. Holographic imaging, the utilization of increased radiation tolerance in short and intense x-ray pulses, numerical alignment

and averaging of many images, and the intrinsic solution of the phase problem by oversampling will give increased resolution on such large and reproducible macromolecular structures. The planned studies with the LCLS will explore these extraordinary possibilities.

The short time structure of the source will allow a range of novel time-dependent experiments in which femtosecond spectroscopy can be combined with very fast structural studies (cf. proposal on femtochemistry). While certain key reactions in life are photochemical, most enzymes participate in diffusion-dominated processes with their reactants and partners. Time-resolved structural studies on diffusive processes in crystalline enzymes are difficult due to problems with mixing enzyme and reactant in the crystal. With submicron-sized samples, the vast majority of solution techniques and methodologies will suddenly become available for time-resolved structural investigations at the LCLS.

X-ray diffraction tomography will be performed with the unfocused LCLS beam on whole cells at "intermediate" resolutions. With nonreproducible structures (e.g., living cells) or with reproducible but small structures (e.g., single protein molecules), higher resolutions could only be reached with a focused beam and with shorter pulses than the pulses planned initially at the LCLS. Thus, the proposal also explores requirements for future developments with the source and will help guide R&D goals for improvements. (See section on x-ray laser physics.)

Ultrashort and high-intensity x-ray pulses from the LCLS, in combination with novel container-free sample handling methods, will open up amazing new possibilities for structural determinations with x-rays and may lead eventually to high-resolution experiments on non-repetitive and nonreproducible structures like cells. This is a "never seen" regime where only predictions and simulations exist today.

II. INTRODUCTION

The history of the living world can be summarized as an elaboration of ever more perfect eyes within a Cosmos in which there is always something new to be seen [4]. Radiation damage hinders structural studies on single biomolecules. Recently, a new dynamic barrier of radiation tolerance has been identified at extreme dose rates and ultrashort exposure times [3]. This barrier is several orders of magnitude higher than limits in conventional experiments [2]. At these extremes, sections of molecular transforms from single macromolecules may be recorded without the need to amplify scattered radiation through Bragg reflections. This area is virtually unexplored. Resolution under these conditions would not depend on sample quality as in conventional crystallography but would be a function of radiation intensity, pulse duration, wavelength, detector parameters, and the extent of ionization and sample movement during the exposure. With reproducible samples, atomic resolution may be achieved through averaging. The potential benefits from studies in this field are substantial

Central to the exploitation of the LCLS in structural biology is the question of the smallest sample size from which it may be physically possible to obtain useful structural information. This may be a single molecule (could we get rid of the crystal in crystallography?), a closed periodic cluster of molecules (oligomers, viral capsids), or an open periodic structure (nanocrystals, microcrystals). First we present an analysis of the dynamics of x-ray scattering from biomolecules and their multimers in ultrashort exposure times at high radiation intensities. Based on this analysis, we then propose biological experiments at the LCLS.

III. THEORY OF IMAGING WITH INTENSE, ULTRASHORT X-RAY PULSES (from *Neutze et al.* [3])

Radiation damage limits high-resolution structural studies on nonrepetitive and nonreproducible structures like individual biomolecules or cells [2]. Cooling can slow down sample deterioration, but it cannot eliminate damage-induced sample movement within the time needed to complete conventional measurements [1,2,5]. Analysis of the dynamics of damage formation [6-8] suggests that the conventional damage barrier (about 200 x-ray photons/Å^2 at 12 keV x-ray energy or 1Å wavelength) [1] may be extended at very high dose rates and very short exposure times. Free electron lasers (FEL) currently under development [9,10] could provide hard x-ray flashes with pulse durations of less than 100 fs and peak brilliance of 10-11 orders of magnitude higher than that which is currently available from third-generation synchrotrons. Here we show that such pulses may allow structural studies on large biomolecules before the effect of radiation damage destroys the sample and may permit the imaging of complex structures without the need to amplify scattered radiation through Bragg reflections.

A. Physics of damage formation

Radiation damage is caused by x-ray photons depositing energy directly into the sample. At 1 Å wavelength (12 keV energy), the photoelectric cross section of carbon is about 10 times higher than its elastic scattering cross section making the *photoelectric effect* the primary source of damage. The photoelectric effect is a resonance phenomenon in which a photon is absorbed and an electron ejected [11], usually from a low-lying orbital of the atom (about 95% of the photoelectric events remove K-shell electrons from carbon, nitrogen, oxygen, and sulphur), producing a hollow ion with an unstable electronic configuration. Relaxation is achieved through a higher shell electron falling into the vacant orbital. In heavy elements, this usually gives rise to x-ray fluorescence, while in light elements, the electron falling into the lower orbital is more likely to give up its energy to another electron, which is then ejected in the *Auger effect*. Auger emission is predominant in carbon, nitrogen, oxygen, and sulphur (99-95%, [12]), thus, most photoelectric events ultimately remove two electrons from these elements. These two electrons have different energies (around 12 keV for photoelectrons and around 0.25 keV for Auger electrons) and are released at different times. Relevant K-hole lifetimes can be determined from Auger linewidths [12], and are 11.1 fs (C), 9.3 fs (N), 6.6 fs (O) and 1.3 fs (S). *Shakeup excitations* (multiple ionization following inner shell ionization, see, e.g., ref. 13), initial- and final-state configuration interaction, and interference between different decay channels will modulate this picture. Most of the time photoionization ejects an inner shell electron so fast that the outer shell electrons have no time to relax. The situation is similar to beta decay, in which the nuclear charge suddenly increases by one unit. The result is that the outer shell electrons find themselves in a state that is not an eigenstate of the atom in its surroundings. Quantum mechanics describes such a state as a superposition of proper eigenstates, which include states where one or more of the electrons is unbound. Such a collective effect is called shakeup. The release of the unbound electron "competes" with Auger electrons—i.e., the interaction of two outer shell electrons whereby one of them fills the inner shell hole and the other gets unbound. (After the Auger process is completed, the electric field in the inner shells of the atom returns to its original value, therefore many fewer additional shakeup electrons are released.) When the first electron velocity is low, it can interact with the other (valence) electrons on its way out. The situation will be more complicated, but, in general terms, less shakeup will happen. If the energy of the first electron is above some threshold, the

sudden approximation is valid. In our case, we expect that the sudden approximation is good for the primary photoelectron, and a shakeup fraction of about 10% is expected.

An additional effect is *inelastic* (Compton/Raman) *scattering*, which represents a direct momentum transfer from an x-ray photon to an electron, so that the x-ray photon is scattered with a reduced energy. If the energy taken up by a bound electron is greater than its shell binding energy, the atom will be ionized. The inelastic cross section of carbon, nitrogen and oxygen is around 3% of the corresponding photoelectric cross sections [14-16], whereas the inelastic cross section of hydrogen is much higher than its photoelectric cross section.

Other factors also contribute to damage. The average velocities of photoelectrons (43 nm/fs) and Auger electrons (7 nm/fs) enable these electrons to escape the protein environment in less than a fs during *early phases* of an exposure. At these velocities the inelastic electron scattering cross sections for carbon [2] lie between 0.1 and 2.0 $Å^2$ such that approximately one electron in five would deposit additional energy into the molecule from which it escapes and may also remove outer shell electrons [17]. In *late phases* of an exposure, a significant fraction of the emitted electrons will not be able to escape the increased positive potential of the sample. Trapped electrons will increase the kinetic energy of the sample through thermal equilibration, but they will also slow down the Coulomb explosion of the sample by partially neutralizing the positively charged protein core as a plasma is formed. These opposing effects have not been considered here, but are factors that are likely to influence the dynamics of larger systems. All plasmas start cold and dense and become hot later (see proposal on plasma-based studies).

It has been argued that in addition to the effects listed above, extreme x-ray intensities could strip all outer shell electrons from their parent atoms on a time scale of attoseconds [8]. However, a quantum mechanical analysis of the electric-field-induced tunneling demonstrates that atoms actually become stabilized against ionization via this mechanism at high photon frequencies [18].

B. Modeling damage formation and sample dynamics

We have constructed a model [3] in which x-ray-induced damage is described stochastically based on the probability of a photoelectric or an inelastic event. Within the model, the instantaneous probability of ionization of atom j at time t was calculated as the product of its photoelectric or Compton/Raman cross section [14-16] and the x-ray intensity I(t). Auger emission was modeled as a stochastic exponential decay to reproduce appropriate K-hole life-times. The direction of photoemission was distributed according to a random deviate that followed a Gaussian distribution [11]. A recoil velocity for the ionized atom due to inelastic scattering or the emission of a photo- or Auger electron was determined from energy and momentum conservation. For inelastically scattered photons, the angle of deflection was determined by a random deviate following a Rayleigh distribution [11]. For each inelastic scattering event, the electron's recoil energy was calculated, and, in cases when this was greater than the binding energy of the electron, an ionization event was modeled (this approximation was deemed sufficient for light elements with weakly bound electrons). An inventory was kept on what electrons remained on what atoms, and changes in the photoelectric, elastic, and inelastic (Raman/Compton) scattering cross sections of all atoms were computed and updated during exposures**.**

A program was created (XMD, [19,3]) that extends the GROMACS molecular dynamics package [20] and simulates electronic and structural changes triggered by x-rays in the sample. The GROMOS force field [21] was modified to incorporate Morse potentials for the description of all chemical bonds, thereby enabling bonds with sufficiently high energy to break. For water,

the simple point charge model [22] was used and adapted in the same manner [23]. Elastic, inelastic, and photoelectric cross sections of atoms were incorporated and changes in the cross sections during the x-ray exposure were modeled, using theoretical values [14-16]. Femtosecond collisional electron transfer and slower radical reactions were not modeled. Modification of the dissociation energy of two atoms due to electron emission was not taken into account.

A small protein, T4 lysozyme [24], was used as a model, including its 118 crystallographically determined water molecules, which bind tightly to the protein molecule. Hydrogens were added to polar and aromatic groups and to water oxygen atoms; the initial charge on the protein was +8. After several rounds of energy minimization the root mean square deviation from the crystal structure of the protein was 0.21 Å for all non-hydrogen protein atoms. This structure was used as the starting point for subsequent molecular dynamics simulations. Simulations were performed with a time step of 50 attoseconds, taking all nonbonded interactions into account explicitly.

In the calculations, the x-ray pulse with intensity I (t), was taken to have a Gaussian temporal profile with a pulse duration (full width at half maximum, FWHM) of 1, 2, 5, 10, 20, 50, 100, 200, 300, 500, and 1000 fs, respectively. The total integrated x-ray flux, I_{tot}, was expressed as the number of 12 keV x-ray photons passing through a 100-nm-diameter circular focal spot, and simulations were run with intensities I_{tot} between 10^{10} and 10^{14} photons/pulse. A simulation with $I_{tot} = 0$ was the reference simulation for calculating elastic scattering properties. The maximum intensity of the x-ray pulse was put at time t = 0, and the simulations were run from t = -1.2 FWHM to +1.2 FWHM (covering 99% of the integrated pulse). All simulations were repeated with different random number seeds for the stochastic events to test reproducibility. The results deviated by less than 5% from each other. Further sets of simulations were performed to estimate wavelength-dependent effects.

For unpolarized x-rays the mean number of elastically scattered photons $\boldsymbol{I}(\mathbf{u},\Omega)$ to be detected by an idealized detector pixel of projected solid angle Ω centered at a positional vector $\mathbf{u}$ is

$$\boldsymbol{I}(\mathbf{u},\Omega) = 1/2(1+\cos^2 2\theta)\Omega r_e^2 \int_{-\infty}^{\infty} I(t) \left| \sum_j f_j(t) \exp\{i\Delta\mathbf{k}(\mathbf{u}) \cdot \mathbf{x}_j(t)\} \right|^2 dt \qquad (1)$$

where r_e is the classical electron radius; I(t) is the intensity of the x-ray pulse; $f_j(t)$ is the atomic scattering factor for the j^{th} atom as a function of time; $\mathbf{x}_j(t)$ is the position of this atom as a function of time; and $\Delta\mathbf{k}$ is the change in the wave vector of the x-ray photon when scattered through 2θ radians towards the pixel centered at $\mathbf{u}$. Radiation damage interferes with the atomic scattering factors $f_j(t)$ and the atomic positions $\mathbf{x}_j(t)$.

C. Predicted scattering patterns from single biomolecules and particles

Energies and ionization events for three simulations on lysozyme are shown in Fig. 1. The protein and its bound solvent molecules were considered to be in the gas phase, under conditions similar to a non-destructive electrospray mass spectrometry experiment. For each simulation in the figure, a total flux of $3x10^{12}$ (12 keV) x-ray photons passed through the 100-nm-diameter focal spot, corresponding to $3.8x10^6$ photons/Å^2 and causing approximately 2,000 primary ionization events, or more than one ionization event for each non-hydrogen atom in the sample. For FWHM = 2 fs (Fig. 1a) only a quarter of the K-holes created by inner shell

ionization events had time to decay via Auger electron emission. As a consequence the total number of positive charges on the sample at the completion of the 2 fs pulse was only 60% of the total number of charges at the completion of the 50 fs pulse (Fig. 1c).

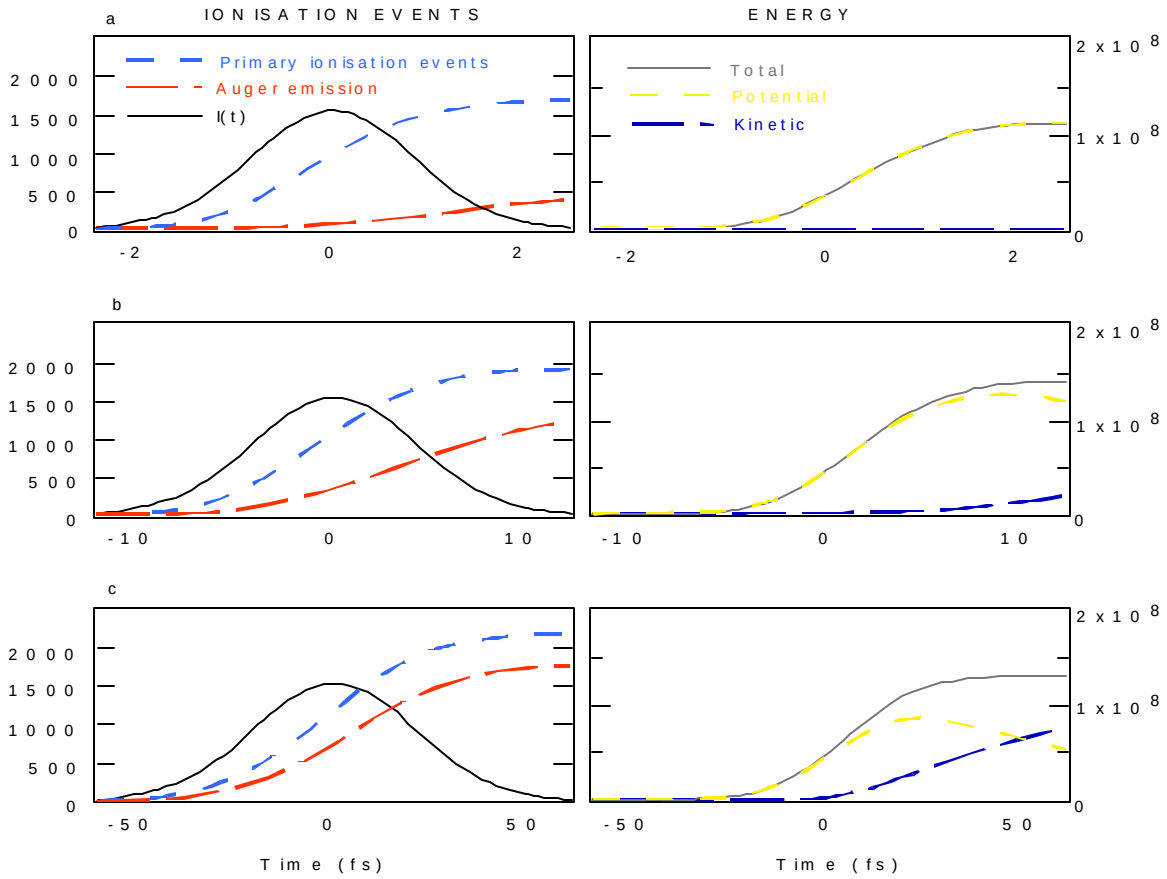

FIG. 1. Ionization of a lysozyme molecule in intense x-ray pulses. Pulse FWHM was 2 fs (a), 10 fs (b) and 50 fs (c). The integrated x-ray intensity was $3x10^{12}$ (12 keV) photons/100 nm diameter spot ($3.8x10^{6}$ photons/Å^2) in all cases. The creation of a large number of positive charges (left hand panel) due to primary ionization by x-rays (photoelectric effect, as well as Compton/Raman scattering) and subsequent Auger emissions results in a rise in the potential (mainly electrostatic) energy of the sample (right). The degree of conversion of potential energy into kinetic energy during the x-ray exposure is inertia limited and as a consequence depends strongly on the duration of the pulse. The Gaussian shape of the x-ray pulse is indicated.

Furthermore, during short intense pulses, numerous K-holes may be present at any one time, reducing the photoelectric cross sections of atoms in which they were produced and thus lowering the total number of primary ionization events in the sample (see trend in Fig. 1). This effect makes the system radiation hardened to photoionization during very short exposures and is more pronounced at even higher radiation intensities. The creation of a large number of positive charges in close proximity results in a rise in the electrostatic energy of the sample (Fig. 1), which drives its eventual explosion (Fig. 2). Under these conditions, each sample will survive only a single shot. The degree of conversion of potential energy into kinetic energy during the x-ray exposure is inertia limited and, as a consequence, strongly depends on the duration of the

pulse. During the 2 fs pulse, there was insufficient time for the kinetic energy to grow appreciably (Fig. 1a). In contrast, by the completion of the 50 fs pulse the kinetic energy of the sample had surpassed its potential energy (Fig. 1c), indicating that the explosion of the sample was well under way. In longer exposures, this effect is even more pronounced.

The destruction of the sample by the x-ray pulse is illustrated by snapshots from the trajectories for pulse FWHM of 2, 10 and 50 fs (Fig. 2). We show these examples to illustrate conditions at the physical limits of imaging. For the two shorter x-ray pulse widths, only very small changes in the atomic positions have had time to develop. Hydrogen ions and highly ionized sulphurs are the first to escape the immediate vicinity of the protein (at 12 keV, the photoelectric cross section for sulphur is about fifty times larger than that for carbon). With the high-integrated x-ray intensity used in Fig. 2c, the molecule is destroyed before the 50 fs (FWHM) pulse is over. The 2 fs FWHM simulation was continued to 50 fs beyond the pulse, and in this case the molecule explodes as well, but only after the structural information has been gathered. These results are in agreement with other observations. Molecular dynamics simulations of the response of small van der Waals clusters of atoms ionized by intense visible fs laser pulses [17] also showed a delay of a few tens of fs prior to the creation of significant structural disorder, and when a fs x-ray pulse generated by a laser plasma was used to probe the dynamics of a rapidly heated organic sample [25], a delay of the order of 100 fs was observed prior to significant growth in disorder.

Figures 3a-c illustrate the calculated scattering intensities for a range of samples, using pulse parameters from Figs. 1b and 2b. The results show that a single tomato bushy stunt virus (TBSV) capsid [26] would scatter x-rays to atomic resolution with a 10 fs pulse containing $3x10^{12}$ (12 keV) photons in a 100-nm-diameter spot (Fig. 3a). The capsid particle of TBSV is a T=3 icosahedral nanocluster of 60 x 3 subunits. It is not a crystalline structure as it lacks translational symmetry. Looking at a tiny crystalline structure, Fig. 3b shows that high-resolution scattering may be obtained from a nanocrystal of 5 x 5 x 5 lysozyme molecules arranged on a rectangular primitive lattice. Molecules in the nanocrystal and subunits in TBSV were given an average root mean square conformational deviation of 0.2 Å to simulate imperfect conditions. While these structures diffract well with these pulse parameters, Fig. 3c shows that the same intensity would only be scattered to around 40 Å resolution from a single lysozyme molecule. For a comparison, Fig. 3d shows a planar section through the continuous molecular transform of lysozyme, shown here under ideal conditions without sample movement or damage. A more detailed analysis of maximum attainable resolutions in single exposures is given in Table 1 and Fig. 4. Figure 4 shows the landscape of damage tolerance in a broad parameter space around the initial LCLS parameters.

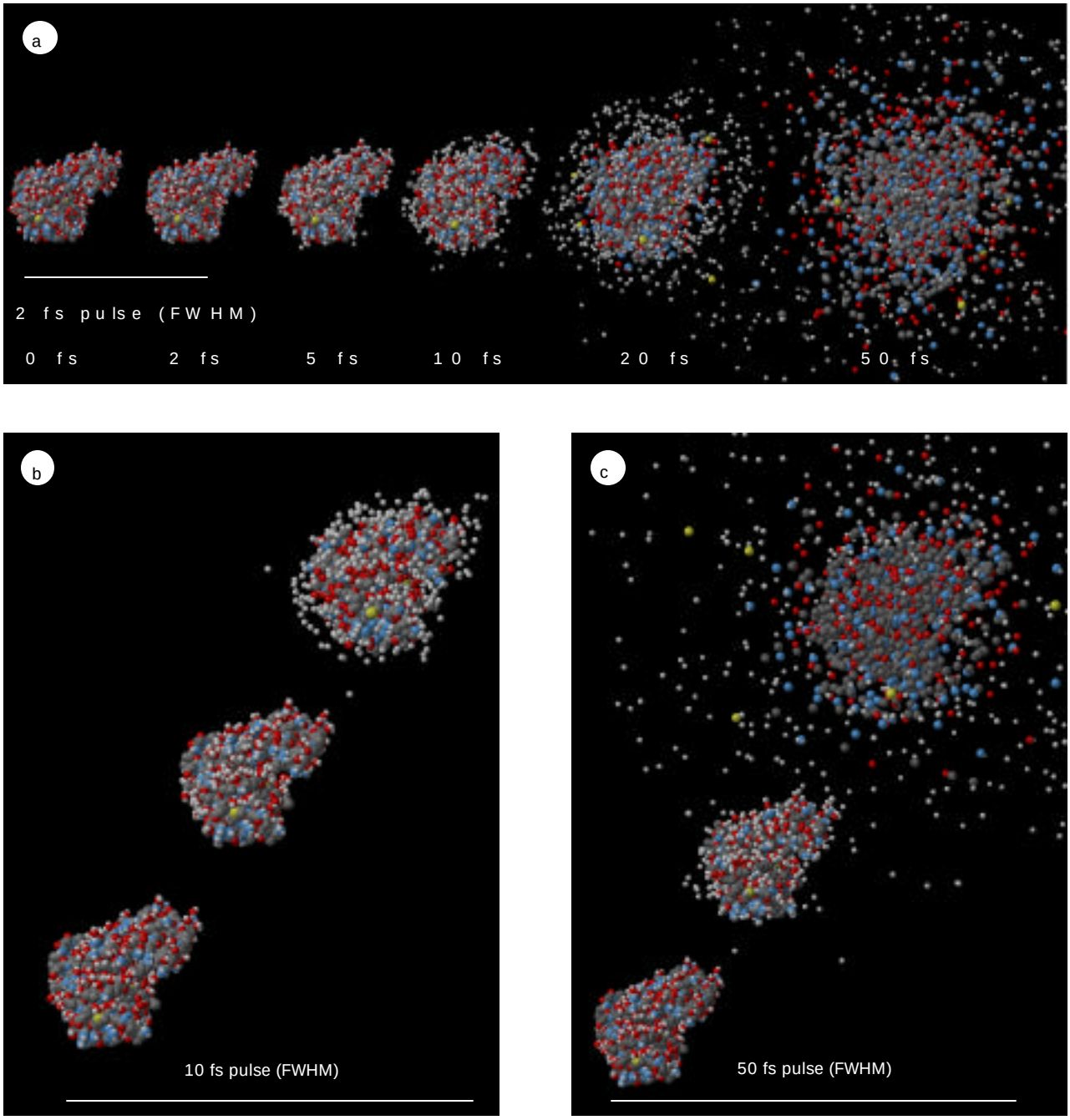

FIG. 2. Radiation-damage-induced explosion of T4 lysozyme (white: H, gray: C, blue: N, red: O, yellow: S). Integrated x-ray intensity was $3x10^{12}$ (12 keV) photons/100 nm diameter spot ($3.8x10^{6}$ photons/Å^2) in all cases. (a) Protein exposed to a 2 fs FWHM x-ray pulse, and disintegration followed in time. The atomic positions in the first two structures (before and after the pulse) are practically identical at this pulse length due to an inertial delay in the explosion. (b) Lysozyme exposed to the same number of photons as in (a), but the pulse FWHM is now 10 fs. The images show the structure at the beginning, in the middle, and near the end of the x-ray pulse. (c) Behavior of the protein during a 50 fs FWHM x–ray pulse. For a, b and c, R_{nucl} was 3%, 7%, 26%, and R_{elec} was 11%, 12%, 30%, respectively.

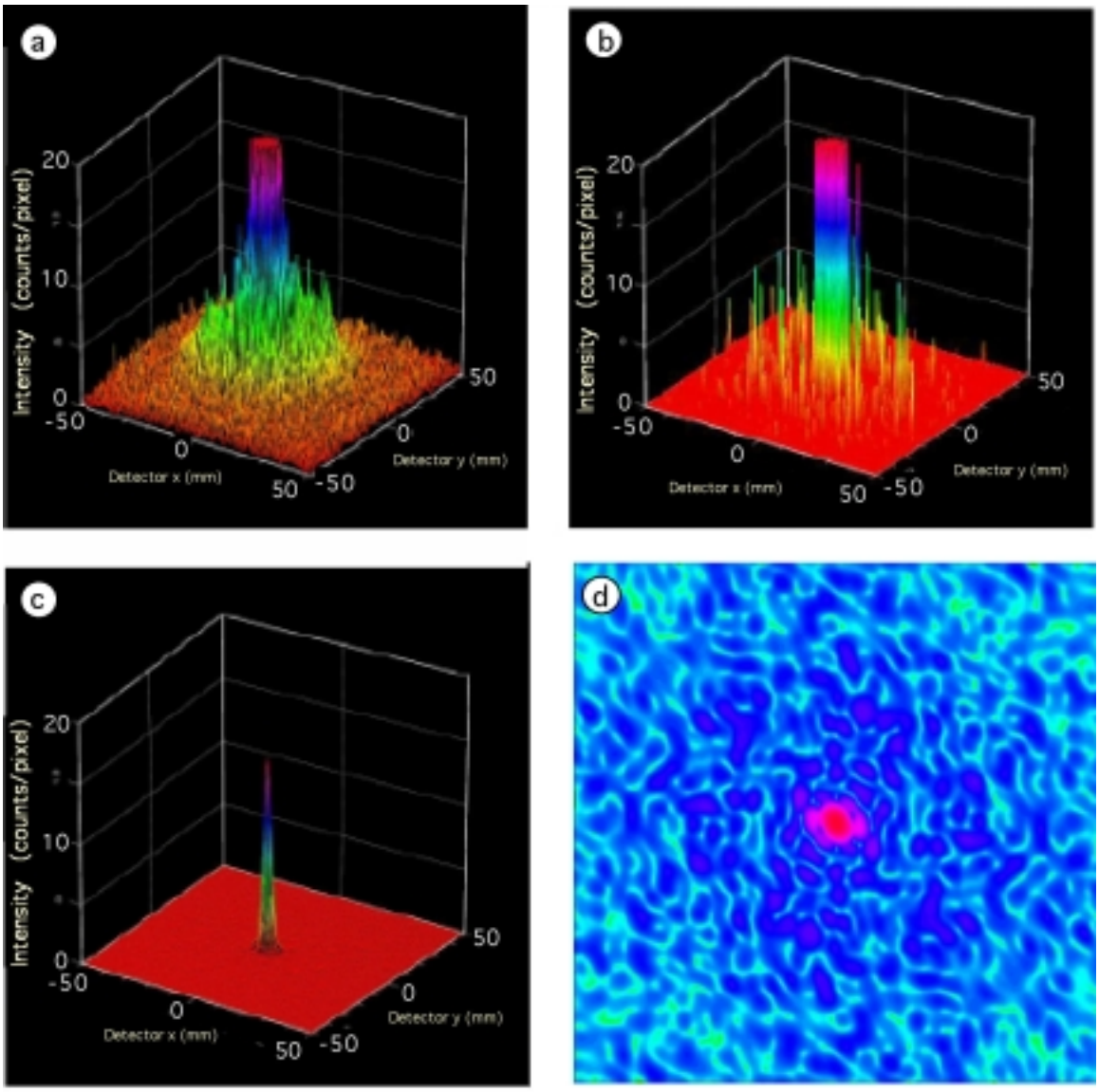

FIG. 3. Elastic scattering from a variety of samples. (a-c) Simulated diffraction images on a 128 x 128 pixel planar detector (100 mm x 100 mm) normal to and centered at the beam, and placed 100 mm from the sample. Background was not modeled, and 100% detective quantum efficiency was assumed. Integrated x-ray intensity = 3 x 10^{12} (12 keV) photons/100 nm diameter spot (3.8 x 10^{6} photons/Å^{2}). Pulse length = 10 fs. The resolution is 2.2 Å at the rim in (a-c). (a) Scattering from a single TBSV capsid. (b) Scattering from a 5 x 5 x 5 cluster of lysozyme molecules with an average root mean square conformational deviation of 0.2 Å to model an imperfect lattice. (c) Scattering from a single molecule of lysozyme. (d) The molecular transform (i.e., a simulated continuous scattering image) of a single T4 lysozyme molecule under ideal conditions without sample movement or damage. Resolution at the rim of this figure corresponds to 2.0 Å. Structure factor amplitudes are colored logarithmically (magenta: high, green: low). The section is perpendicular to the z-axis, and crosses through the origin at the center of the image, revealing centric symmetry.

D. The landscape of damage tolerance for biological samples

The structural information, which is theoretically recoverable from the sample during an exposure, can be quantified by the introduction of a weighted average agreement factor (R-factor, Eq. 2), which provides a direct assessment of the data quality. The R-factor is defined as:

$$R \equiv \sum_{\mathbf{u}} \left| \frac{K^{-1}\sqrt{I_{real}(\mathbf{u},\Omega)} - \sqrt{I_{ideal}(\mathbf{u},\Omega)}}{\sum_{\mathbf{u}}\sqrt{I_{ideal}(\mathbf{u},\Omega)}} \right| \quad (2)$$

where

$$K = \frac{\sum_{\mathbf{u}}\sqrt{I_{real}(\mathbf{u},\Omega)}}{\sum_{\mathbf{u}}\sqrt{I_{ideal}(\mathbf{u},\Omega)}} \quad (3)$$

Scaling factor K describes the relative scattering power of the sample (listed also in Table 1). Values for $I_{real}(\mathbf{u},\Omega)$ and $I_{ideal}(\mathbf{u},\Omega)$ were computed from molecular dynamics simulations by evaluating Eq. (1) from 60 snapshots of each MD trajectory. $I_{real}(\mathbf{u},\Omega)$ was derived from the time-dependent atomic coordinates, $\mathbf{x}_j(t)$, and scattering factors, $f_j(t)$, of a sample exploding in the x-ray pulse, while $I_{ideal}(\mathbf{u},\Omega)$ was determined from the reference molecular dynamics simulation of an unexposed sample. If the atomic scattering factors for the damaged sample are taken as unchanged from those of the parent atoms, then R provides information on the extent to which the average positions of the sample' s nuclei are perturbed by x-ray-induced damage ($R \equiv R_{nucl}$). If the degree of ionization of each atom is included when modeling the atomic (or ionic) scattering factors, then R provides information on the extent to which the elastically scattered radiation is perturbed by x-ray-induced damage ($R \equiv R_{elec}$). R_{nucl} depends only on the movements of atoms during an exposure, while R_{elec} depends both on the movements and on the changes in the electronic structure of atoms. It should be noted that, while R_{nucl} delivers useful insight into the explosion process, it is R_{elec} that corresponds directly to the quality of the data that would be obtained in an actual experiment.

Macromolecular crystal structures in the Protein Data Bank have crystallographic R-factors of around 20%. Many of the structures, especially those collected earlier on photographic film, represent data sets with merging R-factors in the 5-15% range. Taking the latter value as an arbitrary upper limit, we regard damage as acceptable if R_{elec} 15%. A survey of the landscape for damage tolerance (Fig. 4) shows many combinations of wavelength, integrated intensity, and pulse length where R_{elec} 15%. Initial LCLS parameters are marked. Figures 4a and 4b display contour plots of weighted average R_{nucl} and R_{elec} values for 12 keV photons as functions of pulse duration and the total photon flux. It can be seen that R_{nucl} and R_{elec} display different response dynamics since atomic positions do not change as fast as the electronic configuration of the atoms.

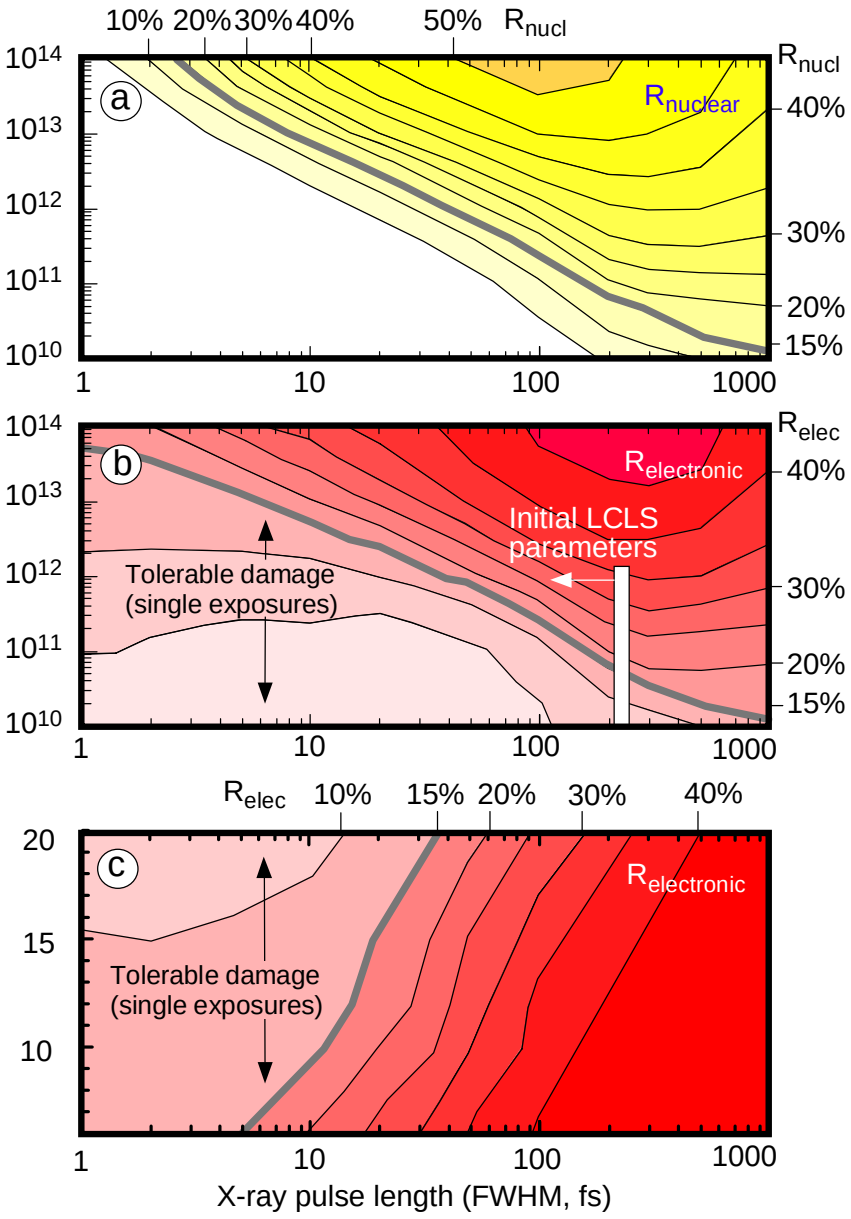

FIG. 4. The landscape of damage tolerance. Contour plots of the nuclear (R_{nucl}) and electronic (R_{elec}) weighted average R-factors (Eq. 2) as functions of the x-ray flux (I_o = the total number of photons/pulse/100 nm ø focal spot), pulse duration, and photon energy. (a) R_{nucl} for a 12 keV x-ray beam, illustrating the extent to which the average positions of the sample' s nuclei are perturbed by radiation damage. (b) R_{elec} for a 12 keV x-ray beam, illustrating the extent to which the information content of the elastically scattered x-rays is degraded due to radiation damage. We regard damage as acceptable if R_{elec} 15%, which is indicated by the gray line. (c) The variation of R_{elec} as the x-ray photon energy is changed, but the total number of elastic scattering events per carbon atom is held constant. These intensities were I_{tot} = 1.33 x 10^{12} (6 keV), 1.85 x 10^{12} (8 keV), 2.36 x 10^{12} (10 keV), 3.0 x 10^{12} (12 keV), 3.96 x 10^{12} (15 keV) and 6.0 x 10^{12} (20 keV) photons/100-nm-diameter spot, respectively.

Table 1 shows calculated limits of resolution at different points along the line of the "maximum tolerable damage" in Fig. 4b. The total dose delivered to the sample at either end of this line represents an increase of several orders of magnitude over the previously postulated limit of about 200 photons/$Å^2$ (i.e., 1.6 x 10^8 photon/100 nm focal spot) for conventional experiments at low x-ray intensities and cryogenic temperatures [1,5]. Increasing I_{tot} much above 5 x 10^{13} photons/spot is likely to be of little value even at very short pulse lengths, as above this dose, most of the sample's electrons are stripped from the atoms during the x-ray exposure (see values for the relative scattering power in Table 1). Thus, the total number of elastically scattered photons no longer increases linearly with increasing dose, and x-rays scattered from unbound electrons will contribute additional noise. With increasing x-ray energy, the ratio of elastic scattering events to damaging events becomes more favorable [14-16], and Fig. 4c shows that data quality improves as the x-ray probe moves to higher photon energies. This is due to a favorable change with wavelength of the ratios of elastic, inelastic, and photoelectric cross sections in biologically relevant elements.

TABLE 1. Calculated limits of resolution. Averaging techniques may provide atomic resolution below the dashed line.

Pulse duration	1 fs	5 fs	10 fs	50 fs	100 fs	230 fs (LCLS, initial)	
Photons/pulse/100 nm spot (1) (from Fig. 4b, grey line)	$5x10^{13}$	$1x10^{13}$	$5x10^{12}$	$8x10^{11}$	$3x10^{11}$	$5x10^{10}$	
Relative scattering power	0.32	0.53	0.71	0.96	0.97	0.99	
Single lysozyme molecule	15Å	24Å	26Å	30Å	>30Å	-	1 ph/pixel (2)
	>30Å	>30Å	>30Å	>30Å	>30Å	-	9 ph/pixel (3)
2x2x2 cluster of lysozymes	2.5Å	3.1Å	4.8Å	12Å	17Å	25Å	1 ph/pixel (2)
	6.5Å	12Å	16Å	30Å	>30Å	>30Å	9 ph/pixel (3)
3x3x3 cluster of lysozymes	<2.0Å	<2.0Å	<2.0Å	3.0Å	6.5Å	12Å	1 ph/pixel (2)
	2.2Å	3.0Å	3.0Å	12Å	17Å	30Å	9 ph/pixel (3)
5x5x5 cluster of lysozymes	<2.0Å	<2.0Å	<2.0Å	<2.0Å	<2.0Å	2.5Å	1 ph/pixel (2)
	<2.0Å	<2.0Å	<2.0Å	2.9Å	3.9Å	5.0Å	9 ph/pixel (3)
Single viral capsid (TBSV)	<2.0Å	<2.0Å	<2.0Å	<2.0Å	<2.0Å	2.4Å	1 ph/pixel (2)
	<2.0Å	2.5Å	2.5Å	4.7Å	22Å	30Å	9 ph/pixel (3)

With reproducible samples:
(1) Max. tolerable integrated intensity values were taken from the grey line in Figure 4b.
(2) Resolution may be extended beyond this limit by averaging, if orientation known.
(3) Information extending to this limit could be used for determining sample orientation.

E. Extending resolution through averaging

Averaging techniques exploit the fact that photon counts from the structural signal grow more rapidly than counts from an incoherent background (sources of noise here include inelastic scattering, bremsstrahlung from photoelectrons colliding with instrument walls, and an imperfect sample environment). As emphasized in the introduction, the achievable resolution for biological specimens is fundamentally limited by damage. If reproducible samples can be obtained in large numbers and they can be oriented parallel to each other, their diffraction patterns add coherently or incoherently. The damage on each sample is therefore reduced. The best known example is, of course, diffraction by crystals, where the diffraction patterns add coherently in directions where the Bragg condition is satisfied and destructively in all other directions. There are several known

methods to obtain an incoherent superposition of diffraction patterns: x-ray and photoelectron holography operate on ordered samples but use incoherent sources of radiation. Recent proposals to obtain similar results include recording the diffuse scattering from a crystal that is a mixture of two species, and the use of partially coherent x-rays on crystals.

It can be shown that the resolution for reproducible samples can be increased even if they cannot be oriented parallel to each other. The technique, widely practiced in electron microscopy, is based on obtaining individual images of the samples at low doses of irradiation and consequently at very low signal-to-noise ratios, then numerically aligning them and averaging the aligned images [27-30]. Averaging exploits the fact that, once the images are numerically aligned, the signal adds linearly from each sample while the noise and background average out. The result is the sharing of the damage, similar to the crystal techniques described above. One could ask the question why aligning images needs less signal than obtaining an image. There are two reasons for its advantage. First, the image is three-dimensional and the alignment is two-dimensional—there are essentially n^3 resolution elements in a volume, while the orientation is determined by n^2 directions. Second, in order to get a good image, one has to use many gray levels while the alignment essentially can be done on a single either/or basis. Multi-image alignment and averaging methods developed in electron microscopy have produced substantially increased resolutions, e.g., for the ribosome [29]. With particles displaying high symmetry, resolution can be extended further by exploiting the symmetry of the structure [31,32]. One should note that averaging procedures can only be applied when a reproducible sample scatters a sufficiently large number of photons for its orientation to be determined. Larger samples scatter more x-rays (even without internal symmetry), and thus their orientation is easier to determine than the orientation of small molecules (one has to find the sample to begin with). Numerical alignment and averaging procedures [3,30,29] can be adopted to the planned studies with x-rays (the molecular transform of a three-dimensional object is another three-dimensional object, and numerical procedures developed for electron microscopy can be used to obtain a three-dimensional reconstruction from individual sections).

F. Sources of background

We anticipate the following key sources for background in the images recorded on the detector:

(1) *Detector noise ("dark current"):* This is probably not a significant problem. Today, less than one photon/pixel/exposure and a dynamic range of 4-5 orders of magnitude are possible on CCD detectors.

(2) *Scattering from gas molecules in the beam path:* Everything will be imaged in the beam path, and therefore the experiments need reduced pressure. At 10^{-9} mbar pressure, over a 100 mm free beam path, a beam of 1 μm^2 cross section will hit about three contaminant nitrogen molecules at room temperature. FT-ICR mass spectrometers usually operate at 10^{-10} mbar, and we could tolerate 10^{-8} mbar or slightly worse.

(3) *Debris from the Coulomb explosion:* Debris are electrons and positively charged ions emitted (nearly) spherically from the sample. Due to their charged nature, the flight path of the debris can be controlled, and we envisage using electric and magnetic fields to guide them away from the detector.

(4) *Bremsstrahlung from photoelectrons hitting the instrument wall:* This, again, is probably not a significant problem as the energy of this radiation is significantly lower than the photon energy in the x-ray pulse.

(5) *Inelastically scattered x-ray photons of various energies:* These photons represent around 3% of the total scattered x-ray intensity, have a broad energy range, and will form a low and smoothly varying background in each exposure.

(6) *Coherent scattering from free electrons:* This is probably not a significant problem. Low intensity is expected only from those electrons that are in the beam. These electrons will scatter x-rays in the direction of the direct beam (similar to a very high B-factor). It is unlikely that this radiation will contribute to background on the detector surface except in an extremely narrow forward direction.

(7) *Weak incoherent scattering from free electrons.*

(8) *Noise from the machine:* (i) Neutron background, (ii) bremsstrahlung (around 10 GeV from gas molecules along the path of the electron bunch in the machine), (iii) inductive fields created by the electron bunch as it is deflected and dumped at the end of the undulator magnet. The background originating from the machine could be reduced by moving the experimental station far away from the magnets.

IV. METHODS FOR PHASING

A number of ways exist for recovering phases in the planned experiments, including the oversampling of continuous molecular transforms [33-35], holographic imaging methods [36-40], holographic data evaluation methods [37], classical methods of crystallography, and techniques for phase extension from lower resolution electron/x-ray cryomicroscopy images.

The low-resolution part of an image is generally important in phasing, and, therefore, arrangements will be made to record the extremely low-resolution data in the planned experiments (described below, see also Fig. 5).

A. Oversampling

The main phasing question is how to determine phases when we do not have a crystal (there being a rich literature on phasing when one has a crystal.) The key thought that needs conveying here is the actual *advantage* that the noncrystal presents over a crystal, of allowing full access to the structural transform. Recent results based on oversampling of continuous molecular transforms in x-ray crystallography include papers from Miao *et al*. [41], Sayre *et al*. [42], Szöke [34], and Miao and Sayre [43]. Other methods based on an oversampling of the molecular transform include multicrystal averaging and the exploitation of noncrystallographic symmetry for phasing. The highest resolution applications of x-ray imaging have been traditionally limited to crystalline samples. Miao *et al*. [35] have demonstrated imaging and phasing (at around 75 nm resolution) of a noncrystalline sample, consisting of an array of gold dots, by measuring the soft x-ray diffraction pattern from which an image was reconstructed. The crystallographic phase problem could be overcome by oversampling of the diffraction pattern, and the image was obtained using an iterative algorithm. It was shown on simulated data [34] that a three-dimensional image can be perfectly reconstructed from a twice-oversampled diffraction pattern of a protein.

The sampling theorem of Shannon assures us that a function with a finite bandwidth is completely defined by its sampled values if they are sampled fine enough. It was noted by Sayre [44] that the Bragg conditions are equivalent to a critical sampling of the diffraction pattern. This means that, if the phases of the reflections are known, the electron density can be reconstructed

everywhere, but any missing information introduces ambiguity into the solution of a crystal structure. This theme was further expanded by Daubechies [45] who emphasized the underlying symmetry: Undersampling introduces ambiguity, critical sampling produces a representation of the electron density that converges very slowly, and oversampling allows a rapidly convergent representation. We quote Bricogne' s remarks on this matter [46]: “Thus the loss of phase is intimately related to the impossibility of intensity interpolation, implying in return that any indication of intensity values attached to non-integral points of the reciprocal lattice is a potential source of phase information.” In other words, the phase problem is somewhat different for noncrystals and crystals. When the specimen is noncrystalline, the diffraction pattern is continuous and this pattern can easily be oversampled, i.e., sampled more finely than the Nyquist frequency (the inverse of the size of the diffracting specimen or that of the unit cell in a crystal). Oversampling of continuous diffraction patterns can be used to retrieve phase information in crystallography [44]. Oversampling is also widely used in radio-astronomy for image reconstruction and in all forms of holography. New possibilities may, however, emerge with very small crystals (nanocrystals) in the LCLS beam (see section on nanocrystals).

B. Holographic data processing methods

Based on model calculations [37,38], Faigel and coworkers have shown that direct three-dimensional imaging of atoms is feasible by holographic reconstruction. Their subsequent studies utilized both holographic data collection and holographic data evaluation methods to produce the first atomic resolution structure derived by x-ray holography [39]. In the first instance, we will use holographic *data evaluation* procedures to extract structural information from *conventional* diffraction and scattering images of an unknown molecule attached to a known core structure (e.g., an icosahedral virus). The known core structure can be treated as the reference structure. Equations have been derived [37,40,47,48,49] for finding an unknown part of the electron density when part of the structure is already known. These equations are based on the similarity of the x-ray diffraction pattern to a hologram. The x-ray field scattered by the known part of the structure is identified as the holographic reference beam. It interferes with the waves scattered from the unknown part of the structure, and the interference pattern contains phase information that can be exploited to recover fully the unknown part of the structure. Experiments support this theory and show that holographic data processing methods represent a potentially viable alternative to conventional Fourier methods in structure determination [50,51].

V. SAMPLE HANDLING

With ultrasmall samples, standard procedures for sample selection, characterization, and handling will no longer be applicable. Everything within the LCLS beam path will be imaged, including the sample holder. We are developing novel “container-free” methods based on spraying techniques [52-57] to select and rapidly inject single hydrated molecules, nanoclusters of molecules and larger particles (e.g., viruses, ribosomes, or even small living cells) into an intense x-ray beam. Another possibility that will be explored is to adopt techniques from electron cryomicroscopy and embed the sample molecules into a thin layer of vitreous ice.

In a focused LCLS beam, no biological sample is likely to survive more than one encounter with an x-ray pulse (Figs. 1, 2, 4). One consequence of this is that with small nonreproducible samples, it will be possible to record only projection images. Depth may be improved in such images if holographic imaging were possible. With reproducible samples, sorting and averaging of images is possible, and this offers two key advantages: 1) three-dimensional structural

reconstitution will be possible, and 2) the attainable resolution can be enhanced substantially by averaging techniques. The achievable resolution depends on the uniformity of objects in the sample, which can be improved by the mass-spectrometric sample selection and injection procedures outlined here.

A. Spraying techniques

The average distance between neighboring macromolecules inside a cell (water content: 70-80%) is only a few Å longer than the average distance between neighboring molecules in the three-dimensional lattice of a protein crystal (average water content 50%). Nevertheless, in going from the solution to the crystalline state, it is reasonable to anticipate certain changes in the structure, and the same may be true for microdroplets in the gas phase. We note, however, that some biology does take place in the gas phase, and transmission in the gas phase is the most common route for infections. New container-free methods are being developed [56] based on microdroplet techniques for the characterization, selection, and injection of single molecules, nanoclusters of molecules, or small living cells into intense x-ray pulses while maintaining the structural integrity of the samples at cryogenic temperatures. Cryogenic temperatures can be reached very rapidly through the supersonic expansion of a carrier gas (e.g., SF_6) in the spray. Techniques from mass spectrometry have been adopted to characterize, select, and inject well-defined clusters of proteins for structural studies in the LCLS beam. The sample entering the vacuum chamber will be in random orientation, encapsulated in a microdroplet [58,59]. The microdroplets can be dried to a desired level before interacting with the beam. A beam of sample molecules/particles will be injected into the 120 Hz pulse train of the LCLS. Figure 5 shows the suggested experimental arrangement. The second detector, placed at some distance behind the first one, serves to provide high-detail resolution for measuring the strong forward scattering pattern (see, e.g., Fig. 3a) of noncrystalline samples. We envisage using a system that can be read out at the frequency of the LCLS pulse train. Individual pulses will either hit or miss molecules/particles in the sample stream. Hits could be verified through the measurement of the x-ray scattering intensity together with the UV/VIS fluorescence emission from the exploding sample. These measurements can also be correlated with a simultaneous mass spectrometric analysis of debris and by numerical evaluation of the scattering image recorded on the detector.

The latest mass spectrometry technology is required for preserving noncovalent macro-molecular assemblies involving nanoflow sample introduction at lower temperatures into an electrospray source. This introduction system provides a particularly “gentle” environment for the analysis of proteins such that surface water molecules can be retained during the analysis of these complexes [52,53]. We propose injecting samples from the mass spectrometer directly into the x-ray beam. Recent experiments have demonstrated that virus particles retain their three-dimensional structure and remain capable of infection after electrospray ionization and collection after passing through the mass spectrometer [54-56]. Intact ribosomes [57] may be analyzed by nanoflow electrospray techniques. An exciting possibility is to select and store desired particles in ion-trapping devices, then inject selected particles into the beam, thus providing a unique opportunity to observe them under a variety of different conditions. To date these conditions involve the introduction of volatile reagents, such as heavy water, to obtain structural data based on H/D exchange rates, and collision with gas molecules to provide protein fragments. We intend to investigate sample selection and storage procedures for large clusters with Fourier transform ion cyclotron resonance mass spectrometers (FT-ICR-MS). In parallel with these studies, experiments with electrospray techniques coupled to orthogonal time-of-flight technology to enhance transmission and signal handling will be carried out. This technol-

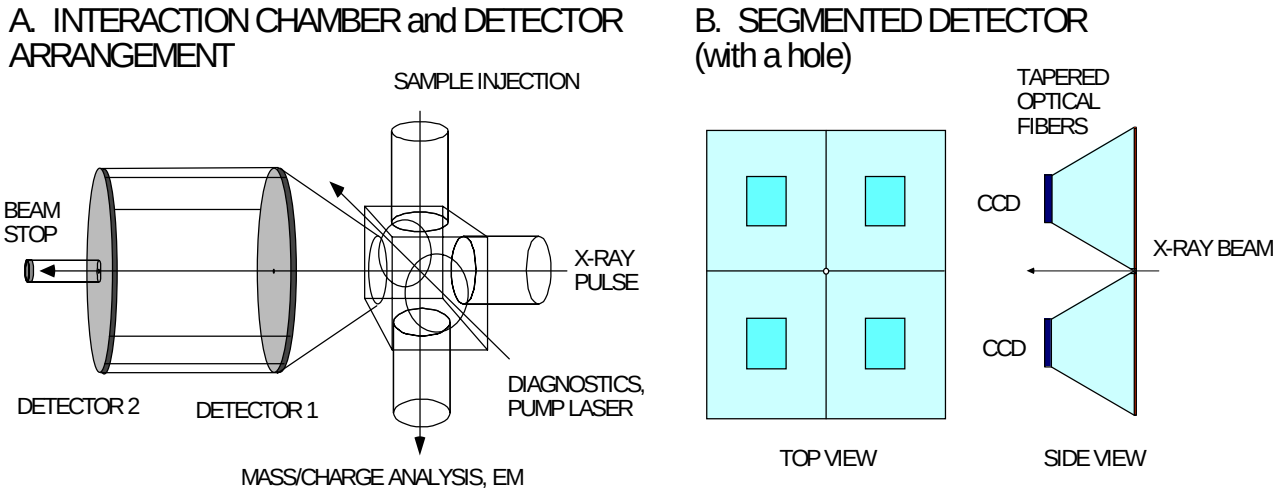

FIG. 5. Suggested detector and experimental arrangement. (a) Sample injection, diagnostics, mass measurement, tandem x-ray detectors, and backstop geometry. (b) The four-segment CCD detector with a hole. The distance between the two detectors in (a) is variable. An "intelligent backstop" measures integrated intensity for each x-ray pulse.

ogy has high sensitivity and a potentially unlimited molecular weight range. By fine tuning drying conditions and the path lengths of the particles before meeting the radiation pulse, similar techniques could be used for introducing small living cells into intense photon beams. Results so far suggest that conditions in the spray can be similar to conditions in electron cryo-microscopy (low temperature, high vacuum, hydrated samples). However, mass spectrometry has the potential to select large samples based on mass differences of a couple of daltons. The marriage of structural methods with mass spectrometry will open up completely new horizons in studies of structure function, solvation, and reaction dynamics in both biology and chemistry.

B. Samples embedded in vitreous ice

Cryomicroscopic techniques could be particularly suitable for studies where a controlled sample rotation is necessary, e.g., in the planned "tomo-holographic" experiments on intact cells and cell organelles using the unfocused, coherent beam of the LCLS. Existing electron microscopy equipment can be adopted for similar studies in an x-ray beam. Sample molecules and particles may be embedded in a thin layer of vitreous ice of a few hundred Å in thickness. Prior to an exposure, the sample(s) of interest may be located by UV/VIS fluorescence techniques and, once found, moved into the path of the x-ray pulse, using programmable positioning devices. With this approach, the complete repertoire of methods in electron cryomicroscopy will become available for x-ray experiments. Vitreous ice surrounding the sample will contribute to background; nevertheless this method may be the method of choice for large samples like intact eukaryotic cells.

VI. FIRST X-RAY EXPERIMENTS

A. An overview

There is a general class of experiments that utilizes the short time structure and the potential for very large intensities of the LCLS beam and lead up to the exciting new regime outlined in the

first sections. It is immediately clear that small crystals, nanoclusters, and two-dimensional (2D) crystals can be studied at 200 fs time resolution from the beginning. In the following sections we will outline some exciting biological problems that become doable this way. Note that the coherence and the saturation of the LCLS plays only a secondary role in these experiments but will be important later.

It was emphasized in the introduction that damage by the incident radiation is the ultimate limit to the resolution of imaging techniques in biological molecules. It is ~ 200 photons/Å^2 at 10 keV incident photon energy in conventional experiments. The primary damage is caused by the ~10 keV photoelectrons and the ~ 250 eV Auger electrons that are absorbed in the sample, causing secondary ionization and, eventually, chemical damage. It is accepted wisdom that the damage in conventional electron microscopy is about 1000 times more benign with large samples than damage with x-rays. This would imply that single-particle imaging techniques would yield 10-fold lower resolution by x-ray scattering. There are three mitigating factors in favor of x-rays. First, the scattering geometry of x-rays allows large-angle data collection, and the clean and simple geometry avoids distortions in the image. Second, if small particles can be used, the primary photoelectrons deposit only a small fraction of their energy and the damage should be ameliorated by ~ 20-40 fold. Third, time-honored techniques of attaching heavy atoms to clusters should increase the signal-to-noise ratio of single-particle images.

In order to utilize the advantages outlined in the previous paragraph, two additional developments are needed: focusing of the beam to about 0.5 μm, and the development of single-particle injection techniques. The latter is well advanced in this partnership. We anticipate that very mildly ionized droplets will be injected into the focused beam just in time. When mild focusing of the beam becomes available (e.g., the focusing of the projected 10^{12} photons in one pulse into a focal diameter of 1/2 micron, giving a flux of 2 x 10^4 photons/Å^2 at the focus), single-particle images can be obtained using averaging techniques similar to those used in electron microscopy. This should open the door to virus structures, including their genomes; to the study of membrane proteins; and to very high time-resolution studies of other, known structures.

In summary, we will argue below that new and exciting biological problems will be open for investigation from the first day the beam at LCLS becomes available. We foresee that our interim technical efforts in sample handling, attaching proteins to viruses, and developing algorithms for single-particle imaging will fully complement developments with the LCLS. The experiments outlined below represent major research lines far beyond the limits of currently available methodologies. We also hope that new research areas may emerge in a field as explosive as biology today by the time LCLS becomes available. Shortening the LCLS pulse length would be a key improvement in all planned applications, including those described in the biological proposal. With shorter pulses, tighter focusing, very fast detectors and development of accurate injection techniques, biomolecular imaging should reach the extreme regime outlined in the theoretical part of this proposal.

B. Nanocrystals

Nanocrystals are open periodic structures with submicron dimensions. The LCLS with its planned initial parameters may offer completely new avenues for structural studies on nanocrystalline samples. No such studies are currently possible. When a crystal is small, the Bragg peaks are broadened and the intensity between the Bragg peaks is not negligible. Both the Bragg peaks and the intensity between the peaks carry structural information. The oversampled diffraction pattern visible between Bragg peaks can directly provide phase information. Figure

6a shows a two-dimensional crystal with 15 x 15 unit cells (overall array size = 75 nm x 75 nm), and Fig. 6b shows the continuous (oversampled) diffraction pattern visible between Bragg peaks.

Applying positivity constraints to eliminate the conjugate ambiguity (cf. twin image problem in holography), phase information can be obtained from the oversampled diffraction pattern. Based on Fienup' s theorem [60], an iterative algorithm has been developed [41,43] and is available for the planned experiments. Computer phasing experiments demonstrate the feasibility of this technique. By employing a finite support, a random phase set, and the positivity constraints on the real part of the electron density, it was possible to reconstruct the electron density of the whole small crystal in an iterative process [43]. It could be shown that the reconstruction of the structure from the diffraction pattern was still possible with deteriorating signal-to-noise ratios of 20, 10, and 5.

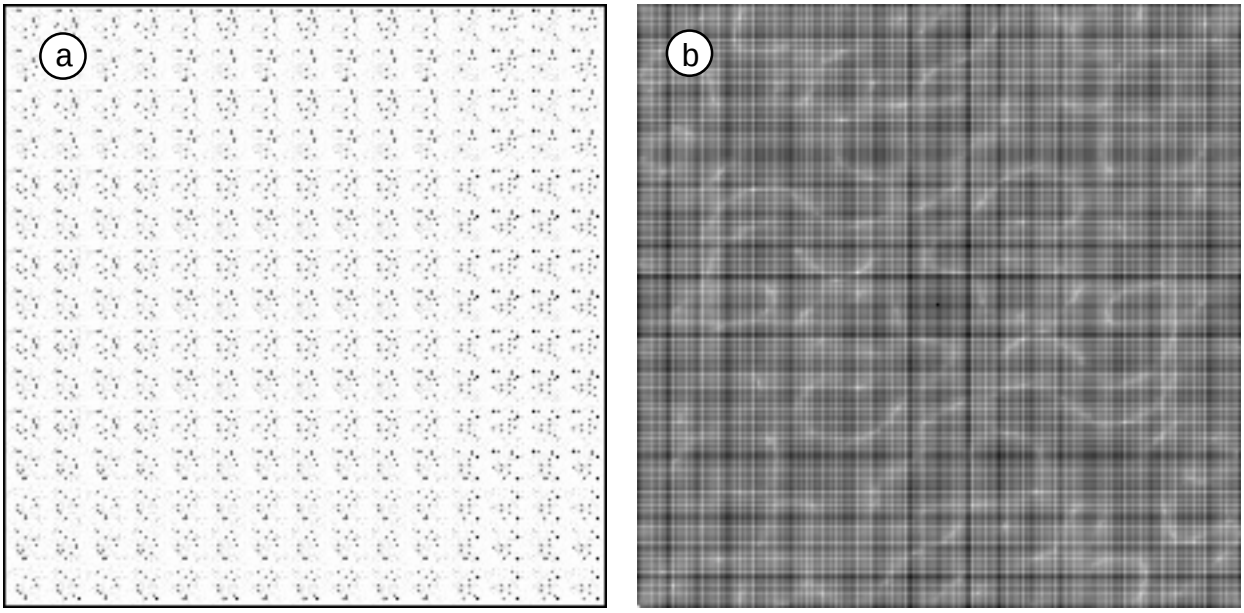

FIG. 6. Oversampled diffraction pattern from nanocrystals. (a) A two-dimensional crystal with 15 x 15 unit cells. Unit cell dimensions: 5 nm x 5 nm; each unit cell contains 25 dummy atoms. Overall array size = 75 nm x 75 nm. (b) Simulated continuous (oversampled) diffraction pattern visible between Bragg peaks (intensity is represented on a logarithmic scale).

C. Two-dimensional crystals of macromolecules

Various estimates show that there are at least as many different membrane proteins as soluble proteins, yet there are only a handful of structures known today for integral membrane proteins compared to almost 14,000 structures for soluble proteins. An understanding of the structure-function relationships in membrane proteins would make invaluable contributions to biochemistry, physiology, and medicine, and would produce a substantial socioeconomical impact (about 70% of all known drugs target membrane proteins).

Two-dimensional crystals of membrane proteins have been used for structural studies in electron cryomicroscopy (see, e.g., ref. 32). Such arrays may also be obtained from a number of other proteins by epitaxial crystal growth methods. The intensity of the scattered x– rays from a small two-dimensional array was simulated, using 300 x 300 copies of a simple test protein (lysozyme)

in the calculations. These protein molecules were arranged on a primitive 2D lattice with 32 Å lattice spacing in two perpendicular directions. The surface area of the array was about 1 μm x 1 μm, and the size of the x-ray beam was selected to match this area. Pulse intensity (4×10^5 photons/Å^2) was chosen to ionize about 10% of all non-hydrogen atoms in the sample. The results show diffraction rods with 200-400 photons/rod at 3-4 Å resolution (Fig. 7). Inelastic scattering was estimated to be around 2 photons per 0.3 mm pixel (sample-to-detector distance = 100 mm) at this resolution. Integration of the diffraction rods requires images with different sample orientations to be recorded, and this could be achieved by merging data from several randomly oriented samples. This procedure could provide structural data on membrane proteins in single bilayers. We will use this technique to obtain structural data on a variety of key membrane proteins.

D. Nanoclusters for structural studies

In contrast to nanocrystals (which are small but open periodic structures with translational symmetry), nanoclusters are closed structures, which may be periodic (like oligomeric proteins or viral capsids) but have no translational symmetry. Such nanoclusters come in very well-defined sizes (see, e.g. Lin *et al*., [61]). We are developing procedures for assembling proteins of choice into regular nanoclusters for subsequent structural studies. Methods are available for the specific attachment of target proteins onto the surface of regular templates, e.g., icosahedral virus capsids. These methods will be applied to structural studies on soluble and membrane proteins at the LCLS. Assembling protein molecules into nanoclusters will increase the intensity of scattered radiation from otherwise small proteins (see Fig. 3a). Using a modified TBSV, containing 180 copies of a specific binding site, we have shown quantitative binding of foreign proteins to the surface of the virus particles. We wish to use modified viruses to construct well-defined nanoclusters of a number of different proteins, including membrane proteins. Expected outcome: structures for “uncrystallizable” proteins attached to the surface of regular templates.

E. Virus structures and the structure of viral genomes

No three-dimensional structure is available for any genome today. Small spherical viruses are among the simplest replicating systems in biology, yet the packing of the nucleic acid inside the capsid, and the factors affecting viral assembly, stability, and disassembly are still not understood. Only a very superficial picture is available today on the packing of the genetic material in intact viruses [62-65]. This is due to the fact that the nucleic acid inside a viral capsid does not follow the symmetry of the outer capsid; when crystallized, the outer shell obeys the space group symmetry, while the inner material does not. As a consequence, the image of the otherwise tightly packed nucleic acid inside the virion is rotationally averaged over some angular range. Viruses are big (around 10-100 nm diameter) and as a consequence give relatively strong scattering patterns (Fig. 3). Initial trials will be performed on the MS2 virus (a bacteriophage). This virus is safe, it is well characterized by mass spectrometry [56], and the structure of the protein capsid is known. From images collected, we propose holographic reconstruction to recover the structure of the inner part (the genome) of the virus. Other methods of phasing will also be explored (e.g., oversampling, [35,34], or classical methods based on derivatives). Further experiments will focus on the assembly/disassembly of the virus. Similar studies will be performed on other viruses. Of particular interest are viruses that cannot be crystallized (e.g., the human immunodeficiency virus, the herpes simplex virus, and many other enveloped viruses).

X-ray studies on viral particles in the gas phase (or in vitreous ice) could open up ways to capture elusive intermediates within the "life cycle" of a virus. An understanding of the functional dynamics of viruses may offer a means to interfere with infection. Experiments will capture dynamic events, e.g., steps in the assembly and disassembly of the virus, and studies on key initial steps in a viral infection.

F. Structural studies on single protein molecules

The need for crystals for high-resolution structural studies is a serious limitation today. Currently, this excludes a very large proportion (>60%) of proteins from structural determination and hinders progress in the area of structural genomics. Structures accessible today for analysis do not represent a random selection of proteins, and knowledge gained on "crystallizable" structures may not automatically translate into knowledge about "non-crystallizable" structures. If and when sufficiently short pulses (20-100 fs) and a reasonably tight focus (around 100-nm-diameter focal spot) will become available, studies on large single individual molecules (with molecular masses in excess of 100,000 dalton) may become routinely possible. In order to *prepare* for such experiments, we intend to start testing the behavior of individual proteins in the LCLS beam. In the tests, proteins of different molecular masses and oligomeric states will be selected and injected into the x-ray beam. We intend to analyze their fragmentation patterns in order to verify theoretical predictions. Success in this area may trigger a new revolution in life sciences.

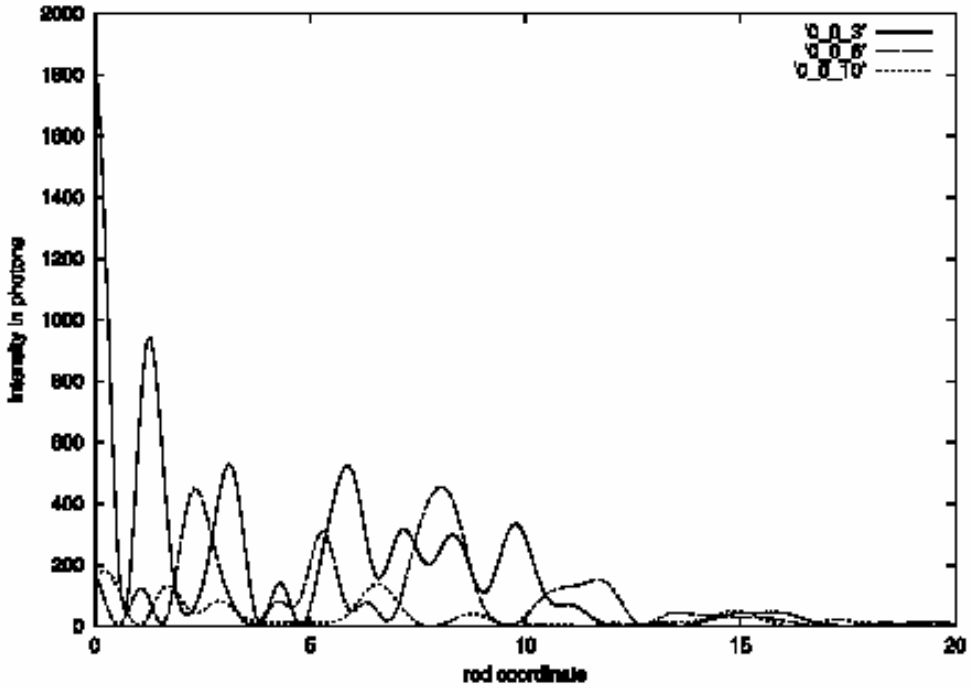

FIG. 7. Predicted intensity distribution from a two-dimensional protein array. Surface area: 1 μm^2. Lattice spacing: 32 Å in two perpendicular directions. Array size 300 x 300 molecules of a simple test protein (lysozyme). Diffraction rods with as much as 200-400 photons/rod can be observed at 3-4 Å resolution.

G. New horizons in time-resolved experiments

Biological function is a four-dimensional property. Time-resolved studies on structure, function and dynamics at the LCLS could cover catalysis, protein folding, nucleic acid folding, the assembly/disassembly of biomolecular complexes, viral uncoating, viral infections and so on. Such studies will first become possible on nanoclusters and nanocrystals as they require less stringent beam parameters from the LCLS than studies on single molecules. Later on, these experiments may be extended to individual biomolecules or cells.

1. Photochemical reactions

Marriage of femtosecond laser spectroscopy with femtosecond time-resolved structural studies will be possible. This area is described in more detail in the proposal on femtochemisty at the LCLS.

2. Diffusion triggering and stop-flow studies

While certain key reactions in life are photochemical, most enzymes participate in diffusion-dominated processes with their reactants and partners. Time-resolved structural studies on diffusive processes in crystalline enzymes are difficult due to problems with mixing enzyme and reactant. Structural studies are only possible on intermediates, which accumulate transiently in the crystal during a reaction. This requires a relatively fast binding followed by a relatively slow reaction. Due to the generally lower activity of crystalline enzymes, uniform catalysis can often be triggered by diffusing reagents (e.g., substrates) into crystals. However, the speed of diffusion and ligand binding sets an upper limit to the speed of reactions that can be analyzed this way. In an average-sized protein crystal (0.2-0.3 mm overall dimensions), half-saturation binding with small ligands can be reached within about a minute. One obvious possibility for lowering diffusion barriers is to reduce the sample size and to use nanoclusters or nanocrystalline assemblies of enzymes for stopped-flow-type time-resolved experiments. With very small samples, the vast majority of solution techniques and methodologies will suddenly become available for time-resolved structural investigations. Kinetic studies based on diffusion triggering will become possible on micron- and submicron-sized assemblies, and they may diffract to high resolutions in the LCLS beam (see Table 1). A new nanocluster/nanocrystal would be needed for each exposure. We foresee that container-free sample-handling methods based on spraying techniques will open up new horizons here. A microdrop-based stop-flow apparatus has recently been developed by one of us (C. Robinson), linking stopped flow and spraying methods. The overall impact of these developments on structural and functional biology is immeasurable.

H. X-ray diffraction tomography of whole cells

A challenging problem in cell biology involves the imaging of whole, eukaryotic cells at high resolution and with good resolution depth. While impressive advances are being made in light microscopy using confocal, through-focus deconvolution, interferometric, and patterned illumination techniques for labeled specimens, these techniques are not able to go below about 100 nm resolution, and one is not able to image the overall architecture of an intact cell at the same resolution as the labeled structures. At the same time, the use of energy filters has made 10-nm-resolution electron tomography of frozen hydrated specimens possible but only on specimens thinner than about half a micrometer. X-rays offer an opportunity for imaging whole, eukaryotic cells of 10 micrometer thickness in a frozen hydrated state and at high resolution. Advances in

zone-plate optics are making it possible to image such specimens at 30 nm or better resolution. However, the complexity of a cell is such that one will have considerable overlap of structures in a single projection; for this reason, groups at Stony Brook and Goettingen have demonstrated tomographic imaging of frozen hydrated specimens.

A challenge with these existing approaches is that they have relied on absorption-contrast imaging within the depth-of-focus limit of a zone-plate optic. Absorption contrast is strongest at photon energies of about 0.5 keV, while at higher energies phase contrast completely dominates. At 0.5 keV, the depth of focus of zone plates with 30 nm transverse resolution decreases towards 1 μm; as a result, out-of-focus planes will contribute phase-contrast information to the in-focus absorption-contrast information recorded in an image. This is quite unlike the situation in through-focus deconvolution fluorescence microscopy, where one records a signal that is always dependent on illumination intensity rather than phase. At the same time, recent demonstrations of the reconstruction of images from diffraction patterns have also involved a restriction that the net phase shift through a specimen be no more than about $\pi/2$ radians, which again restricts one to the imaging of specimens no more than a few micrometers in extent.

Our partners from the State University of New York at Stony Brook are developing a diffraction tomographic microscope to circumvent these limits. The proposed experimental method provides uniformly good depth resolution. The microscope includes a holder for the frozen hydrated specimen that can be tilted up to +/- 80 degrees in either direction. At each rotation, a zone plate will be used to magnify two holograms (from different near-field distances from the specimen) onto a CCD camera. One can then reconstruct the complex wavefield at various depths through the specimen in one viewing direction using back propagation rather than the back projection approach used in conventional tomography. By combining many viewing angles, one can build up a three-dimensional representation of the complex refractive index of the object and thus obtain a faithful three-dimensional (3D) image without regard to the depth of focus of the optics or the lack of phase contrast in conventional images. Finally, it might also be possible to simultaneously record the diffraction pattern from x-rays scattered at larger angles than are accepted by the zone plate and use the reconstructed hologram as a phase reference at low resolution to solve the diffraction pattern at higher resolution, thereby obtaining a 3D image beyond the zone-plate resolution limit.

Because one needs to record holograms at each viewing angle, the specimen must be coherently illuminated. To obtain information from weak contrast objects in small-volume elements, many photons must be used. The specimen must be at cryogenic temperatures throughout the multiple-view experiment, unless one imagines placing a grating in front of the specimen to record multiple viewing directions in one flash exposure. The coherent flux requirements are extremely demanding for today' s synchrotron sources, and ultimately the resolution they can deliver in such an experiment is limited by the buildup of contaminants on a frozen hydrated specimen over many hours. Consequently, an FEL may be the only way to obtain the highest resolution data sets. Thermal effects may be alleviated by the fact that one wants to spread the FEL beam over an area of 10-30 micrometers or more, rather than focusing it down to a 0.1 micrometer spot.

VII. OUTLOOK

A. From molecular to modular and cellular biology

Structural biology is the foundation on which modern life sciences and medicine are built. The discovery of the double helix, the subsequent emergence of molecular genetics and molecular biology, together with the elucidation of protein and virus structures at atomic resolution are changing life sciences, as well as life itself. For the first time in the history of evolution, a genome is "reading itself" (and other genomes) in the same way as we read books: the Human Genome Project is nearing completion. New research areas, like bioinformatics, proteomics, genomics, and structural genomics are emerging from these developments. These "-omics" projects are modern, molecular equivalents of Linne' s innovation [66,67] called "biosystematics." Genomics and bioinformatics are one-dimensional sciences, proteomics is two-dimensional, structural genomics is three-dimensional. Biological function, however, is a four-dimensional property (x,y,z,t), and a functional understanding requires a synthesis of knowledge in four dimensions. Darwin' s theory of evolution is such a four-dimensional synthesis [68]. While his is a brilliant description of events on a grand scale, a comprehensive understanding of function on the supramolecular and subcellular level is still to come and may shed light on questions related to the emergence of life from a collection of complex chemicals. It is obviously not enough to simply mix such compounds. Function in biology is embedded into a network of interacting components. Biologists and others have thus begun to think about systems and networks, and we can anticipate research picking up on system analysis of labile, functional collections of interacting molecules or modules. Cellular functions (e.g., signal transduction, respiration, protein synthesis, etc.) are carried out by modules made up of many species of interacting molecules. Understanding how modules work and interact with each other is a key aim in understanding organization within a cell and, ultimately, in life. Structural information is only available on a handful of stable modules (macromolecular complexes) that could be crystallized (e.g., the cytochrome bc1 complex or the ribosome). Most modules are loose assemblies of interacting molecules, and studies on them require new approaches in which the LCLS may play a key role. We believe that studies on modules are likely to become a new norm of biological investigation, crucially aided by the other traditional disciplines and also by computational simulations. Certain modules may be localized and analyzed *in situ*.

Novel diffraction and data processing methods may allow phase retrieval and image reconstruction from images of whole biological cells, molecular clusters, and single biomolecules. The experimental pursuit in this direction is already in progress. Figure 8 shows an experimental diffraction pattern (wavelength = 13 Å) from an air-dried yeast cell recorded in the X1B undulator at the National Synchrotron Light Source to a resolution of about 180 Å. This experiment demonstrates the feasibility of recording diffraction patterns from nonrepetitive samples. The main limitation to achieving meaningful resolutions is radiation damage. Short and intense x-ray pulses from the LCLS may open up a new era for research here.

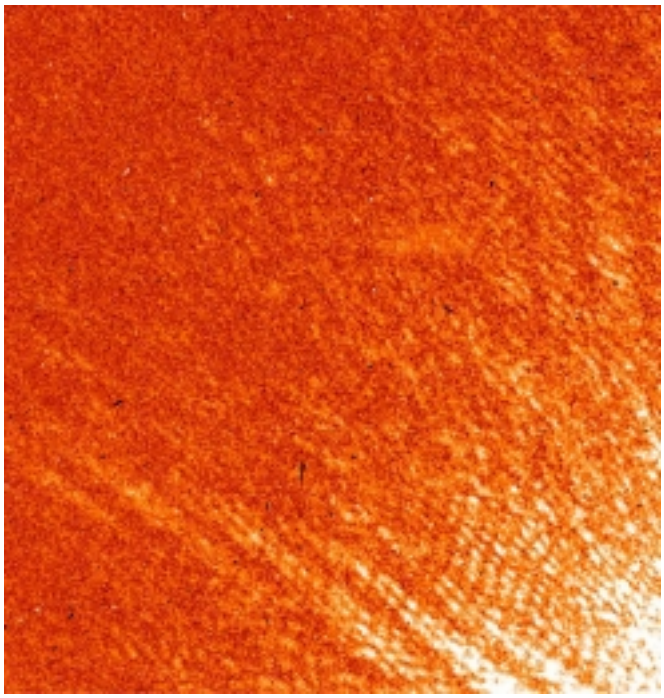

FIG. 8. The upper left quadrant of an experimental diffraction pattern from an air-dried yeast cell recorded on a 512 x 512 pixel CCD detector with 13 Å radiation and 10 min. exposure at the National Synchrotron Light Source, Brookhaven National Laboratory.

VIII. FEL REQUIREMENTS FOR THE PLANNED BIOLOGY EXPERIMENTS

A. Studies on large structures

Photon wavelength	1-15 Å
Bandwidth	0.2 %
Brightness	Important for focusing
Flux density per pulse	As high as possible (not more than about 10^8 photons/Å^2)
Transverse coherence	Yes; could be exploited in holographic imaging
Spontaneous radiation	Can be used (e.g., in tomographic imaging)
Higher harmonics	May be useful for shorter wavelengths (lower damage/elastic event)
Pulse length	230 fs and then shorter (while maintaining high dose/pulse)
Pump-probe ?	May be possible (delay pump-probe)
	Synchronization requirement: around 200 fs
Polarization (linear, circular)	Not relevant
Polarization (direction, hor/vert)	Not relevant
Focusing	Variable, down to 100 nm x 100 nm
Pulse-to-pulse fluctuations	Not a factor (normalization)
Pulse train	Not more than 120 Hz

B. Studies on small and large structures

Photon wavelength	1-15 Å
Bandwidth	0.2 %
Brightness	Important for focusing
Flux density per pulse	As high as possible (not more than about 10^8 photons/Å^2)
Transverse coherence	Could be exploited in holographic imaging
Spontaneous radiation	Could be used
Higher harmonics	May be useful for shorter wavelengths (lower damage/elastic event)
Pulse length	As short as possible (while maintaining high dose/pulse)
Pump-probe ?	Yes, a clear possibility (delay pump-probe)
	Synchronization requirement: around 200 fs
Polarization (linear, circular)	Not relevant
Polarization (direction, hor/vert)	Not relevant
Focusing	As much as possible (down to about 100 nm x 100 nm)
Pulse-to-pulse fluctuations	Not a factor (normalization)
Pulse train	Not more than 120 Hz (detector readout, sample clean-out)

IX. REFERENCES

[1] R. Henderson, Proc. R. Soc. **241**, 6-8 (1990).
[2] R. Henderson, Quart. Rev. Biophys. **28**, 171-193 (1995).
[3] R. Neutze, R. Wouts, D. van der Spoel, E. Weckert, and J. Hajdu, Nature **406**, 752-757 (2000).
[4] P. Teilhard de Chardin, (1955) *The Phenomenon of Man*.
[5] C. Nave, Radiat. Phys. Chem. **45**, 483-490 (1995)
[6] J.C. Solem, J. Opt. Soc. Am. **B3**, 1551-1565 (1986).
[7] J. Hajdu, in *Frontiers in Drug Research*, Alfred Benzon Symposium 28, B. Jensen, F.S. Jorgensen, H Kofod, editors, pp. 375-395. Munksgaard, Copenhagen (1990).
[8] S. Doniach, J. Synchr. Rad. **3**, 260-267 (1996).
[9] H. Winick, J. Elec. Spec. Rel. Phenom. **75**, 1-8 (1995).
[10] B.H. Wiik, Nucl. Instrum. Methods B **398**, 1-8 (1997).
[11] N.A. Dyson, *X-rays in Atomic and Nuclear Physics*, (Longman, 1973).
[12] M.O. Krause and J.H. Oliver, J. Phys. Chem. Ref. Data **8**, 329-338 (1979).
[13] S. Svensson, N. Martensson ,and U. Gelius, Phys. Rev. Lett. **58**, 2639-2641 (1987).
[14] W.J. Veigele, Atomic Data **5**, 51-111 (1973).
[15] J.H. Hubbell, W.J. Veigele, E.A. Briggs, R.T. Brown, D.T. Cromer, and R.J. Howerton, J. Phys. Chem. Ref. Data **4**, 471-494 (1975).
[16] B.L. Henke, E.M. Gullikson, and J.C. Davis, At. Data Nucl. Data Tables **54**, 181-342 (1993).
[17] T. Ditmire, Phys. Rev. **A57**, 4094-4097 (1998).
[18] H.R. Reiss, Laser Physics **7**, 543-550 (1997).
[19] D. van der Spoel *et al.*, in preparation.
[20] H.J.C. Berendsen, D. van der Spoel, and R. van Drunen, Comp. Phys. Comm. **91**, 43-56 (1995).

[21] W.F. van Gunsteren and H.J.C. Berendsen, *Gromos-87 Manual*. Biomos BV, Nijenborgh 4, 9747 (AG Groningen, The Netherlands, 1987).

[22] H.J.C. Berendsen, J.P.M. Postma, W.F. van Gunsteren, and J. Hermans, in *Intermolecular Forces*, B. Pullman, ed. (D. Reidel Publishing Company, Dordrecht, 1981) pp. 43-56.

[23] D. van der Spoel, P.J. van Maaren, and H.J.C. Berendsen, J. Chem. Phys. **108**, 10220-10230 (1998).

[24] L.H. Weaver and B.W. Matthews, J. Mol. Biol. **193**, 189 (1987).

[25] C. Rischel, A. Rousse, I. Uschmann, P. Albouy, J. Geindre, P. Audebert, J. Gauthier, E. Forster, J. Martin, and A. Antonetti, Nature **390**, 490-492 (1997).

[26] S.C. Harrison, A.J. Olson, C.E. Schutt, F.K. Winkler, and G. Bricogne, Nature **276**, 368-372 (1978).

[27] M. van Heel, Ultramicroscopy **21**, 111-124 (1987).

[28] M. van Heel, G. Harauz, E. V. Orlova, R. Schmidt, and M. Schatz, J. Str. Biol. **116**, 17-24 (1996).

[29] M. van Heel, E.V. Orlova, G. Harauz, H. Stark, P. Dube, F. Zemlin, and M. Schatz, Scanning Micros. **11**, 195-210 (1997).

[30] F. Mueller, I. Sommer, P. Baranov, R. Matadeen, M. Stoldt, J. Wohnert, M. Gorlach, M. van Heel, and R. Brimacombe, J. Mol. Biol. **298**, 35-59 (2000).

[31] B. Bottcher, S.A. Wynne, and R.A. Crowther, Nature **386**, 88-91 (1997).

[32] M.H.B. Stowell, A. Miyazawa, and N. Unwin, Curr. Opin. Struct. Biol. **8**, 595-60 (1998).

[33] D. Sayre, in *Proceedings of the NATO Course, Erice* (H. Schenk, ed.) pp.353-356 (1990).

[34] A. Szöke, Chem. Phys. Letts. **313**, 777-788 (1999).

[35] J.W. Miao, P. Charalambous, J. Kirz, and D. Sayre, *Nature* **400**, 342-344 (1999).

[36] A. Szöke, in *Short Wavelength Coherent Radiation: Generation and Application.* D.T. Attwood and J. Bokor, eds., American Institute of Physics Conference Proceedings No. 147 (New York, 1986).

[37] A. Szöke, Act. Cryst. **A49**, 853-866 (1993).

[38] M. Tegze and G. Faigel, Europhys. Lett. **16**, 41-46 (1991).

[39] M. Tegze and G. Faigel, Nature **380** 49-51 (1996).

[40] G. Faigel and M. Tegze, Rep. Progr. Phys. **62**, 355-393 (1999).

[41] J. Miao, D. Sayre, D. and H.N. Chapman, J. Opt. Soc. Am. **A15**, 1662-1669 (1998).

[42] D. Sayre, H.N. Chapman, and J. Miao, Acta Cryst. **A54**, 233-239 (1998).

[43] J. Miao, and D. Sayre, Acta Cryst. **A**, to be published (2000).

[44] D. Sayre, Acta Cryst. **5**, 843 (1952).

[45] I. Daubechies, Ten Lectures on Wavelets. Philadelphia, PA: SIAM (1992).

[46] G. Bricogne, *International Tables for Crystallography*, Vol. B. 1.3.3.1.1.7, U. Shmueli, ed. (Dordrecht: Kluwer Academic Publishers, 1992).

[47] G.J. Maalouf, J.C. Hoch, A.S. Stern, H. Szöke, and A. Szöke, Acta Cryst. **A49**, 866-871 (1993).

[48] J.R. Somoza, H. Szöke, D.M. Goodman, P. Beran, D. Truckses, S.H. Kim, and A. Szöke, Acta Cryst. **A51**, 691-708 (1995).

[49] A. Szöke, H. Szöke, and J.R. Somoza, Acta Cryst. **A53**, 291-313 (1997).

[50] P. Beran and A. Szöke, Acta Cryst. **A51**, 20-27 (1995).

[51] J.B.Murray, H. Szöke, A. Szöke, and W.G. Scott, Mol. Cell **5**, 279-287 (2000).

[52] C.V. Robinson, M. Gross, S.J. Eyles, J.J. Ewbank, M. Mayhew, F.U. Hartl, C.M. Dobson, and S.E. Radford, Nature **372**, 646-651 (1994).

[53] C.V. Robinson, E.W. Chung, B.B. Kragelund, J. Knudsen, R.T. Aplin, F.M. Poulsen, and C.M. Dobson, J. Amer. Chem. Soc. **118**, 8646-8653 (1996).

[54] D. Despeyroux, R. Phillpotts, and P. Watts, Rap. Commun. Mass Spect. **10**, 937-941 (1996).

[55] G. Siuzdak, B. Bothner, M. Yeager, C. Brugidou, C.M. Fauwuet, K. Hoey, and C.M. Chang, Chem. Biol. **3**, 45-48 (1996).

[56] M.A. Tito, K. Tars, K. Valegard, J. Hajdu, and C.V. Robinson, J. Am. Chem. Soc. **122**, 3550-3551 (2000).

[57] A.A. Rostom, P. Fucini, D.R. Benjamin, R., Juenemann, K.H. Nierhaus, F.U. Hartl, C.M. Dobson, and C.V. Robinson, Proc. Natl. Acad. Sci. USA **97**, 5185-5190 (2000).

[58] P. Kebarle and L. Tang, Anal. Chem. **65**, A 972-986 (1993).

[59] A. Orfao and A. Ruizarguelles, Clin. Biochem. **29**, 5-9 (1996).

[60] J.R. Fienup, Appl. Opt. **21**, 2758-2769 (1982).

[61] T.W. Lin, C. Porta, G. Lomonossoff, and J.E. Johnson, Fold. & Des. **1**, 179-187 (1996).

[62] K. Valegå rd., L. Liljas, K. Fridborg, and T. Unge, Nature **345**, 36-41 (1990).

[63] A.J. Fisher and J.E. Johnson, Nature **361**, 176-179 (1993).

[64] B. Bottcher and R.A. Crowther, Structure **4**, 387-394 (1996).

[65] P. Gouet, J.M. Diprose, J.M. Grimes, R. Malby, J.N. Burroughs, S. Zientara, D.I. Stuart, and P.P.C. Mertens, Cell **97**, 481-490 (1999).

[66] C. Linne, *Philosophia Botanica*, Uppsala (1751).

[67] C. Linne, *Species Plantarum*, Uppsala (1753).

[68] C. Darwin, *On the origin of the species by means of natural selection, or the preservation of favoured races in the struggle for life* (John Murray, London, 1859).

Femtochemistry

Dan Imre, *Brookhaven National Laboratory, Upton, NY, USA*
Ahmed Zewail, *California Institute of Technology, Pasadena, CA, USA*
Wilson-Squire Group, *University of California, San Diego, San Diego, CA, USA*
John Arthur, *Stanford Synchrotron Radiation Laboratory, Stanford, CA, USA*
Michael Wulff, *European Synchrotron Radiation Laboratory, Grenoble, France*
Philip Anfinrud, *National Institutes of Health, Bethesda, MD, USA*
Richard Neutze, *Uppsala University, Uppsala, Sweden*
Jerry Hastings, *Brookhaven National Laboratory, Upton, NY, USA*
Chi-Chang Kao, *Brookhaven National Laboratory, Upton, NY, USA*
Mark Renner, *Brookhaven National Laboratory, Upton, NY, USA*

I. SUMMARY

A chemist's most powerful tool is his or her ability to describe matter in terms of bond lengths and angles. From a chemist's perspective, an intuitive predictive picture of a system, or a process, describes the molecular structure and its evolution in time. Chemical reactions and physical transformations involve the breaking and rearranging of intra- or intermolecular bonds for which the time scale of fundamental steps is on the order of femtoseconds or picoseconds and distance is measured in angstroms. Since every chemical or physical transformation involves structural changes on an atomic scale, the direct observation of these processes would necessarily require an instrument with the power to resolve molecular bond lengths spatially and molecular vibrations temporally. Only an extraordinary apparatus, such as the Linac Coherent Light Source (LCLS), has sufficient spatial and temporal resolution to follow molecular motion in real time.

We present here only a sampling of studies where significant breakthroughs could be anticipated, though there are many more that could become reality once the proposed light-source is fully operational

We begin with the most fundamental of chemical reactions: photodissociation of isolated gas-phase molecules. We then proceed through photochemically induced bond breakage in solution and the subsequent recombination within the solvent cage. The LCLS will make it possible to trace atomic motions during these reactions in real time.

Photosynthetic processes present a higher level of complexity. While, traditionally, the studies in the field of photosynthesis have been divided into structure determination and time-resolved dynamics, here we propose to use the LCLS to observe the structural transformations in real time.

When a crystalline sample is excited with an intense short laser pulse, extreme states of matter can be produced. Melting on picosecond and femtosecond time scales have been reported. We propose to use the LCLS to probe the dynamics of these ultrafast transformations by characterizing the time-evolving structures.

Nucleation experiments in extremely metastable nanodroplets will make it possible to follow, in real time, the formation of a critical nucleus and its subsequent growth. The resulting data could

be compared directly with molecular dynamics simulations of nucleation processes for the first time.

Nanoparticles, or quantum dots, are extremely attractive to science as well as industry. The LCLS will enable us to observe the internal and surface motions within a single nanoparticle.

II. BACKGROUND AND MOTIVATION

A. Temporal and spatial resolution in molecular dynamics

Because every chemical or physical transformation involves structural changes on an atomic scale, the direct observation of these processes would necessarily require an instrument with the power to resolve molecular bond lengths spatially and molecular vibrations temporally. Chemical reactions take place when existing bonds break and new ones are formed, while physical transformations, such as phase transitions, are a result of atomic rearrangement. The time scale of the fundamental steps, which bring about transformations, typically ranges from femtoseconds to picoseconds and is determined by the time required for atoms to move. For example, when a water molecule absorbs a UV photon, ~8 femtoseconds elapse before one of the hydrogen atoms can move far enough for the system to be described as H+OH rather than H_2O. During that brief period of time, the atomic separation between the H atom and the OH molecule has increased by a mere angstrom. The H atom, which is the lightest atom, sets the upper limit for the time resolution necessary to observe motion on the atomic scale.

Ultrashort pulsed lasers, with pulse widths on the order of a few femtoseconds, have been used for the past two decades to study a wide array of atomic, molecular and macroscopic transformations. Ultrafast lasers have made it possible to measure the time it takes for processes to occur [1-5]. However, the fact that they operate in wavelengths that are more than three orders of magnitude larger than a typical bond length limits their ability to provide information with relevant spatial resolution. In a typical femtosecond pump-probe experiment, the pump pulse induces an electronic transition. A variably delayed probe pulse is used to map out the time evolution of a spectrum, which is a measure of the transition probability between the time-evolving prepared state and yet another electronic state. The nuclear and/or electronic dynamics of the system is then inferred from these time-resolved spectra.

As chemists we find that a description of matter in terms of bond lengths and angles is extremely powerful. This picture of nature has served us well. Most major breakthroughs in the area of chemistry or biochemistry can be traced to the solution of a molecular structure. Therefore, from a chemist's perspective, a truly detailed understanding of a system or a process should include a description of molecular structure and its evolution in time. At a time when extremely short laser pulses are making it possible to observe dynamical events on a molecular vibration time scale, a glaring lack of any spatial resolution limits the entire field. We can tell how fast the structure is changing, but cannot describe how.

In a 1991 editorial in the magazine *Nature*, J. H. Thomas discussed a revolutionary proposal by Williamson and Zewail, to use time-resolved diffraction to trace the motion of individual atoms as they are rearranged during a reaction. The Williamson-Zewail proposal addresses the widely accepted premise that only when one can trace the path of atoms in the course of a chemical transformation with great detail is the true mechanism of the change properly characterized. The ability to describe the positions and movements of atoms during a fraction of a molecular vibration goes to the core of our understanding of the transition state. The revolutionary concept in the Williamson-Zewail proposal was their suggestion that time-resolved diffraction could be

used in conjunction with ultrafast lasers to map out the trajectories of individual atoms *directly* during chemical transformation.

A great deal of progress has been made since that editorial was published. Tabletop- and accelerator-based subpicosecond x-ray sources have been developed [6-8] to enable a new class of experiments in physics, chemistry, and biology [7,9-12]. In other experiments, short pulses of high-energy electrons have been used to obtain time-resolved diffraction spectra [5,13]. These efforts produced the first observations of the earliest few picoseconds of the melting process of a crystal [10,14] and the time-resolved electron diffraction spectra of a photodissociating polyatomic gas phase molecule [15].

Tabletop short-pulse x-ray and electron sources, when utilized in pump-probe experiments with visible long-wavelength lasers, provide an unprecedented view of chemical and physical transformation processes in nature, but they are of limited use due to their relatively low brilliance and temporal resolution. LCLS is ideally suited to the purposes of this emerging scientific field. Its brilliance is many, many orders of magnitude higher than that achieved by tabletop x-ray sources and the temporal resolution it offers, of order 200 femtoseconds, will make it possible to resolve events on subvibrational periods for many molecular systems.

B. LCLS techniques

The unique properties of the LCLS can be applied, through a number of spectroscopic and diffraction techniques, to a wide range of fundamental problems. A sharp pulse from a short optical pulse laser, which is then followed by an x-ray probe pulse from the LCLS, comprises the typical experiment. The delay between the pump and probe pulses defines the time evolution.

The most obvious application of the LCLS for the study of chemical and physical transformations would be in a diffraction mode. Here, a pump pulse from a femtosecond laser initiates a photochemical reaction and the x-ray light from the LCLS is used to obtain time-delayed diffraction spectra to chart changes of a molecular structure.

Time resolved diffraction is only one of many possible techniques that can be used to interrogate rapidly evolving systems. X-ray absorption spectroscopy (XAS) and its variant, extended x-ray absorption fine structure (EXAFS), are extremely powerful techniques that can also be used to yield direct molecular structural information. EXAFS can be used to probe the radial structural information centered on a specific metal ion (i.e., how many of what type of atoms are at what distance from the metal). Time-resolved XAS and EXAFS spectroscopy can thus be used to hone in on the dynamics of a specific metal ligand bond.

Mie scattering spectroscopy is used to study changes in the size and index of refraction of spherical and non-spherical particles, whose size is within a factor of 10 from the light's wavelength. Minute changes in particle size can be detected in the form of sharp Mie resonances. By using the x-ray pulse from the LCLS to generate Mie spectra in combination with a short-pulse, visible-UV laser, it will be possible to investigate the dynamics of nanometer-size particles.

In most cases, only a fraction of the molecules become excited by the first laser pulse and therefore, the probe spectra tend to be composites of unexcited- (the unwanted portion) and excited-state molecules. It is possible to develop stimulated Raman-like techniques to produce spectrally shifted outgoing x-rays at frequencies that are dependent on the pump laser frequency, and thus rid the probe spectra of the unwanted portions.

Thus, the temporal and spatial resolution offered by the LCLS makes it an ideal light source for the study of chemical and physical transformations on the molecular scale. The present document provides an exploration of a number of applications of the LCLS to fundamental problems in chemistry and chemical physics. The section below outlines a few of the scientific issues, their importance and the role that the LCLS could play in addressing them.

III. SCIENTIFIC OBJECTIVE

A. Unimolecular photochemistry

1. Photochemistry in the gas phase

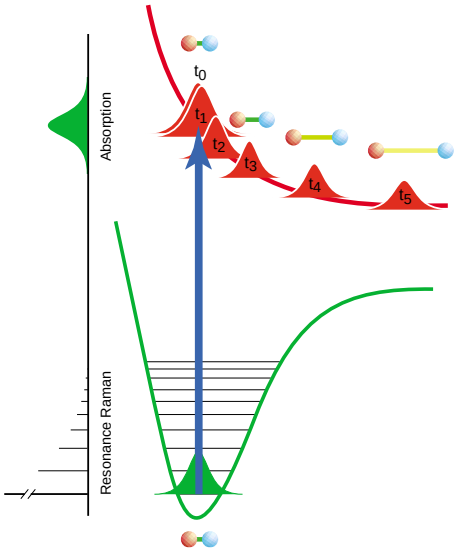

FIG. 1. Idealized diatomic photodissociation. The red wave packet is prepared on the repulsive excited state at t=0. The time evolving wave packet remains fairly localized as it moves to longer bond lengths. The absorption spectrum is featureless, and the resonance Raman spectra show a long progression tracing the reaction.

The ideal system through which to explore the evolution of molecular geometry during chemical transformations in real time should maintain a relatively well defined nuclear geometry throughout the reaction (i.e., the coordinate space wave packet describing the reaction should remain localized). The nuclear wave function of thermally excited molecular systems near or above their dissociation limit tends to be extremely diffuse and even the concept of a “bond length” becomes ill defined. In contrast, the wave function of a photodissociating molecule as it moves on the repulsive potential often remains localized throughout the reaction. It is therefore meaningful to assign a bond length as a function of time, and consequently it may also be practical to design an to measure it directly.

The photodissociation of the diatomic AB molecule, illustrated in Fig. 1, is the simplest of chemical reactions. The ground electronic state is bound and the electronically excited state is repulsive. A short-pulse laser prepares a coherent localized wave packet in the Franck-Condon

(FC) region. The shape of this wave packet at t=0 is virtually identical to the vibrational wave function on the ground electronic surface. The wave packet develops momentum and begins to move. Within a few tens of a femtosecond it has accelerated and moved to where it is better described as two separate atoms. The reaction is thus complete. The LCLS offers the proper

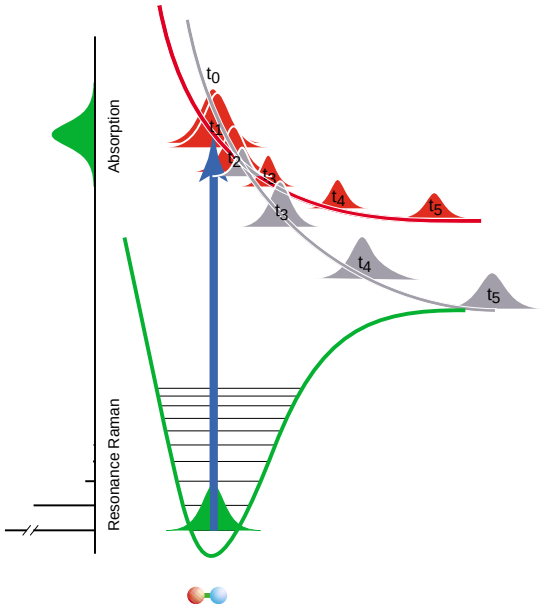

FIG. 2. Schematic representation of a photodissociation process that includes surface hopping. The initial wave packet is prepared on the optically active red excited state, which is crossed by the dark gray state. As the wave packet moves to near the crossing point between the two excited states a fraction of its amplitude crosses to the gray state, changing its electronic character in the process. The gray wave packet moves faster because of the differences in energy between the two surfaces.

temporal and spatial resolutions for a detailed characterization of such an idealized process. It should be possible, in principle, to trace the transformation of the AB molecule into the two separate atoms A+B, by using time-resolved diffraction. In reality, however, there are no accessible molecular systems of such simplicity.

Figure 2 shows a more realistic diatomic system, in which the added complexity is representative of virtually every molecular system. It has multiple excited states and, as a result, it also exhibits complex dynamic behavior that includes surface hopping. Surface hopping, which is an integral part of nuclear dynamics, is a process by which a fraction of the wave packet hops from one surface to the next and becomes electronically transformed as a result. This process may occur even when the initial laser pulse prepares a localized wave packet in a relatively pure electronic state, because the nuclear motion that follows inevitably induces electronic transitions.

The surface hopping process described above takes place during virtually every photochemical transformation, but since curve crossings are inherently quantum mechanical processes, and because their rates depend exponentially on the details of the crossing geometry, they are notoriously difficult to simulate. It would be highly desirable to provide these simulations with experimental observations that can be used to guide and test them. Frequency domain experiments

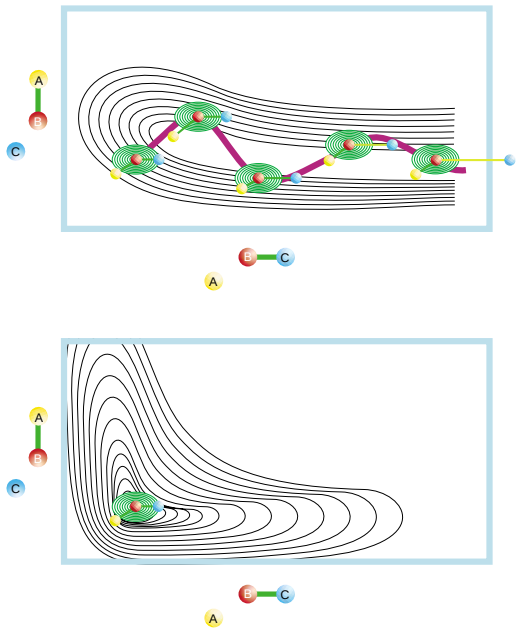

FIG. 3. Schematic representation of a triatomic ABC photodissociating molecule. The lower panel is the ground state and the upper one shows the dissociative excited state. Also shown in purple is the trajectory of a wave packet on the excited state during the photodissociation process.

such as resonant Raman spectroscopy have long been used to study nuclear dynamics during photodissociation. The dynamics is “followed” here by measuring the transition probability between the photodissociating wave packet in the excited state and the ground electronic state vibrational wave functions. The Raman line intensities are used to infer nuclear motion. It is, however, generally accepted that resonant Raman spectroscopy only explores the FC and its immediate vicinity.

The LCLS is perhaps the only experimental apparatus that might enable us to observe these very fundamental chemical processes in detail, as depicted in Fig. 2. A direct measurement of the atomic separation as a function of time has the potential for revealing the surface hopping process. The fraction of the wave packet on the lower surface is moving faster than the one that stays on its original curve. One would expect to observe two distinct populations to form over time. Since the LCLS operates with the appropriate spatial and temporal resolution, it may allow the actual differentiation of the two populations to be observed for the first time.

In polyatomic molecules, the reaction proceeds along many coordinates and the motion that leads to reactions includes “spectator” and reactive modes. Figure 3 shows a schematic representation of a single excited electronic state of a generic ABC molecule in two of the three vibrational degrees of freedom, the A-B and B-C bond lengths. Also shown are snapshots of an evolving wave packet. The motion to break the B-C bond also induces the A-B bond to oscillate about an increasingly shorter bond length. These two motions couple to produce a vibrationally excited A-B product.

In ABA systems, the force, and hence the motion, on the excited state is always along the symmetric stretch and dissociation takes place by wave packet spreading. CH_2I_2, one of the members of this class, has recently been the subject of numerous femtosecond experiments. It was also the subject of a time resolved, picosecond electron-scattering experiment. The data suggest that two processes occur; the first is on the order of 200– 300 fs, while the second takes a

few picoseconds to complete. Despite an intense effort the exact nature of the two processes is still unclear. The LCLS may be able to provide the needed information to understand this very fundamental reaction.

2. Photochemistry in the condensed phases

The section above presented the most fundamental open questions in chemistry: unimolecular reactions of isolated molecules in the gas phase. Most of chemistry, however, takes place in the condensed phase, where the interactions between the solvent

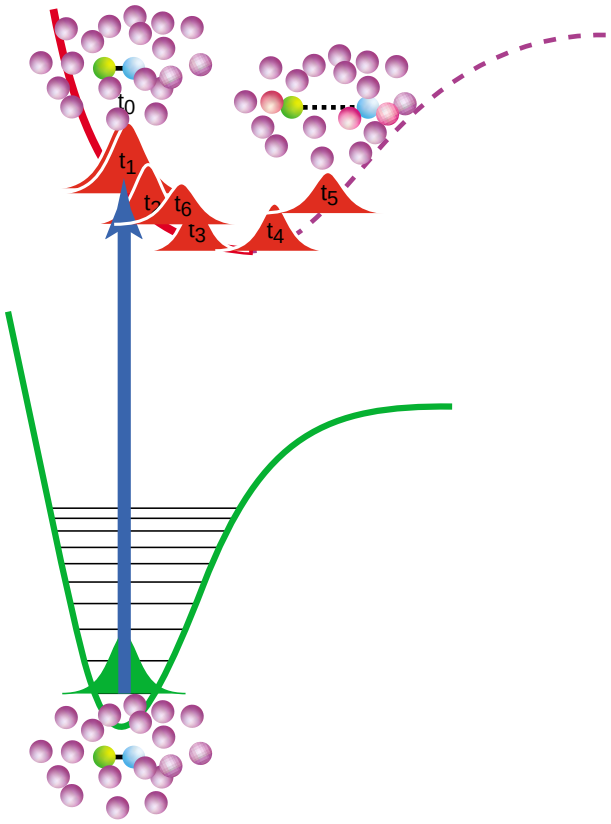

FIG. 4 A schematic representation of a photodissociation experiment in the condensed phase. The solvent molecules are represented by purple balls and the diatomic are blue and yellow. The dashed purple line represents the molecule solvent interaction.

and the reacting molecule often determine the final outcome of a reaction. On a most rudimentary level, the solvent molecules act as barriers by preventing the separation of molecular fragments. As the wave packet accelerates downhill energetically, the atoms are moving away from each other and toward the solvent molecules. Unless one of the atoms can find a gap to escape through, it will hit a solvent molecule, lose some of its kinetic energy, bounce back, and recombine geminatly (rejoin its geminate twin). This phenomenon is called the cage effect. Because all of the dynamics prior to recombination is above the dissociation, it cannot be traced by using spectroscopic techniques in the optical range. In contrast, an experiment that is sensitive

to nuclear separations such as x-ray scattering, would be ideally suited to the problem. Figure 4 is a schematic illustration of the dynamical processes of a photodissociation process in the condensed phase.

The utility of x-ray diffraction in the study of cage dynamics was demonstrated most recently by Neutze *et al*. [16]. They have applied picosecond elastic x-ray scattering to the study of iodine photodissociation in dichloromethane solvent. Following photoexcitation to the repulsive wall of the B surface, the two atoms of diatomic iodine rapidly move apart. The kinetic energy of the exploding molecule is absorbed by the solvent and within a few picoseconds, the majority of the fragments recombine. As a result of reorientation during the collision with the solvent, recombination can take place on any of the surfaces. These preliminary experiments clearly demonstrate the feasibility of time-resolved diffuse x-ray scattering, even when applied to a system where the molecule of interest is at millimolar concentrations in a solvent.

The LCLS will make it possible to resolve the individual steps and investigate the early time dynamics when the initial solvent/fragment collision takes place, as well as the fragment/fragment recombination.

B. Biological systems

1. Dynamics of photosynthetic systems

The development of short-pulsed lasers 25 years ago made it possible to observe molecular dynamic events with picosecond time resolution and uncovered completely unexpected early steps in photosynthesis. We are on the verge of being able to take another important step as we develop new tools, which will complement these fast lasers and will enable us to observe the structural transformations that accompany and/or drive the picosecond/femtosecond dynamics of photosynthesis.

The dynamics of excited-state metalloporphyrins, their lifetimes and relaxation pathways are central to an understanding of the energy conversion processes in photosynthesis (electron transfer, charge separation and storage). It is now accepted (on the basis of theoretical calculations and experimental observations using static and time-resolved magnetic, electronic and vibrational spectroscopy), that nuclear dynamics play a key role in the determination of electronic dynamics. In many respects, porphyrin dynamics is a complex example of what has been described above as curve-crossing dynamics.

The tracing of multiple atomic motions in a large molecule such as a porphyrin (or worse yet, including its host protein) in the excited state is prohibitively complex. However, x-ray absorption experiments at the metal K-edge make it possible to focus on the metal atom and its immediate environment. These spectra can be used to monitor the metal coordination number, geometry, nearest neighbor atoms, oxidation state and bond distances in solution, while L-edge XAS experiments for 3d transition metals that are sensitive to the metal electronic structure, provide information about the metal 3d-orbital splitting, oxidation and spin state.

Time-resolved XAS studies of metalloproteins and other inorganic compounds in their excited states have been reported recently [17,18]. These experiments were used to study the photodissociation of carbon monoxide in myoglobin, the base on and off rates in cobalamine, structural changes associated with the excited states of inorganic compounds, and photoinduced spin-state changes in iron(II) complexes. However, the time resolution of these experiments is mostly limited to microseconds.

The frequency spectrum of the LCLS, together with its temporal resolution, should make it possible to observe the motion of metal ligands and any electronic transformations on a time scale that is faster than the vibrational period of the metal-ligand motion. These experiments could be carried out in solution with the porphyrin in its native environment.

C. From lattice vibrations to phase transitions and extreme phases

Most of the fundamental steps in atomic-scale dynamics, including transport of acoustic vibrations and phase transformations in condensed matter, occur on time scales that are comparable with lattice vibrations (femtosecond to picoseconds), and on length scales comparable with molecular distances. Yet, measurements on ultrafast time scales have been largely limited to visible or near-visible wavelengths, which provide information about valence electrons and Raman-active vibrational modes. A number of recent experiments used ultrashort x-ray pulses from a variety of to observe directly harmonic and anharmonic dynamics of coherent acoustic phonons and ultrafast melting in crystalline solids. However, the low flux of these sources (10^8 photons/pulse sr) limits their applicability to ordered systems. Figure 5 is a schematic illustration of a typical pump-probe experiment designed to study phase transformations in ordered systems.

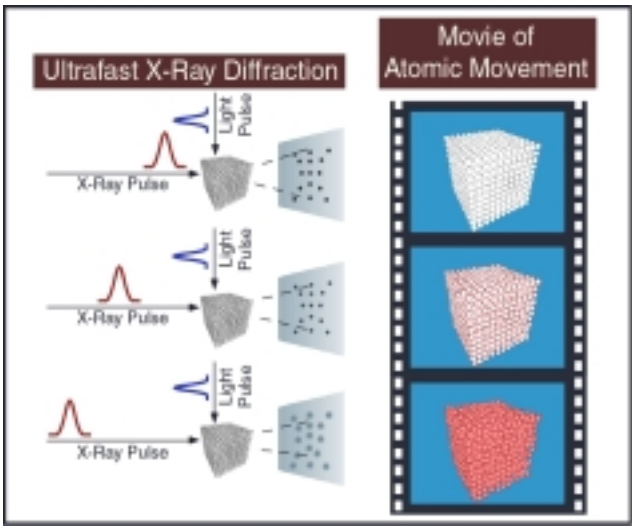

FIG. 5 A schematic representation of a typical ultrafast x-ray scattering experiment designed to study the melting of ordered systems. In the first frame the optical laser pulse and the x-ray pulse arrive at the sample at the same time. The diffraction pattern is sharp since no electronic-to-vibrational energy transfer has occurred. The second frame is an intermediate stage of melting. In the final frame the x-ray pulse is delayed to allow for the electronic to vibrational energy transfer process to evolve, eroding the crystal structure and thus diffusing the scattering pattern.

These pioneering experiments help to highlight the benefits of time-resolved x-ray studies. The very high peak brilliance and superior time resolution of the LCLS could make possible a large number of experiments in condensed matter that are inaccessible at present. Below is a truncated list of possible applications of the LCLS to condensed-phase physics:

1) By correlating time-resolved structure determination (x-ray diffraction) with ultrafast optical measurements during the early stages of laser-induced phase transitions, the interplay between electronic and atomic rearrangements could be determined (e.g., during metal-insulator or conductor-superconductor transitions). This class of experiments would be particularly revealing in systems where the electrons are strongly correlated or where phase transitions could be coherently driven by optical excitation along soft vibrational modes.

2) Ultrafast structural probes in (x-ray diffraction and/or EXAFS) could elucidate the physical properties of transiently generated states of matter that were obtained by irradiating materials with intense, ultrashort laser pulses. For instance, important information would result if the maximum degree of superheating of a solid phase and its connection to structural stability could be determined. Equally important would be the measurements of atomic rearrangement in solid phases at high pressures, for example during compression by a shock wave. Finally, previously unexplored regions of the phase diagrams of materials could be addressed, revealing, for instance, the geologically and technologically relevant dynamics of the melting of carbon [19] or of diamond formation [20].

3) Ultrafast, small-angle x-ray scattering experiments would permit investigations of mesoscopic rearrangements on the nanometer scale, for instance by measuring nucleation rates of new phases [21] (solid to liquid and liquid to gas) far away from thermodynamic equilibrium. The mesoscopic dynamics that lead to nanometer-scale structuring of carbon-based materials (e.g., nanotube formation) could also be investigated, with great benefit to studies in nanotechnology.

4) Dynamic probing of high k-vector vibrational excitations would be made possible by extending inelastic x-ray scattering experiments to the ultrafast time scale. Ultrafast probes of localized vibrational excitations in solids and liquids would reveal, among other things, the important interplay between molecules and surfaces, between solvents and solute, and its role in the stabilization of chemical reactions via vibrational energy transfer.

D. Dynamical processes in nanoparticles

1. Vibrational modes and capillary waves

Nanoparticles, also known as quantum dots or nanocrystals, possess unique electronic and optical properties that result from quantum size confinement of charge carriers and an extremely large surface area, relative to volume. From a fundamental scientific perspective, nanoparticles offer an opportunity to study a range of phenomena that are otherwise inaccessible. They also hold great promise for applications in areas such as microelectronics, electro-optics, photocatalysis, and photoelectrochemistry.

The large percentage of surface atoms can introduce a high density of surface states. These surface states can fall within the band gap, trap charge carriers (electrons and holes), and affect the charge-carrier behavior and other properties of nanoparticles. In the last few years, significant progress has been made in the study of the dynamic properties of charge carriers in semiconductor and metal nanoparticles, mainly through the use of femtosecond laser techniques. In conjunction with conventional spectroscopy and powerful microscopy techniques, preliminary understanding of the dependence of the charge-carrier lifetime on particle size, surface area and shape started to emerge. Because these studies use optical pump-probe techniques, they can only probe the electronic dynamics.

While a great deal of attention has been given to electronic transformations, not a single study has probed the nuclear dynamics, which occur in the excited electronic states and continue after the system returns to the ground electronic state. Depending on the electronic temperature, different lattice internal and surface vibrational modes will be stimulated. These should result in particle deformations at the particles' natural frequencies. Using x-ray scattering, it should be possible to observe these deformations in real time and characterize the vibrational states as a function of particle size and composition.

Recently there has been considerable interest in the structure of vapor-liquid interfaces at short length scales. In the Gibbs model, these interfaces are described as regions of continuous variation of density, and recent density functional calculations, based on that model, have led to the prediction of a reduction in surface energy at short (angstrom to nanometer) length scales. A similar prediction was obtained more recently, with the newer capillary wave model. The capillary wave model, however, is qualitatively distinct from the non-uniform spherical drop-model of Gibbs. In the former, the interface assumes a locally step-like density profile, whose overall width results from the propagation of thermally excited capillary waves, while the latter treats the gas-liquid interface as a slow change in density. The proposed femtosecond pump-probe x-ray scattering experiments have the potential to resolve nonuniform density profiles on the angstrom scale, as well as to "freeze" (in time) the surface morphological effects caused by the presence of capillary waves. Figure 6 provides a schematic of a pump-probe experiment designed to observe internal and surface vibrational modes.

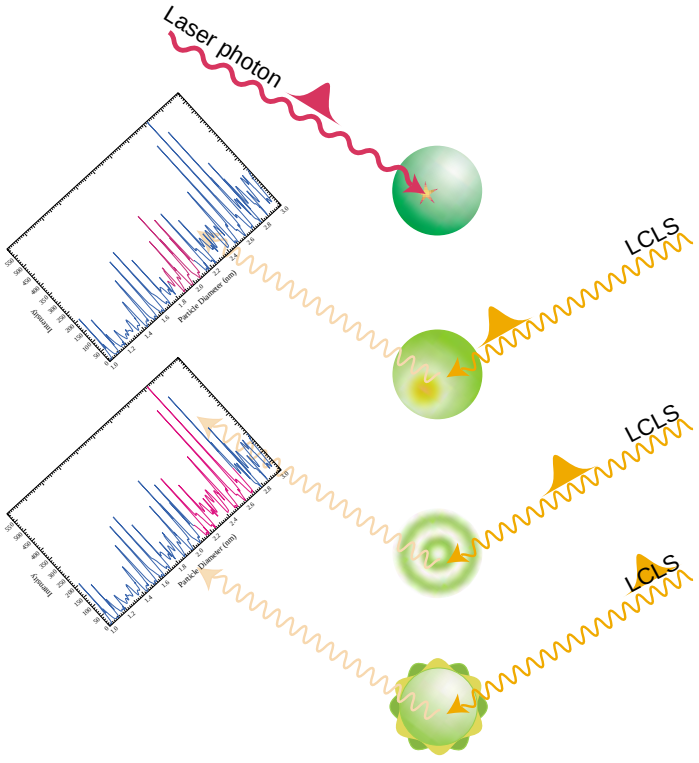

FIG. 6. A schematic of an experiment designed to probe nanoparticle vibrational and surface modes.

2. Melting on the nanoscale level

Nanoparticles offer a unique opportunity to investigate the dynamics of melting and crystallization. One could use an optical femtosecond laser to deposit sufficient energy, so as to induce complete particle melting. Time-resolved melting studies of films have been reported and discussed above. Melting of nanoparticles may present a very different dynamical system. Here, the overall particle size is significantly smaller than that of the exciting light wavelength, and no substrate is present to provide for heat exchange. It should be possible to trace the solid-to-liquid transformation process in real time, by using either x-ray Mie scattering, or x– ray diffraction, following a sharp excitation in time. It would be interesting to explore the

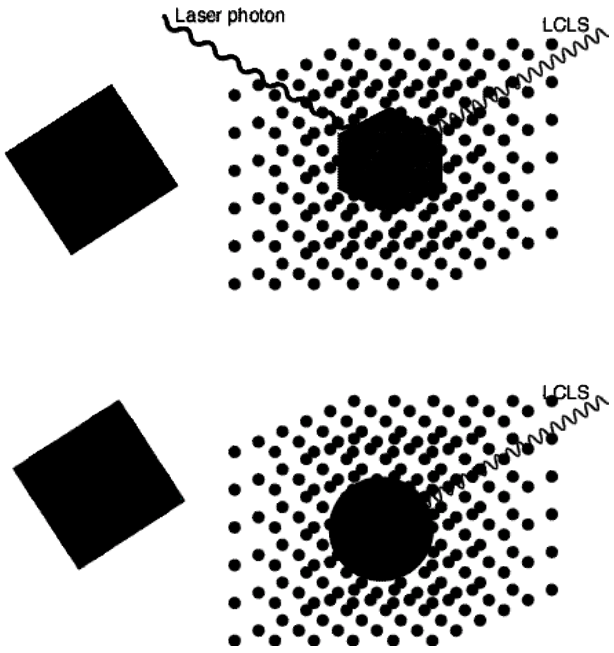

FIG. 7. A schematic of a laser-induced nanoparticle melting in Ne crystal experiment.

connection between the size-dependent dynamical behavior with the observed size-dependent melting point. As an illustration of the magnitude of this latter effect, note that the melting point of a 0.5-nm-sized Na particle is 30% lower than that of a cubic micrometer or a cubic inch of Na, which have equivalent melting points.

The dynamics of melting of a single nanoparticle could be investigated using particles trapped in a rare gas crystal. Figure 7 is a schematic illustration of such an experiment.

3. Nucleation dynamics

The transformation from a disordered liquid phase to a crystalline one is triggered by a nucleation event (i.e., the formation of an initial germ structure followed by crystal growth about it). The entire process is kinetically controlled, highly nonlinear and cooperative. Crystallization can only take place once a critical germ, large enough to overcome the nucleation barrier, forms. But, the rate of critical germ formation is exceedingly slow unless the system is driven past the solid-liquid equilibrium point. As the system is driven further into the meta-stable region, the height of the barrier to nucleation is reduced and the size of the required germ decreases, driving

up the rate of critical germ formation. Ultimately, the rate of nucleation increases to the point where the phase transition can occur within the observation period.

Classical nucleation theory, which has been successful at predicting nucleation rates of many systems, takes a macroscopic, thermodynamic view of the process and makes no realistic attempt to describe its dynamic details. Recently, however, it has become possible to perform molecular dynamics simulations by using trajectories driven by classical mechanics of systems sufficiently large to make these simulations relevant to nucleation. This approach provides an intuitive view of the dynamical process. It treats the individual molecules and their interactions in "real time," and its output is a movie of the position and momenta of each molecule as a function of time. One can literally watch these movies, trace the molecular motions, and even identify the formation of a critical nucleus just prior to crystallization. Because of the number of molecules that are required to obtain a realistic representation of a nucleation event, these computations are very intensive, and the observation times are limited to a few picoseconds.

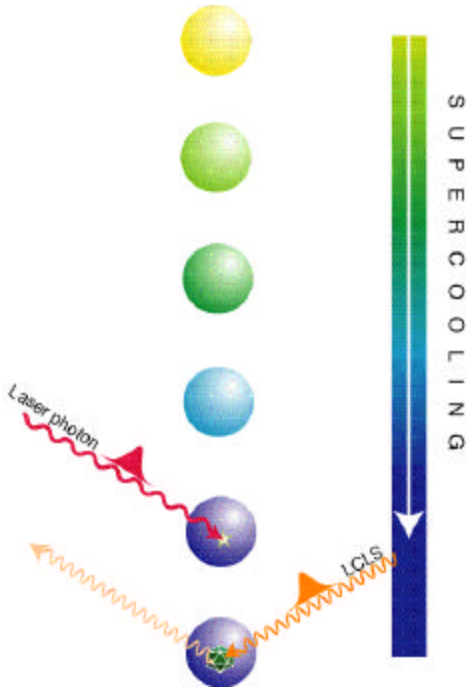

FIG. 8 A schematic representation of a time-resolved laser-induced nucleation experiment. Nanoparticles are supercooled to just below the nucleation threshold. An optical laser pulse generates a catalyst that starts the nucleation. An x-ray photon is used to probe the growth dynamics.

There is an obvious match between the temporal and spatial scales offered by the LCLS, the nucleation dynamics, and the molecular dynamics simulations that if explored could provide a great deal of insight into the processes that control nucleation. Figure 8 is a schematic illustration of an experiment designed to probe nucleation dynamics in small particles.

IV. EXPERIMENTAL DETAILS

A. Time-resolved molecular structures during photochemical reactions

1. Photochemistry in the gas phase

The pioneering experiments by Zewail *et al*., in which ultrafast electron diffraction was used to investigate the photodissociation of $C_2F_4I_2$ in a molecular beam, serve as a guide for the design of the gas phase photochemistry proposed here. These experiments have shown that time-resolved diffraction of non-crystalline samples is a feasible method and that the spectra can be inverted to obtain structural information of very short lived molecular intermediates. In this case the parent molecule photodissociates in two phases to yield a hot C_2F_4I and an iodine atom in the initial phase, which is then followed by a much slower process, during which the hot C_2F_4I fragments to form C_2F_4 and a second iodine atom. The half-life of the second phase was measured to be on the order of 20 ps.

Table 1 shows a comparison between the parameters of the gas-phase experiments of Zewail *et al*. and those attainable by the LCLS. The time resolution of the ultrafast electron detection (UED) experiments is limited to ~10ps. The inverse relationship between the number of electrons and the ultimate resolution makes it extremely difficult to improve on this system. At present, UED cannot be used to trace molecular motions, which are generally on a sub-picosecond time scale. The LCLS is expected to provide similar signal strength but with temporal resolution fifty times better than the UED.

Table 1. Comparison between Ultrafast Electron Diffraction (UED) and the LCLS

	Δt[1]	flux	Cross section[2]	Rate (Hz)	Signal[3]
UED	10 ps	7000	10^7	1000	7×10^{13}
LCLS	200 fs	2×10^{12}	1	100	2×10^{14}

[1] time resolution; [2] relative cross section; [3] relative signals

We propose to perform the first set of experiments on a diatomic molecule. As mentioned above, the nuclear motion of diatomic molecules might be rather trivial, but the added complications due to electronic-nuclear coupling make the problem interesting. Every one of the diatomic halogens is a good candidate for a study of curve-crossing dynamics described in the introduction. The electronic structure of I_2 is presented in Fig. 9. Other halogens present similar scenarios.

The two-step photodissociation of $C_2F_4I_2$ would clearly be an interesting case to explore given the background information that is available. The superior temporal resolution of the LCLS will make it possible to time resolve the first iodine atom dissociation and observe the intramolecular energy transfer processes that bring about the dissociation of the second iodine atom.

2. Photochemistry in the condensed phase

The utility of the LCLS is not limited to isolated systems in the gas phase. One of the advantages of the LCLS over UED is the fact that it can be applied to the investigation of solution-phase dynamics. Most of chemistry takes place in the condensed phase, where the solvent influences

the electronic structure, as evident from shifts in absorption spectra and the nuclear dynamics by providing a cage to trap the products.

The design of the photochemistry in solution experiments seeks to build on the successes of Neutze *et al*. in developing the methodology to follow the dynamics on a picosecond time scale through x-ray scattering. They used beamline (ID09) of the European Synchrotron Radiation Facility and a gas-filled x-ray detector, coupled to a lock-in detection system and were able to observe a diffuse scattering signal following photodissociation, from geminately recombining iodine atoms in dichloromethane. The electronic structure and a schematic of the dynamics are shown in Fig. 9. When I2 is excited to the B state above its dissociation limit, it falls apart in less than a picosecond. Due to the presence of the solvent cage, the kinetic energy of the exploding molecule is absorbed, and within a few picoseconds the majority of the molecules recombine geminately. The relaxation pathway down to the ground state passes through the excited A-state, which has a solvent-dependent lifetime (equal to 500 ps in dichloromethane). Due to the greater interatomic separation of excited state iodine relative to its atomic separation in the ground state, the diffuse x-ray scattering pattern will be slightly changed. The experimental results are shown in Fig. 10. The solid line shows the theoretical curve obtained by convolution of the 500 ps decay of the A-state in dichloromethane with the 80 ps FWHM x-ray probe.

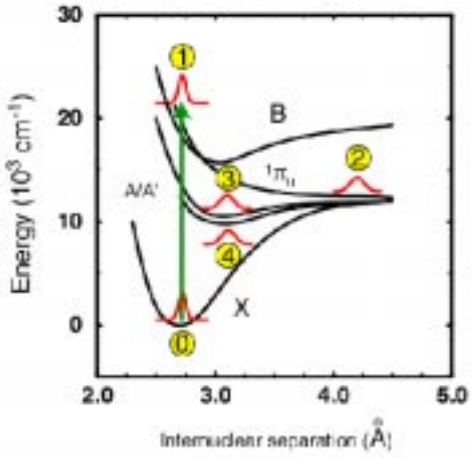

FIG. 9. Potential energy surfaces of iodine. The time evolution is shown schematically with the red wave packets numbered sequentially in time.

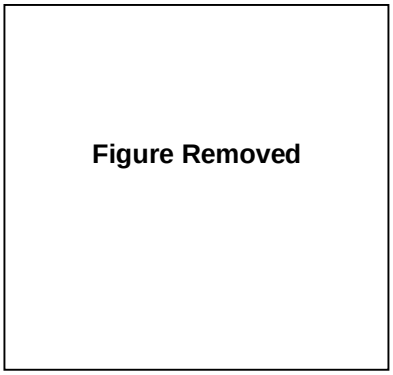

FIG. 10. Temporal response of the scattered signal measured using a lock-in amplifier. The solid line is the 80 ps x-ray pulse convoluted with a 500 ps exponential decay.

3. Background in pump-probe experiments

A common thread to all the experiments discussed in this section is the fact that the majority of the scattering is due to spectator molecules. In the gas-phase experiments, they are the unexcited molecules and the carrier gas. Similarly, in the condensed phase the majority of scattering is due to the solvent. These situations inevitably produce a high background that is difficult to handle. Neutze *et al*. used lock-in methods to improve their signal to noise, and Zewail *et al*. use a sophisticated subtraction technique.

Another approach to lower background in condensed-phase experiments is to use a rare gas crystal, such as Ne or Ar, as the solvent. The crystal structure provides a clean background and

the low Z number assures low scattering probability. This solvent is non-reactive and should therefore damage very slowly. There is also a large volume of frequency and time-domain research on photodynamics in these media available to provide the background for the LCLS.

A second approach for background reduction uses a stimulated Raman approach as discussed by

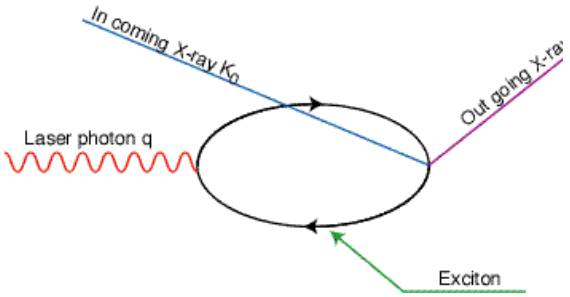

FIG. 11 Stimulated Raman diagram

S. Doniach. This method takes advantage of the fact that the scattering molecule that is of interest is in an electronically excited state. There is a finite probability that incoming x-ray photons with wave vector K_0 that are scattered to $K_1 = K_0 + q$ will include both excitation absorption (stimulated Raman, see Fig. 11) events and excitation scattering (stimulated Brillouin). The difference in energy between the two is equal to that of the difference between the ground state and the electronically excited state. All photons with wave vector K_1 are a result of scattering events with the desired molecules. This approach requires that the x-ray line width be significantly smaller than ε, which is on the order of 3-5 eV.

B. Biological systems

1. Dynamics of photosynthetic systems

Comparison of time-resolved excited-state structures of Ni(II) tetraphenylporphyrin (**1**), Ni(II) tetra-tert-butyl porphyrin (**2**) and Ni(II) dodecaphenylporphyrin (**3**) are proposed. These nickel porphyrins are low spin (d^8) in their ground state with Ni-N distances of 1.929 Å for **1,** 1.86 Å for **2**, and 1.88 Å for **3**. (Multiple conformations have been observed crystallographically for **3**.) The Ni-N distances are a good indicator of the macrocycle's deviation from planarity. Shorter distances reflect increased distortion. EXAFS studies have shown that the solid-state structures for these three molecules are retained in solution.

The photochemistry of Ni porphyrins is shown in Fig. 12. The ground state is excited to the singlet state, which relaxes and decays to a vibrationally and conformationally excited (d_z^2, $d_{x^2-y^2}$) state. This (d,d) state undergoes structural changes as it relaxes vibrationally and then decays back to the ground state. The vibrationally relaxed (d,d) state should have long Ni-N distances (~2.02 Å) to accommodate the larger nickel ion, due to the unpaired electron in the $d_{x^2-y^2}$ orbital. These structural transformations could result from the macrocycle becoming planar, doming, and/or the metal moving out of the nitrogen plane. For these Ni(II) porphyrins the (d,d) electronic excited state lifetimes vary from ~3 picoseconds to ~50 nanoseconds, depending on the solvent polarity, viscosity, and temperature, the specific porphyrins ground state conformation, and steric constraints.

Nickel L- and K-edge ultrafast XAS studies of these porphyrins will enable us to follow the excited-state structural dynamics, monitor the d-orbital occupancy, metal oxidation, and ligation state. Solvent and temperature dependence studies will also be performed to determine if different mechanisms of deactivation are present.

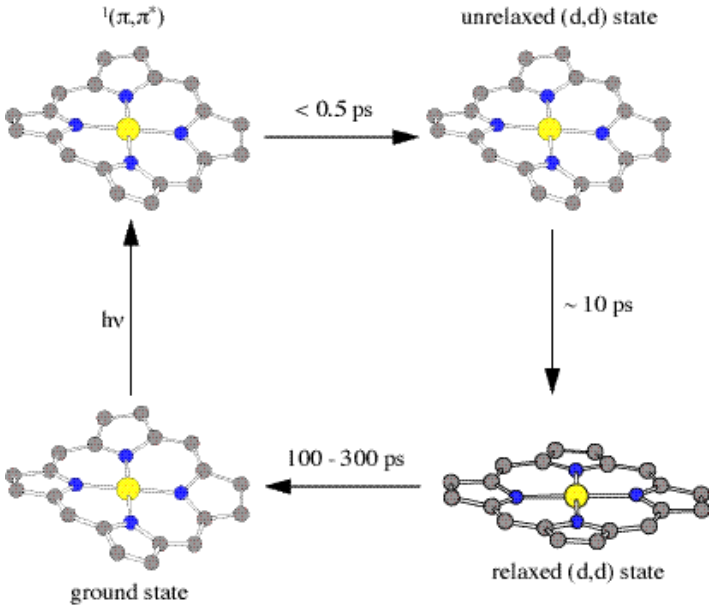

FIG. 12. Low-spin (d^8) Nickel(II) Porphyrins Deactivation Pathway.

The conformational changes shown in Fig. 12 associated with the vibrationally relaxed (d,d) state have been inferred from transient Raman measurements. The proposed experiments would provide the first direct structural information for the excited-state conformations and how they might modulate the decay pathways and lifetimes for planar and nonplanar porphyrins.

C. Laser melting of graphite

In a recent publication, Silvestirelli and Parrinello present the results of an *ab initio* molecular dynamics simulation of the laser melting of graphite. These calculations were performed in an attempt to simulate the experimental observations in which very short (~90 fs!) laser pulses were used to induce graphite melting. These experiments yielded observations of a laser-limited ultrafast increase in the reflectivity. Such transition to a more reflecting state is interpreted as a transformation of the system to a liquid, metallic phase. The time scale appears to be an order of magnitude faster than that expected by normal lattice melting.

The molecular dynamics (MD) simulations [22] show that the behavior of the laser-irradiated system depends crucially on the electronic temperature. Laser melting of graphite occurs only for local temperatures higher than 40,000 K. At this high temperature, many of the electrons occupy antibonding states. The strong repulsive forces drive the intramolecular covalent bonds to break before any intermolecular motions can take place. This is illustrated in Fig. 10, where the effect of electronic temperature on molecular bonding is clearly visible. The MD simulations predict that, when the electronic temperature reaches 40,000 K, the graphite system disorders within 50 fs, during which most of its covalent bonds break.

By combining time-resolved reflectivity experiments with ultrafast x-ray diffraction experiments, such as the one shown in Fig. 13, it should be possible to distinguish between the various mechanisms that may be responsible for the ultrafast melting observed.

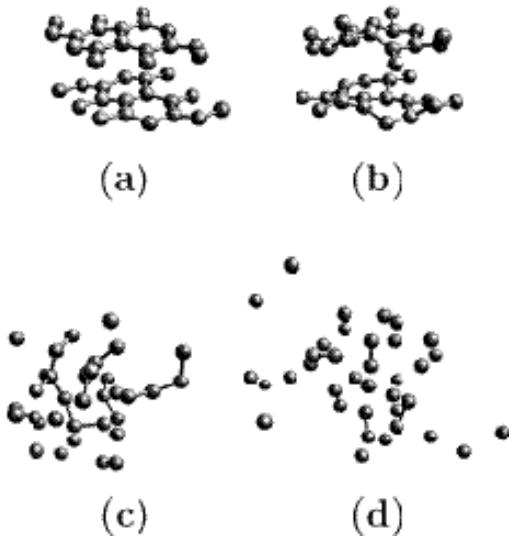

FIG. 13 Snapshots of selected MD configurations at different electronic temperatures a) 25,000 K, b) 35,000 K, c) 40,000 K, d) 50,000 K.

D. Dynamical processes in nanoparticles

The potential application of semiconductor and metal nanoparticles to the electronic and optical industry has provided an impetus for intense research. In the last few years, significant progress has been made in the study of the dynamic properties of charge carriers in semiconductors and metal nanoparticles, mainly through the use of femtosecond laser techniques. In conjunction with conventional spectroscopy and powerful microscopy techniques, preliminary understanding of the dependence of the charge-carrier lifetime on particle size, surface area, and shape is starting to emerge. Results suggest that in many of the nanoparticle systems studied, including CdS, CdSe, TiO_2, Fe_2O_3, PbS, PbI_2, Ag_2S, AgI, CuS, Mn-doped ZnS, Au, Ag, and Pt, the electronic relaxation process is dominated by surface trap states. No attempt has yet been made to characterize any structural changes that accompany or drive the electronic dynamics.

Size-dependent properties and extreme sensitivity to interactions at the interface due to the large surface-to-volume ratio are the two features that make nanoparticles extremely attractive. Yet, when particles are produced and studied in solution it is extremely difficult to control particle-solvent or particle-contaminant interactions. The dominance of the uncontrollable surface effects, combined with the nonuniform size distribution, make the study of size and surface effects on a fundamental level virtually impossible.

This program aims to utilize the LCLS to investigate the dynamics of structural transformations in nanoparticles, all of which are expected to be size dependent. It is clear that for this program to succeed it must first implement controls over particle size and interface. We propose to produce nanoparticles by homogeneous nucleation in the gas phase in a rare gas environment. This method will ensure that the resulting particles possess well-defined surface properties and sizes. Subsequent studies will be conducted either in the gas phase or in rare-gas crystals, in

order to minimize/control surface interactions. As previously noted, rare-gas crystal environments offer important advantage for x-ray scattering studies. Conditioning through gas-particle interactions will be used to control supercooling or supersaturation prior to observation or the imbedding step.

Metallic, semiconducting, and refractory nanoparticles can be generated by direct evaporation of the neat substance in a tube furnace operated at a high temperature in a stream of inert gas or in jet-flow reactors. In either case, the particles are formed when hot gas is cooled rapidly as it exits the heated zone. The resulting high gas-phase supersaturation induces homogeneous nucleation and the formation of small particles.

Although it may be possible to tune the center of the particle size distribution by controlling production conditions, the final size distributions tend to be rather wide. For experiments in which a monodispersed aerosol size is essential, it is possible to select a narrow size range from the overall aerosol population. This can be achieved using the recently developed nano differential mobility analyzer (NDMA), which is designed to select particles with diameters between 2 nm and 50 nm with a better than 1% precision. This instrument is designed to separate charged particles according to their mobility in an electric field. It allows for the selection of a narrow size range and the preparation of a macroscopic sample at atmospheric pressure. 10^5 single size particles/cc can be produced at flow rates of 2 liters/min. This sample can be concentrated further as it is deposited into the host crystal. For gas-phase studies on nanoparticle dynamics, it is possible to size-select particles by aerodynamically focusing a single size at the intersection of the light sources by controlling flow conditions.

1. Vibrational modes and capillary waves—Single particle dynamics

The proposed research will involve the study of nanoparticle vibrational and capillary wave dynamics in rare-gas crystal environments. Macroscopic Ne or Ar crystals can be easily grown on the tip of a standard liquid He cooled cryostat. It is possible to control particle concentration in the final crystals by selecting the He to Ne or Ar ratio in the gas-flow mixture.

In the initial phase a narrow size distribution will be selected using the NDMA and trapped in the Ne crystal. Their size distribution will be verified using static Mie scattering at the LCLS 0.15 nm wave length. To observe the dynamics, the sample is excited with a visible femtosecond laser and probed with the time-delayed LCLS recording the Mie spectra as a function of delay between the pump and the probe. Figure 14 shows a computed Mie spectrum for TiO_2 5 nm to 125 nm diameter particles obtained with 3.0 nm wavelength. The figure demonstrates the sensitivity of the Mie spectra to particle size. Moreover, the details of the Mie spectra can also be used to extract particle shape. However, because of inhomogeneous particle size and environment, a system that includes an ensemble of particles will quickly loose coherence and the sensitive Mie spectra would become difficult to interpret.

Clearly, the ideal solution to the above problem is to perform the experiment on individual particles at a time. Single-particle experiments should make it possible to observe the time evolution of the coherently prepared state, the coupling between electronic and nuclear, internal and surface modes, and finally the relaxation by energy transfer to the matrix. The high intensity, superior beam quality, and coherence of the LCLS make possible single-particle experiments.

Single-particle experiments will be performed on high-Z crystalline nanoparticles trapped in a Ne crystal. Metallic or semiconducting for which pump-probe optical experiments will first be used to characterize the electronic dynamics will be used. These will be followed by time-resolved x-ray diffraction experiments at the single-particle level.

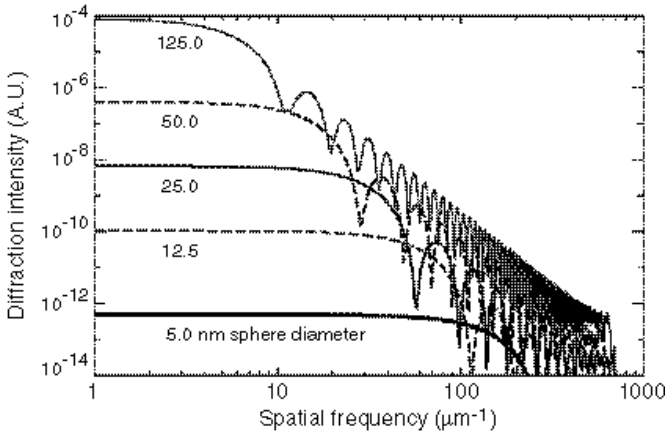

FIG. 14. Angular distribution (characterized in terms of spatial frequency in inverse microns) of scattering of 400 eV x rays from TiO_2 spheres of various diameters (1 m^{-1} = 3.1 mrad).

Homogeneous nucleation experiments require highly metastable conditions to drive the process. Bulk samples, which invariably contain a large number of solid impurities, cannot be used because these impurities catalyze nucleation near the thermodynamic-phase transition point and no homogeneous nucleation ever takes place. Nanoparticles, because of their small size, have an extremely low probability of containing any impurities. It is possible, therefore, to produce metastable nanodroplets that are extremely far from equilibrium in a controllable manner. These could be supercooled neat droplets or supersaturated solution droplets. Such highly metastable droplets provide a unique opportunity to study the dynamics of crystal formation in systems far from equilibrium.
Because the system can be driven to just below the nucleation threshold, it should be possible to induce nucleation by introducing a very small perturbation to lower the barrier and start nucleation process.

For example a supercooled solution of aromatic anthracene could be resonantly excited with a near UV photon. The presence of an exciton in the solution results in rapid exciplex formation, which is a form of a tightly bound molecular multimer. This newly formed cluster can now catalyze nucleation of the entire droplet. Time-delayed x-ray diffraction spectroscopy can then be used to follow the dynamics of crystal growth.

References

[1] *Femtochemistry and Femtobiology: Ultrafast Reaction Dyamics at Atomic Scale Reaction*, V. Sandstroem, ed, (World Scientific, Singapore 1997).

[2] *Ultrafast Chemical and Physical Processes in Molecular Systems*, M, Chergui, ed, (World Scientific, Singapore 1996).

[3] *Femtosecond Chemistry*, J. Manz and L., Woeste eds, (VCH, NY 1995).

[4] *Femtochemistry: Ultrafast Dynamics of the Chemical Bond*, (World Scientific, Singapore 1994).

[5] J. Phys. Chem. A **102**,.4021-4404, A. W., Castleman, Jr., ed., (1998).

[6] R. W. Schoenlein *et al.*, Science **274**, 236, (1996).

[7] C. Rischel *et al.*, Nature **390**, 490, (1997); R.W. Schoenlein *et al., Science* **287**, 2237, (2000).
[8] M. M. Murnane, *et al.*, Science **251**, 531, (1991).
[9] J. Larson *et al.*, Appl. Phys. A **66**, 587, (1998).
[10] C. Rose-Petruck *et al.*, Nature **398**, 310, (1999).
[11] A. H. Chin *et al., Ultrafast Phenomena XI*, T. Elsaesser, J. G. Fujimoto, D. A. Wiersma, and W. Zinth, eds. (Springer, Berlin, 1998), pp 401-403.
[12] A. Caveleri *et al.*, Quantum Electronics and Laser Science Conference `99.
[13] J. C. Williamson *et al.*, Nature **386**, 159-162, (1997).
[14] C. W. Siders, *et al.*, Science **286**, 1340-1342, (1999).
[15] J. Cao etal., Proc. Natl. Acad. Sci. **96**, 338-342, (1999).
[16] Neutze *et a,l* in preparation
[17] L. X. Chin *et al.*, J. Am. Chem Soc. **115**, 4373-4374, (1993).
[18] L. X. Chin et al., in preparation
[19] N. Bloembergen, Nature **356**, 110, (1992).
[20] L.R. Benedetti *et al.* Science **286**, 100, (1999).
[21] A. De Vita *et al*.Nature **379**, 523, (1996).
[22] P. L. Silvestrelli *et al.*, J. Appl. Phys. **83**, 2478-2483, (1998).

Studies of Nanoscale Dynamics in Condensed Matter Physics

B. Stephenson, *Argonne National Laboratory, Argonne, IL, USA*
S. Mochrie, *Yale University, New Haven, CT, USA*
M. Sutton, *McGill University, Montreal, Quebec, Canada*
K. Nelson, *MIT, Cambridge, MA, USA*
F. Sette, *European Synchrotron Radiation Facility, Grenoble, France*
G. Ruocco, *Universita' di L'Aquila, L'Aquila, Italy*
S. Dierker, *University of Michigan, Ann Arbor, MI, USA*
S. Sinha, *Argonne National Laboratory, Argonne, IL, USA*
D. Schneider, *Lawrence Livermore National Laboratory, Livermore, CA, USA*

I. SUMMARY

Most condensed matter exhibits complex dynamics. Viscoelastic flow, polymer reptation, protein folding, crystalline phase transitions and domain switching, and countless other *collective processes* show both fast and slow responses, often sensitive functions of temperature, applied fields, and fabrication parameters. These complex dynamics may be crucial for material function, as in synthesized structures such as gels and high-impact polymers and in natural structures such as proteins, whose folding dynamics involves a hierarchy of time scales. Complex dynamics also may be deleterious, as in ferroelectric DRAMS whose slow response components limit their practical switching times.

Using time- or energy-resolved light-scattering techniques, we can currently probe the full range of these time scales, from femtoseconds through kiloseconds. However, conventional measurements with visible and near-visible wavelengths probe responses on the distance scale of the wavelength or longer, that is, at least 0.1 microns and generally much longer. But in almost all materials, intermolecular interactions are short-range (angstroms) and correlations in quantities such as polymer or ferroelectric alignment, motions of polymer or protein subunits, or liquid-state molecular orientational alignment, extend over nanometers, not tenths of microns or longer. How do systems made out of angstrom-size molecules that only interact with neighbors nanometers away coordinate and organize their macroscopic (micron and larger distance scale) responses?

In many cases, we don't know. For example, do the essentially universal polymer responses that we observe on a hierarchy of time scales (assumed to obtain in protein folding and other biopolymer behavior as well) reflect the responses on a corresponding hierarchy of length scales — fast motions of small segments, slower motions of larger structural elements, even slower motions of whole polymer chains? If so, why do small-molecule viscoelastic liquids (including honey and molasses) show almost identical dynamical responses, with the same temperature-dependent trends, even though there are only microscopic-sized units? Our measurements reveal macroscopic dynamics, but not the mesoscopic (nanoscale) dynamics that give rise to them. Our theoretical and computational methods are inadequate for description of many-body complex dynamics, including complex molecules and structures and including the slow, as well as fast, time scales.

The Linac Coherent Light Source (LCLS) provides a unique opportunity to observe nanoscale dynamics in condensed matter systems over a wide range of time scales using x-ray photon correlation spectroscopy (XPCS) and x-ray transient grating spectroscopy (XTGS). The experiments proposed here explore dynamics over ranges of wave vector and time that are important in a variety of systems but are difficult or impossible to study with other techniques. Three initial experiments are proposed in the following areas:

1. Dynamics of entangled polymers
2. Structural basis of glassy dynamics
3. Collective mode dynamics in liquids and glasses

The common theme in these experiments is the interplay of multiple length and time scales in the dynamics. While the time scales of interest vary greatly (10^{-13} to 10^{3} s), in all three cases the length scales are in the atomic to nanoscopic range (10^{-1} to 10^{3} nm). This corresponds to wave vectors of 10^{-3} to 10^{1} A^{-1}. XPCS and XTGS provide a direct measure of the wave vector dependence of the dynamics over this range.

Three types of experimental techniques will be investigated:

a) Using the very high time-averaged coherent x-ray flux from the LCLS to carry out XPCS measurements over time scales from 10^{-3} to 10^{3} seconds;

b) Using the extremely high-peak coherent x-ray flux from the LCLS to carry out XPCS measurements using a split-ulse technique over time scales from 10^{-12} to 10^{-6} seconds;

c) Using the short pulse width from the LCLS to carry out XTGS measurements of stimulated dynamics over time scales from 10^{-12} to 10^{-6} seconds.

II. NEW CAPABILITIES THROUGH THE LCLS

The unprecedented brilliance and narrow pulse width of the LCLS will significantly advance the frontier of structural and dynamical studies of condensed matter [1]. Through its use, the time-domain light-scattering spectroscopies that have been used extensively but limited to low-scattering wave vectors (i.e., long material length scales) will be extended into the x-ray regime. This will give access to nanoscopic length scales from microns to angstroms, over the full-range time scales from femto- to kiloseconds.

This section will first focus on experiments using the high coherent flux to perform XPCS studies of nanoscale dynamics in condensed matter. Consideration will also be given to the use of the short pulses provided by the LCLS in a complementary method, XTGS. This is an active time-domain approach, in which material responses are driven by excitation pulses and monitored by time-delayed probe pulses. We will then consider feasibility issues, such as the general conditions under which heating of the sample by the x-ray beam will limit the extent to which the additional brilliance of the LCLS can be used for studies of dynamics.

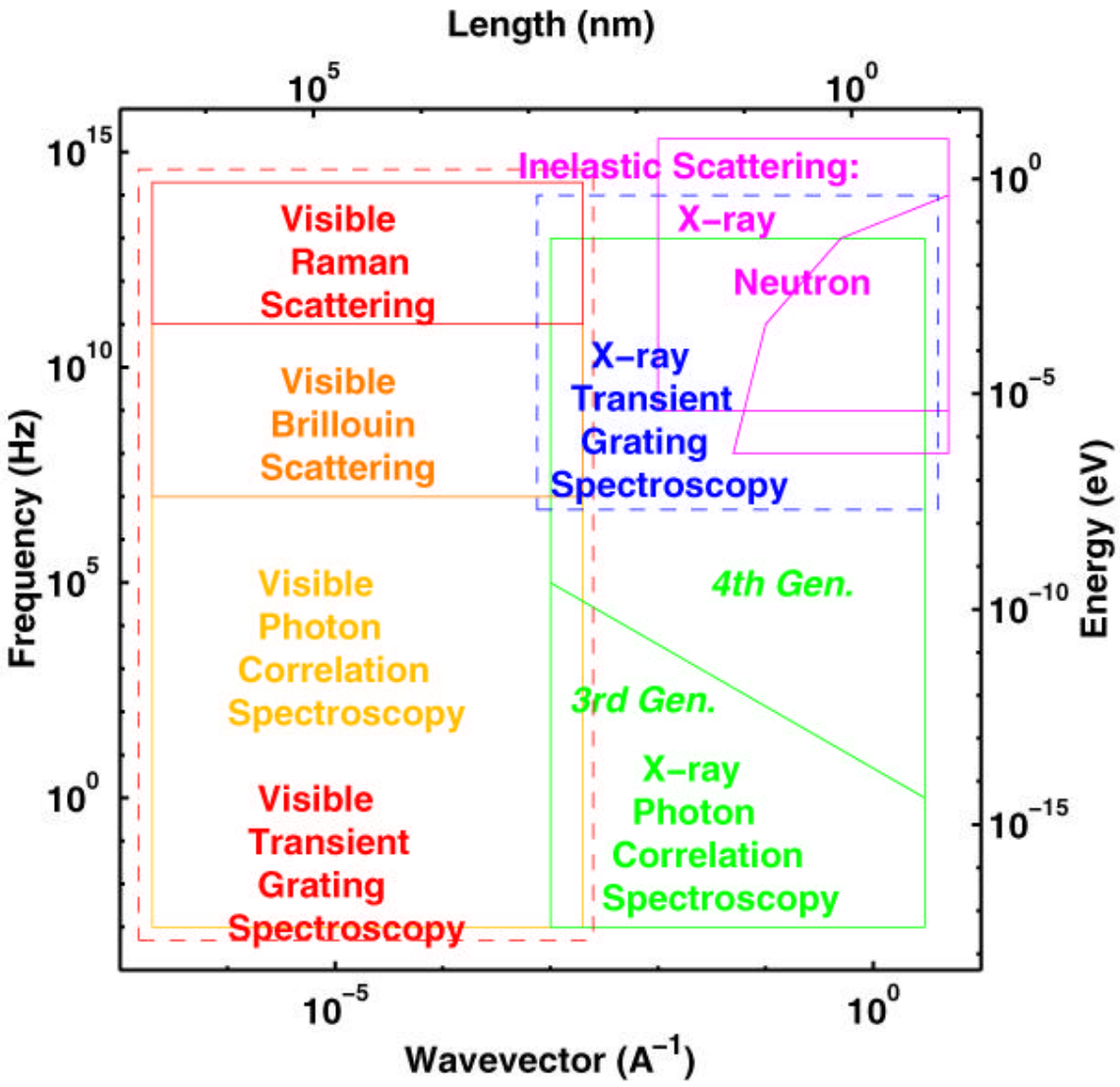

FIG. 1: Plot of the frequency-wave-vector space relevant to dynamics in condensed matter and the regions covered by various probes of equilibrium dynamics (after [2]). Active (transient grating) methods are indicated by the dashed enclosures.

Figure 1 shows the relationship between the proposed techniques of XPCS and XTGS to other techniques for probing equilibrium dynamics [2]. The experimental challenge is to measure the dynamic structure factor $S(Q,\omega)$ or the corresponding response function $S(Q,t)$ in the appropriate region of frequency ω (or time t) and wave vector (Q) space. The figure shows that XPCS could provide a time-domain, small-length-scale spectroscopy highly complementary to other techniques, uniquely covering ω lower than 10^8 Hz and Q larger than about 10^{-3} A^{-1}, as well as the gap between visible and neutron techniques at high ω in the nanoscopic length scale regime. XTGS measurements could provide unique active time-domain access to fast processes at high Q.

The time (energy) and length (wave vector) ranges covered by XPCS and XTGS experiments at LCLS are of great interest for the study of dynamics in many research areas at the frontier of condensed matter physics and chemistry [1]. Examples of problems that could be addressed are:

Simple Liquids **–** Transition from the hydrodynamic to the kinetic regime.

Complex Liquids – Effect of the local structure on the collective dynamics.
Polymers – Entanglement and reptative dynamics.
Glasss Formers – Vibrational and relaxational modes in the mesoscopic space-time region.
Dynamic Critical Phenomena – Order fluctuations in alloys, liquid crystals, etc.
Charge Density Waves – Direct observation of sliding dynamics.
Quasicrystals – Nature of phason and phonon dynamics.
Surfaces – Dynamics of adatoms, islands, and steps during growth and etching.
Defects in Crystals – Diffusion, dislocation glide, domain dynamics.
Ferroelectrics – Order-disorder vs. displacive nature; anisotropic correlations and size effects.

A description of current XPCS technique and the status of XPCS measurements at operating third-generation sources are available in recent workshop reports [1] and articles [3,4]. The use of XPCS has been limited to date by the availability of sufficient coherent x-ray flux. Since the flux of coherent x-rays is proportional to the source brilliance, XPCS studies benefit directly from higher brilliance sources. The modest coherent x-ray flux available at third-generation synchrotron sources makes XPCS measurements currently feasible at ω up to the kHz range, depending upon Q and the scattering efficiency of the material [3]. The impact of the high-coherent x-ray flux from LCLS and future fourth-generation sources will be to allow XPCS measurements at higher ω and on a greater variety of materials, overlapping with energy-domain measurements using neutron and x-ray inelastic scattering.

III. SCIENTIFIC OBJECTIVES

A. Experiment 1. Dynamics of entangled polymers

On the macroscopic scale, long-chain polymer liquids exhibit a dramatic visco-elastic response, responding elastically at short times but flowing at long times. Many of the properties of high-polymer liquids may be understood on the basis of the reptation model of polymer dynamics, which depicts the motion of a polymer as a random walk along a tube delimited by temporary entanglements with neighboring chains [5], as illustrated at the top of Fig. 2. For concentrated solutions, aspects of this model have been confirmed via fluorescence microscopy studies on labeled DNA [6] and on actin filaments [7], as well as by laser correlation spectroscopy studies of very long-chain diblock copolymers in toluene [8]. In polymer melts, features predicted by the reptation model have been seen in measurements of the macroscopic diffusion constant [9] and in interdiffusion experiments [10]. Microscopic evidence for the existence of the tube and its corresponding entanglement length has been provided by neutron spin-echo (NSE) measurements [11], which have characterized the relaxations within the tube (Rouse modes). However, the delay times accessible with NSE are shorter than needed to observe reptative relaxation directly, and important aspects of the reptation model remain untested after more than twenty years. One of the most remarkable predictions of the reptation model is that small-scale compositional fluctuations with $Q^2 R_G^2 >> 1$ show a wave-vector-independent relaxation rate (Γ), given by the inverse of the disentanglement time (τ_d) for a polymer to reptate out of its original tube [12]. (Q is the wave vector and R_G is the polymer radius of gyration.) This prediction stands in contrast to the diffusive behavior ($\Gamma \propto Q^2$) expected for polymers at small Q, and to the $\Gamma \propto Q^3$ or $\Gamma \propto Q^4$ behavior in non-entangled polymers [13], and is experimentally untested. The predicted intensity autocorrelation function (g_2) is illustrated at the bottom of Fig. 2 for three values of Q. At small times g_2 decreases as a universal function of $Q\sqrt{t}$ as a result of Rouse modes within the tube, to a Q–dependent plateau value, given by the tube diameter. NSE has been used to characterize the

early time behavior, but how this connects to the behavior at long times and understanding the long time relaxations themselves await XPCS measurements at the LCLS. Physically, this behavior occurs because to relax a small-scale compositional fluctuation, it is nevertheless necessary for polymers to disentangle, which requires a time τ_d. From this point of view, it is clear that the polymer radius of gyration is an important length scale for blend dynamics, in addition to the correlation length for compositional fluctuations. Also a puzzle is what determines the tube diameter and the distance between entanglements. Present theory assumes the existence of an entanglement distance without being able to calculate it. New experiments might yield key insight into resolving the question of what determines the entanglement length in blends and melts. Thus, it seems imperative to probe polymer motions in melts and blends at length scales comparable to and smaller than the polymer radius of gyration, and on time scales comparable to the disentanglement time.

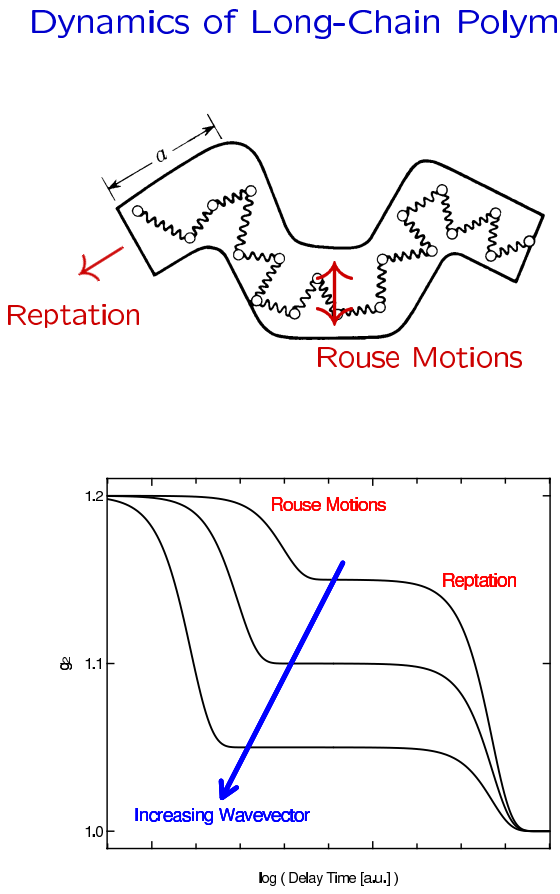

FIG. 2: Top: Schematic of polymer motions. Bottom: Predicted blend intensity autocorrelation function.

The emerging technique of XPCS has recently been shown to be capable of studying the slow dynamics of colloidal systems at small length scales [3]. In a preliminary XPCS study of dynamics in a binary blend of poly(ethylene oxide) and poly(methyl methacrylate) at the Advanced Photon Source, it was found that the application of XPCS to polymer blends is far more challenging than to colloids, because of the smaller scattering cross section in blends. Experiments at the LCLS will provide definitive measurements of the time-dependent relaxation of polymer blend concentration fluctuations. Such measurements will allow a test of the dynamic random

phase approximation (RPA) predictions for reptation relaxation. The dynamic RPA yields collective blend dynamics from single-chain motion. For a monodisperse, entangled melt of flexible polymers, the dynamic RPA predicts a crossover in the dependence of the relaxation rate on Q from an approximately quadratic dispersion relation to a nondiffusive regime at large Q, where the relaxation rates become Q-independent.

The macroscopic viscosity of a polymer is typically large, because of the proximity of its glass transition. Similarly, the microscopic dynamics of long-chain polymers are very slow, with time scales typically longer than 10^{-2} s. This means that it will be possible to employ the very high time-averaged coherent x-ray flux from the LCLS, averaged over the 8 ms repetition rate, to investigate the reptative dynamics in polymer blends using data reduction/analysis techniques that are similar to those used now. Such an experiment consists of collecting a sequence of speckle patterns on an area detector for each pulse of the LCLS. From an analysis of these sequences, correlation times from a few repetition times up to many minutes can be measured.

B. Experiment 2. Structural basis of glassy dynamics

Many liquids, when rapidly cooled below their melting points, form a metastable glassy or amorphous phase intermediate between a liquid and a solid. This is the case for a wide variety of materials including metallic alloys, oxides such as silica (e.g., window glass), polymeric materials (plastics), and a long list of others. It is clear that glassy materials are one of the most important classes of materials in everyday use. However, in spite of their ubiquity, they are probably one of the least understood materials at a fundamental level. For instance, conventional equilibrium statistical mechanics does not predict the existence of, or even strictly apply to, the amorphous state, whereas it can explain most other states of matter, even quite exotic ones like superconductivity and superfluidity. Understanding visco-elastic effects in glassy materials is currently a topic receiving heavy activity.

Glassy systems are defined by the nature of their dynamics. In a typical glass-forming system, the viscosity increases exponentially by many orders of magnitude as temperature is lowered, until viscous flow processes are effectively frozen. Much has been learned about dynamics in glass-forming systems using light scattering and nuclear magnetic resonance imaging. Relaxation processes with time scales associated with viscosity are called primary (α) processes. Other, much faster processes, called secondary (β) processes, are also seen near the glass transition [14]. It is still an open question as to the nature of these modes and the role they play in the glass transition. Recently, mode coupling theory [14,15] has received much attention as a possible explanation of glass transition dynamics.

The temperature at which a cooled liquid transforms into a glassy state depends on the rate of temperature change. There is also a hysteresis upon heating and cooling. This leads to a dichotomy. Tests for a true thermodynamic transition require slow rates to look for the underlying thermodynamic phase transition but still be fast enough to avoid crystallization. Studies using light scattering [16], neutron scattering [17,18], and recently inelastic x-ray scattering [19] have examined phonon-like modes in these systems, which have seen changes such as the slopes of these frequencies with temperature near the glass transitions. Usually, measurement times are long, making the systems difficult to study in the most interesting region, which is as they undergo the glass transition.

XPCS measures the time constants of a system as a function of wave vector and gives direct information on the dynamics. The region of Q and ω covered by XPCS will be very important in understanding the structural nature of the dynamics in glass-forming systems at the atomic and

nanoscale. We propose studies spanning a very large range of time scales (10^{-12} to 10^{3} s) in order to observe the evolution of the dynamics from liquid to glassy behavior as the temperature is lowered. There are many possible systems for study, but a good first candidate is B_2O_3. This is random-network glass with well-understood macroscopic properties [20], and on which complementary Raman [21] and neutron scattering [22] studies have been performed. Its low electron density helps minimize adiabatic heating by the beam, as described below.

The current XPCS technique, using the high average brilliance to record a sequence of speckle patterns for subsequent time-correlation analysis, will be used to probe time scales longer than the repetition rate of the source (8 ms). We propose to use a split-pulse technique, taking advantage of the instantaneous brilliance of the LCLS, to probe time scales between 10^{-12} and 10^{-6} s. The concept of the technique is to split each x-ray pulse into two equal-intensity pulses separated in time. The scattering from the two pulses will then be collected during the same exposure of an area detector. If the sample is static on the time scale of the two pulses, then the contrast in the summed speckle pattern will be the same as that from a single pulse. If the sample evolves on this time scale, then the summed speckle pattern will have lower contrast. Thus by analyzing a set of such patterns, each for a different time delay, the correlation times of the system can be measured. A pulse splitter with a path length difference variable from 3 x 10^{-4} to 3 m would give delay times from about 10^{-12} to 10^{-8} seconds. Longer time delays between pulses may be possible using two electron bunches in the free electron laser (FEL). With the planned pulse structure of the LCLS, there may be a gap between about 10^{-6} and 10^{-3} s in the time scales accessible by the time-averaged technique and the split-pulse technique.

C. Experiment 3. Collective mode dynamics in liquids and glasses

Atomic motions in crystals can be described in terms of collective oscillations around equilibrium positions. Qualitative differences occur as soon as the microscopic crystalline order is abandoned. In contrast to the crystalline case, the disordered system is characterized by two different length scales: In addition to the inter-particle separation, a, one must also consider the correlation length characterizing the topological disorder, ξ. In this case, the understanding of the atomic dynamics is complicated not only by the difficulties associated with the absence of translation invariance, but also by the presence of other degrees of freedom, such as diffusion and relaxation in fluids, and hopping and tunnel processes in glasses. The presence of these processes in disordered systems naturally introduces a time-scale, τ, usually strongly dependent on the specific thermodynamic state. This time-scale affects the collective dynamical properties differently, depending on its value with respect to the time scale t_D, characterizing the "vibrational" dynamics of the particles around their quasi-equilibrium position. This is of the order of the inverse of the Debye frequency, whose value is comparable to that of a corresponding crystal with similar density and sound velocity. The rich phenomenology observed in the dynamics of disordered systems is, therefore, often the consequence of the interplay between these different structural (a and ξ) and dynamic (τ, t_D) scales.

The collective dynamics in the absence of translation invariance can be easily treated theoretically in two limiting cases, namely excitations with characteristic space and time scales which are either very long or very short compared to the disorder scale ξ , and to the relaxation time τ, respectively. They are respectively the hydrodynamic limit, where the system is seen as a continuum, and the single-particle kinetic limit, where the particle behavior is described as a free particle between successive collisions. In contrast, an exhaustive theoretical understanding is still not available in the intermediate, mesoscopic, region, defined by a length scale comparable to the correlation length of the topological disorder and by a time scale comparable to t_D.

Brillouin light scattering (BLS) and inelastic neutron scattering (INS) are traditionally used to study the mesoscopic space-time domain in crystals, corresponding to a time-momentum region of 100 to .01 ps and 0.001 to 10 nm^{-1}. In disordered systems this mesoscopic space-time domain has been much less studied because the INS technique suffers from important kinematics limitations that can be overcome only in crystals by the choice of a high-order Brillouin zone, where it becomes possible to map the desired phonon branch. For this reason one can explain why, in disordered systems, a comprehensive experimental picture of the high-frequency collective dynamics is still missing.

The outlined scenario has left open several relevant questions on the mesoscopic dynamics of disordered materials. Among them, we mention the following:

1. Are there collective excitations in liquid and glasses with wavelengths approaching x and a? And, if so, to what extent do their eigenvectors deviate from the plane waves found in crystals? Are these deviations responsible for the anomalous thermal conductivity found in glasses at low temperatures? Similarly, how do they relate to the sound excitations observed in the long wavelength limit?

2. With respect to the Debye behavior of the corresponding crystal, what is the origin of the excess specific heat at low temperature and the excess density of vibrational states found in glasses?

3. What is the microscopic description of hopping and tunnel phenomena in glasses, and of relaxation processes in liquids?

4. Are short-wavelength excitations still affected by relaxation processes as are the long wavelength ones, observed, for example, in light-scattering and ultrasound measurements? This last point relates to the issue of how the high-frequency dynamics may be affected by the liquid-glass transition in glass-forming systems, and whether any critical behavior is present in these dynamics.

We propose to carry out measurements of these phenomena by extending the transient grating techniques currently used for visible light studies [23] to x-ray wavelengths. Such XTGS experiments are based on the splitting of the beam into three components.

Two beams are used to produce a standing wave with periodicity $\Lambda = 2\pi/Q$, where $Q = 2k_o \sin \theta_s/2$. Here, k_o is the wave vector of the incident photons while θ_s is the incidence angle between the two *transversely* coherent beams producing the standing wave. If a sample is positioned in the standing wave, the electromagnetic field is expected to produce a *density* modulation in the sample with the same periodicity Λ. The standing wave field will exist for the pulse duration (200 fs), and therefore also the density modulation in the sample will be created in a comparable (or longer) time scale. The third pulse is the probe pulse. It measures the time-dependent amplitude of the density modulation. The probe pulse and the two excitation pulses do not have to have a well-defined phase relationship, and they can be different frequencies. This is done by looking at the intensity of the third beam after Bragg scattering from the density modulation of periodicity Λ, providing that the third beam impinges on the sample with a known delay with respect to the time of creation of the density modulation. In some configurations, heterodyne detection permits the field of the scattered beam to be measured directly.

The interest is to perform these experiments at density modulations with periodicity in the 1-100 nm region (Q = 0.05-5 nm^{-1}), where the expected frequency of collective acoustic excitations in condensed matter is (assuming a sound speed of ~3000 m/s) in the range 40–0.4 THz, i.e., excitations with characteristic energy in the 10-0.1 meV region and time in the 0.025–2.5 ps region.

This implies that, with k_o = 4.2 A^{-1}, the angle q_s will be in the 150-1.5 mrad region. The uniqueness of this instrument is its ability to help bridge the momentum gap existing at present in the study of propagating collective excitations (sound modes). Using BLS one can study excitations up to 0.04 nm^{-1} with the desired energy transfer, while using inelastic x-ray scattering (IXS) one can study excitations down to 0.8 nm^{-1}, also with the desired energy transfer. When using INS, one is strongly limited in the energy transfer by the neutron kinematic constraints existing at the considered *Q*-values. This method is basically impossible to use for excitations with a velocity of sound larger than 1.5 km/s. The present instrument should be able to fill the unexplored momentum gap. Just as important, the XTGS measurements should permit unambiguous determination of heavily damped and over-damped dynamics in the same wave vector range covered by other experiments, which do not resolve these responses well. Since high-wave-vector acoustic modes become over damped in essentially all disordered and partially ordered liquids and solids, and the crossover between under-damped and over-damped modes reveals the important static and dynamic correlations that scatter the phonons, direct experimental access to this regime of behavior is of interest in a very wide range of samples.

IV. EXPERIMENTAL DETAILS

A. Feasibility assessment: adiabatic heating

The pulsed structure of the LCLS presents a significant challenge to the feasibility of XPCS measurements, because of the potential for radiation damage. This is an important issue not just for XPCS but also for any application of a fourth-generation source as a non- or weakly interacting probe. Although a detailed understanding of the interaction between high-peak-power x-ray beams and matter will be one of the major areas of scientific investigation at the LCLS, based on the analysis presented here, it appears that XPCS studies in a weakly interacting regime will be feasible. One primary area of R&D needed for planning XPCS experiments at the LCLS will be to better understand the threshold for radiation damage to the sample.

The feasibility of XPCS at the LCLS can be assessed for different sample compositions and x-ray energies by comparing three quantities: N_{MIN}, the minimum required number of photons per pulse to give sufficient signal per speckle; N_{MAX}, the maximum tolerable photons per pulse to avoid sample disturbance; and N_{AVAIL}, the photons per pulse available from the LCLS.

For dynamics studies, one would like to avoid heating the sample by more than a few degrees during the measurement. With a subpicosecond pulse, the illuminated area will be heated adiabatically—there will be no time for significant heat flow by conduction or thermal radiation. Since it will generally be possible to reduce the thermal time constant of a thin (e.g., 10-micron-thick) sample to less than 1 millisecond, only the heating from each individual LCLS pulse need be considered. The simplest approximation is that the total energy of absorbed photons from a pulse is deposited in the illuminated volume. (This may be a conservative approximation if there is significant escape of fluorescent x-rays or electrons.) To a first approximation, the heat capacity per atom is given by $3k_B$, where k_B is the Boltzmann constant. Thus, the maximum number of photons per pulse is

$$N_{MAX} = \frac{3k_B A}{E\,\sigma_{abs}}\,\Delta T_{MAX}\ ,$$

where A is the beam area, E is the photon energy, σ_{abs} is the absorption cross section per atom, and ΔT_{MAX} is the maximum tolerable temperature rise. The proportionality between N_{MAX} and

ΔT_{MAX} is thus only a function of E, A, and the atomic number(s) (Z) and fractions of the element(s) in the sample; it is independent of sample density or other properties.

The minimum photons per pulse N_{MIN} needed in an experiment depends on the signal level per incident photon. For a scattering experiment, higher Z atoms will scatter more strongly. If the illuminated volume is determined by the absorption length, more atoms will contribute when there is less absorption. For an idealized sample with uncorrelated atomic positions, intensities scattered per atom can simply be summed. The angle-integrated number of elastically scattered photons per incident photon is then given by σ_{el}/σ_{abs}, where σ_{el} is the total scattering cross section per atom. The actual signal level per incident photon in a scattering experiment will depend strongly on the atomic arrangement in the sample, and the position and resolution in reciprocal space. In general, the signal level per incident photon will be higher by a factor equal to the effective number of atoms scattering in phase (M_{corr}). For XPCS measurements, the solid angle subtended by a single "speckle" is given by λ^2/A. Thus the minimum required incident photons per pulse can be expressed as

$$N_{MIN} = \frac{2\pi A E^2 \sigma_{abs}}{h^2 c^2 \sigma_{el} M_{corr}} N_{MIN}^{SP} ,$$

where N_{MIN}^{SP} is the minimum number of scattered photons per speckle required for XPCS. This depends upon the number of equivalent (equal-Q) speckles (e.g., 10^4), the number of repetitions with successive LCLS pulses (e.g. 10^4) and the instantaneous contrast of the speckle pattern due to resolution, etc. (e.g., 10^{-1}). Based on experience with similar analysis in current experiments we estimate the required value of N_{MIN}^{SP} to be 10^{-2}.

Figure 3 shows a comparison of N_{MIN}, N_{MAX}, and N_{AVAIL} as a function of sample composition for two energies, using $\Delta T_{MAX} = 1K$, a beam area of 10^{-4} cm^2, and two types of samples: $M_{corr} = 10$, corresponding to a typical liquid or glass, and $M_{corr} = 10^3$, corresponding to nanoscale clusters, e.g., in a polymer blend. The horizontal lines give the available photons per pulse from the LCLS for a bandwidth of 10^{-4} typically required for XPCS. The calculation predicts that XPCS will be feasible at the LCLS when the value of N_{MIN} is lower than both N_{MAX} and N_{AVAIL}. Since N_{MIN} and N_{MAX} vary oppositely with σ_{abs}, the result depends strongly on sample composition and photon energy. For studies of liquids or glasses, Fig. 3 predicts that the average sample Z would have to be below 7 (nitrogen) at 8 keV, or 13 (aluminum) at 24 keV (although available intensity may be the limiting factor at 24 keV). For studies of nanoscale dynamics, a much wider range of sample compositions could be used, including heavier elements with judicious choice of photon energy with respect to absorption edges. Because of the order-of-magnitude uncertainty in several quantities, these calculations do not provide exact limits, but do indicate that feasibility will depend upon sample composition and scattering power.

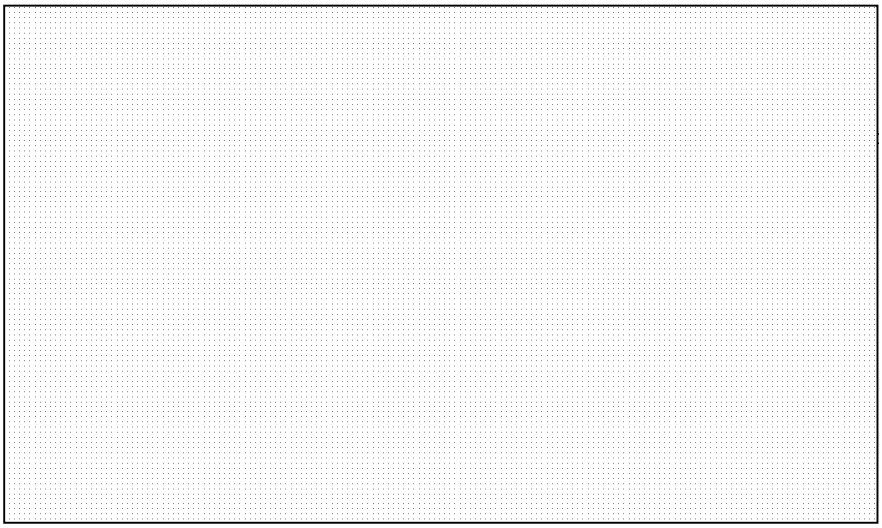

FIG. 3: Comparison of calculated number of photons per pulse required for XPCS, tolerable due to adiabatic heating, and available from the LCLS, as a function of sample composition, at two energies.

The threshold calculated here for adiabatic sample heating of 1K is a more stringent damage criterion than typical radiation damage thresholds found at third-generation x-ray sources for "soft" materials. For example, an x-ray damage threshold of 2000 kGy has been found for polymers in XPCS studies by Dierker, which corresponds to about 5×10^{13} photons per 10^{-4} cm^2 at 8 keV. The thresholds given in Fig. 3 are significantly lower than this value. Thus the unprecedented x-ray flux per pulse from the LCLS introduces a new facet to radiation damage issues.

B. Feasibility assessment: transient grating technique

For the XTGS technique, the envisioned experimental setup foresees the interference of two coherent x-ray beams (pump beams), which generate, in the investigated sample, a density modulation with a spatial periodicity in the subnanometer range. This density modulation, created in a time of the order of the LCLS pulse length (~200 fs), has an amplitude that is monitored as a function of elapsed time, t, with a third x-ray beam (the probe beam). This read-out method is based on the monitoring of the intensity of the probe beam coherently scattered by the density modulation.

Hereafter we report a brief discussion on the main mechanisms expected to produce the density modulation and a description of a possible layout for the proposed experiment.

The transverse coherence properties of the LCLS allow us to envisage the creation of a standing wave field for the electric field of the emitted radiation. This can be obtained by splitting the FEL beam in two components that are recombined at an angle θ_s. Considering that this standing wave can be formed only for a time equal to the FEL pulse length, T, the two beam paths must be kept equal within a value that is small with respect to cT~60 μm, where c is the speed of light. This is done routinely in the optical regime, and should be straightforward with x-rays. Under this condition, the standing wave field is created for a time T in a spatial region determined by the angle between the two pump beams and by their transverse dimensions. The periodicity is given by $\Lambda = \pi / (k_o \sin \theta_s/2)$ along the direction perpendicular to the bisector of the two pump beams incident directions.

We consider now a sample placed in the standing wave field. Because of absorption processes, the energy of the standing wave field is transferred to the sample. This absorption is dominated,

in the considered x-ray region, by photoelectric absorption from core electronic states. Considering values of λ much larger than the interatomic distances, the absorption will take place with a spatial modulation of periodicity λ, because vanishing (high) absorption is expected in the region of the nodes (anti-nodes) of the electric field. We now make the sensible assumption that a large amount of the de-excitation processes take place by nonradiative decays that, at the end, release the energy initially in the standing wave into the sample. We also assume that this thermalization process takes place on a spatial scale much smaller than λ and therefore induce a temperature modulation in the sample interaction region with periodicity λ. This temperature modulation, in turns, produces a density modulation. The aim of the experiment is the determination of the time evolution of this density modulation created during the interaction time T.

The efficiency of the described process, i.e., the amplitude of the density modulation, will linearly depend on the energy density of the standing wave field. From this point of view, it is important to have: 1) sufficient excitation pulse energy, as provided by the LCLS and 2) absorption length l_a yielding sufficient absorption through the depth of the sample. We estimate that the flux of the pump beam is expected to be 2×10^9 photons/pulse and its total energy $\Delta Q = 2.5\ 10^{-6}$ J/pulse.

An estimate of the produced density modulation $\Delta\rho$ can be made as follows. With ΔQ the average energy, the peak-to-valley energy released in the sample is $2\Delta Q$, and the peak-to-valley temperature modulation is $\Delta T = 2\Delta Q / C\ V\ \rho$. C is the specific heat of the sample, ρ is the mass density, and $V \sim \lambda_a\ d^2$ the volume of the interaction region. The density modulation amplitude is then obtained from:

$$\Delta\rho / \rho = \alpha\ \Delta T = 2\ \alpha\ \Delta Q / C\ \lambda_a\ d^2\ \rho,$$

with α the thermal expansion coefficient.

We consider now a probe x-ray beam that is Bragg scattered from the density modulation: Its intensity is directly related to the amplitude of the density modulation $\Delta\rho$. In the assumption of kinematic diffraction conditions, the integral reflecting power, I, is given by (taking the Debye-Waller and polarization factors equal to unity):

$$I = (r_e^2\ \lambda_a\ \lambda^3 / 2 \sin 2\theta_B) (| F |^2 / V^2),$$

where r_e is the classical electron radius and F is the form factor of the Bragg reflection, i.e., in our case, the Fourier component with wavelength λ of the electron density modulation associated to $\Delta\rho$. This quantity, in the case of monatomic samples, is given by $F = \Delta\rho\ V\ Z / M$, with Z and M the atomic number and atomic mass, respectively. The Bragg reflectivity, R, is obtained from the total reflecting power as $R = I / \Delta\theta$. $\Delta\theta$ is the angular width of the reflection and can be expressed as $\Delta\theta \sim \lambda / 2 \cos\theta_B\ \lambda_a$. Finally:

$$R \sim 2\ (Z / A)^2\ (r_e^2\ \lambda^2 / d^4)\ (\alpha\ \Delta Q / m_N\ C)^2\ ,$$

where A is the atomic weight and m_N is the nucleon mass. In some configurations, heterodyne detection yields a signal that varies linearly rather than quadratically with the sample response.

On the basis of this expression it is possible to estimate the reflectivity expected for specific systems. We note that it is very important to have pump beams with transverse dimension d as small as possible, but with the high pulse energy provided by the LCLS the limitation will likely be sample damage not pulse intensity. Note also that the reflectivity does not depend too much on a specific atomic species considering that Z/A is almost constant and of the order of 0.5. Moreover we notice the independence of R from the absorption length λ_a. This is at first sight

surprising and can be understood considering that, on one hand, with decreasing l_a, the magnitude of the density modulation increases, but, on the other hand, the efficiency of the kinematic Bragg reflectivity of the probe beam decreases. The two effects cancel each other. The last two considerations seems to imply that this technique can be utilized with comparable efficiency with any atomic species. Finally, we also notice the strong dependence on the wavelength of the probe beam.

As an example, we consider water. Using $r_e = 2.82\ 10^{-15}$ m, $m_N = 1.67\ 10^{-27}$ kg, $l = 1.5\ 10^{-10}$ m, $d = 10^{-4}$ m, $DQ = 2.5\ 10^{-6}$ J, $Z = 10$, $A = 18$, $l_a = 10^{-3}$ m, $a = 2\ 10^{-4}$ m, and $C = 4180$ J/kg, we get $Dr/r = 2.5\ 10^{-5}$, $DT = 0.1$ K, and $R = 6\ 10^{-6}$.

Considering that the intensity of the probe beam, which can have a bandwidth up to 10^{-3}, could be of the order of 10^{12} photons/pulse, we see that for this specific example one should get a very high signal in the Bragg scattered beam. One should consider, however, that this example is a fairly ideal situation because the chosen example of water is particularly favorable for the large value of the thermal expansion coefficient. Nevertheless, assuming that experiments should be possible with count rates as low as 1 count/s, and that the LCLS repetition rate is ~100 Hz, one can probably accept a Bragg reflectivity down to 10^{-10}-10^{-12} and intensity reduction of the probe and pump beams of ~10^{-2} with respect to the values reported in the previous example.

On a general basis, one can envisage a method based on collimating pinholes and, possibly, multilayers optics to isolate the LCLS FEL first harmonic, which has a bandwidth of 10^{-3}, from the undulator spontaneous emission. Using thin silicon or diamond crystals in Bragg conditions one could split the two pump beams from the undulator beam, while the transmitted beam is the probe beam. In order to generate the two pump beams, a possible scenario could be based on the commonly used strategy of diffraction of ±1 orders from a crystal grating. The two beams are then recombined by subsequent diffraction from two additional gratings. This method has the advantage (relative to reflective optics) of not requiring a narrow x-ray spectral bandwidth. The transient grating wave vector in this scenario is determined by the crystal grating, and a library of such gratings is envisioned for the highest wave vectors. For somewhat lower wave vectors (still above those accessible with optical wavelengths), x-ray lithography gratings (already available with 50 μm spacings, and continually progressing toward shorter spacings) can be used. In this setup, the probe pulse can be sent through the same gratings so that it arrives at the sample at the phase-matching angle for diffraction off the transient grating. A small angle out of the plane of the excitation pulses can be used to separate the diffracted beam from the excitation pulses. Alternatively, a different probe wavelength may be selected, in which case spatial separation is achieved even with all the beams in the same plane. Using diffractive optics in this manner, the probe beam is taken from one order (say, +1) of diffraction, and the other (-1) order can be used as a reference beam for a heterodyne measurement. This provides strong enhancement of signal and signal/noise levels because the signal intensity varies linearly, rather than quadratically, as a function of the sample response (i.e., as a function of the extent of sample heating and the resulting density change).

We note that an alternative method for setting up the XTGS experiment is provided through the use of a four multilayer mirrors device. Here, two fractions of the beam from the channel cut are symmetrically sent on two mirrors where they are deviated first by an angle d and then by an angle $-d+q_s/2$. In this way the two fractions have the same path lengths and they converge onto each other with the desired angle q_s. The sample will be positioned in this interaction region that, in the proposed setup, will be at different locations in the laboratory for different values of q_s.

One must then manipulate the probe beam in such a way as to produce the desired time delay and to converge into the interaction region with the correct Bragg angle, which is equal to the incidence angle of one of the two pump beams while the Bragg scattered beam is collinear with the transmitted part of the other beam; this a consequence of the fact that the wavelength of probe and pump beams are equal. Again, a small out-of-plane excursion of the probe beam from the excitation beams or the use of a different probe wavelength (for example, the FEL third harmonic) is required to circumvent this problem and achieve a spatial separation of the signal.

C. Operations and instrumentation needs

The proposed experiments will typically require monochromatic radiation (e.g., using a diamond (111) reflection) to provide adequate temporal coherence. Energy tunability will help in minimizing the sample heat load, as will operation at highest possible energies (e.g., using the third harmonic). The split-pulse techniques will require either a pulse-splitter optical element, or alternatively, the ability to provide two pulses with variable delay from the source. An x-ray sensitive streak camera with appropriate time resolution will be needed to set up and monitor the split pulses. An x-ray sensitive CCD camera with high spatial resolution, and read-out time commensurate with the source repetition rate, will be required for the time-averaged and split-pulse techniques. Sufficient room in the experimental area for a long distance (10-100 m) between the sample and detector will be beneficial.

D. R&D in support of construction

Several components of the required instrumentation will require R&D effort to assemble and test new systems and possibly extend the current state of the art. These include the monochromator, CCD camera, pulse splitter, and streak camera. It will also be important to carry out tests of the principles of the proposed split-pulse, contrast-analysis technique, and the transient-grating technique, using existing third-generation sources. Work is currently underway to develop direct illumination CCDs that work at TV frame rates (~60 Hz). There is also a large world-wide program to develop pixel array detectors using thin-film technologies. Useful prototypes of these detectors will soon be available; they will have similar spatial resolutions as a CCD but higher quantum efficiencies and faster readout times.

E. Requirements for a future fourth-generation source

For experiments in need of time-averaged brilliance, e.g., standard XPCS, a pulse structure that spreads the intensity into many weaker pulses over a time scale larger than the thermal conduction time constant (e.g., 10 μsec) would alleviate the limitation due to adiabatic sample heating.

V. REFERENCES

[1] See, e.g., G. Gruebel and G.B. Stephenson, in Proceedings of the 4th Generation Light Source Workshop, Advanced Photon Source, Argonne National Laboratory, 10/27-29/97, and references therein.

[2] S. Dierker, *NSLS Newsletter*, July 1995, Brookhaven National Lab.

[3] See, e.g., L.B. Lurio *et al.*, Phys. Rev. Lett. **84**, 785 (2000) and references therein.

[4] See, e.g., A.R. Sandy *et al.*, J. Synchrotron Rad. **6**, 1174 (1999) and references therein.

[5] P.G. de Gennes, J. Chem. Phys. **55**, 572 (1971).

[6] T. Perkins, D.E. Smith, and S. Chu, Science **264**, 819 (1994).

[7] J. Kas, H. Strey, and E. Sackmann, Nature **368**, 226 (1994).
[8] A.N. Semenov *et al.*, Macromolecules **30**, 6280 (1997).
[9] J. Klein, Nature **271**, 143 (1979).
[10] T.P. Russell *et al.*, Nature **365**, 235 (1993).
[11] P. Schleger *et al.*, Phys. Rev. Lett. **81**, 124 (1998).
[12] P. Pincus, J. Chem. Phys. **75**, 1996 (1981).
[13] G.H. Fredrickson and F. S. Bates, J. Chem. Phys. **85**, 633 (1986).
[14] W. Gotze and L. Sjogren, Rep. Prog. Phys. **55**, 241-376 (1992).
[15] R. Bergman *et al.*, Phys. Rev. B. **56**, 11619 (1997).
[16] M. Grimsditch and L.M. Torell, in *Dynamics of Disordered Materials*, ed. D. Richter *et al.*, (Springer, Berlin 1989).
[17] M. Russina *et al.*, Phys. Rev. Lett. **84**, 3620 (2000).
[18] U. Buchenau *et al.*, Phys. Rev. Lett. **77**, 4035 (1996).
[19] C. Masciovechio *et al.*, Phys. Rev. Lett. **80**, 544 (1998).
[20] R. Bruning and M. Sutton, Phys. Rev. B **49**, 3124 (1994).
[21] A.K. Hassan *et al.*, Phys. Rev. B **45**, 12797 (1992).
[22] D. Engberg *et al.*, Phys. Rev. B **59**, 4053 (1999).
[23] Y.-X. Yan and K. A. Nelson, J. Chem. Phys. **87**, 6240 (1987).

X-ray Laser Physics

J. B. Hastings, *Brookhaven National Laboratory, Upton, NY, USA*
J. Arthur, *Stanford Linear Accelerator Center, Stanford, CA, USA*
P. Emma, *Stanford Linear Accelerator Center, Stanford, CA, USA*
A. Freund, *European Synchrotron Radiation Facility, Grenoble, France*
D. Mills, *Argonne National Laboratory, Argonne, IL, USA*
C. Pellegrini, *University of California, Los Angeles, CA, USA*
D. Peter Siddons, *Brookhaven National Laboratory, Upton, NY, USA*
R. Tatchyn, *Stanford Linear Accelerator Center, Stanford, CA, USA*
A. Toor, *Lawrence Livermore National Laboratory, Livermore, CA, USA*
L.-H. Yu, *Brookhaven National Laboratory, Upton, NY, USA*

I. SUMMARY

The Linac Coherent Light Source (LCLS) is a free electron laser (FEL) designed to produce self-amplified spontaneous emission (SASE) at 1.5 Å, with a pulse length of approximately 230 fs, a peak power of about 10 GW, and full transverse coherence. However, even if the LCLS surpasses third-generation sources by 10 orders of magnitude in peak brightness, it will still not have attained its ultimate capabilities. In fact, the LCLS can be considered as a first step toward a new class of electromagnetic radiation sources, similar to the evolution of the first generation of storage-ring-based synchrotron radiation (SR) sources. For example, we have already begun to study the production of significantly shorter pulses approaching 10 fs, a pulse that is transform limited, and optical systems to focus the radiation to spot sizes approaching 10 nm. To achieve these features and to provide the x-ray optics that preserve these properties are the goals of the proposed experimental program. The experiments will be based on manipulation of both the electron beam and x-ray optical techniques to achieve short pulses. Seeding the FEL with cascaded harmonic generation will be used to produce a transform-limited pulse that might also be of approximately 10 fs duration. A two stage FEL with an inserted monochromator also produces a transform-limited pulse, but with 230 fs duration. Efforts toward producing focal spot sizes of order 10 nm will be based on x-ray optical techniques that are beyond the state of the art today. If successful, these results will qualitatively expand the scientific breadth of the LCLS program and form the design basis of future generations of x-ray FEL user sources in the angstrom region.

II. INTRODUCTION

The significant theoretical and experimental advances in FEL physics, high-brightness electron sources, and accelerator technology over the last several years have made a single-pass FEL in the angstrom regime a real possibility. The calculated performance of such a machine shows that both the average and peak brilliance far exceed the corresponding values from the third-generation storage rings.

The radiation field of the SASE output of the LCLS baseline design provides unique scientific opportunities due to the very short pulse length of 230 fs that results from the length of the

electron bunch. This time corresponds to times for atomic motions of heavier atoms and other processes on the atomic scale. However, to access the broadest range of phenomena that are of current interest, it will be critical to reduce the pulse length from 230 fs toward 10 fs, times accessible today with short-pulse lasers operating in the visible/near infrared.

In fact we obtain fs-long spikes in the output from an FEL because the gain bandwidth of this system is large, and the pulse length limit corresponding to the gain bandwidth is as short as 0.9 fs [1]. The corresponding bandwidth in this case for the LCLS is about $5x10^{-4}$.

This same fact determines the temporal shape and the associated line width of the radiation from the SASE FEL. This is a consequence of the SASE process. Starting from spontaneous SR, all frequencies within the bandwidth are excited, so that the resulting amplified radiation consists of independent wave packets (or spikes) in time. These spikes can be shorter than the radiation pulse (bunch length) and their respective phases are random. In the case of the LCLS, there are 250 spikes in a 230-fs-long pulse. While this is not a problem for most experiments that will simply average the intensity over the pulse length, it leads to a line width about 100 times larger than the transform limit. Thus, improvements in the longitudinal coherence of the FEL radiation field are important for the experiments that for example require narrow line-widths.

The peak field provided by the SASE FEL can reach values that are unprecedented in this wavelength range. The radiation output of the individual spikes is fully coherent in the transverse direction and thus in principle can be focused to the diffraction limit. X-ray optics today can provide 100 nm spots in the soft x-ray region of the spectrum and have achieved spot sizes of order 200 nm or slightly smaller in the angstrom regime on the most modern storage ring sources. Development of x-ray optics that provide focal spots approaching the diffraction limit will open uncharted scientific opportunities.

III. SCIENTIFIC OBJECTIVES

A. Focusing of LCLS pulses

A singularly important phase-space transformation of LCLS pulses is ordinary demagnification, or focusing. This follows from the numerous applications and opportunities for new experimental x-ray science made possible by field strengths in the $\sim 10^{10}$-10^{16} V/m range [2,3]. However, realization of the theoretical promise of focusing fully transversely coherent light to a diffraction-limited waist is, in the case of the LCLS, not trivial. As has been noted in prior literature [4], the unique temporal, spectral, and transverse phase space properties of LCLS radiation can strongly influence the performance of conventional optical elements and instruments, and must be rigorously accounted for even in an operation usually as straightforward as focusing.

Issues of particular concern to the effective focusing of LCLS pulses include short-pulse effects, peak power damage effects, and the design, fabrication, and performance of high-quality optical elements in the x-ray range. For example, it can be shown that transmissive (viz., refractive or diffractive) focusing optics rapidly lose effectiveness at focal lengths approaching the diameter of the LCLS pulses, resulting in the necessary utilization of reflecting optics for applications requiring extreme demagnification [5]. The peak power damage issue can be addressed in a number of diverse ways, ranging from the use of multiphase optical media to mitigate damage effects to the use of translatable (e.g., disposable, or single shot) optics where damage is unavoidable. The issue of high-quality optics fabrication for the LCLS is similar in scope to that of x-ray optics utilized on many present-day storage rings, but is complicated by the peak power

damage limitation, as well as the obvious motivation to extend performance limits to take full advantage of the remarkable properties of a fully transversely coherent x-ray source,

To pursue the development of effective focusing strategies for the LCLS, we propose investigations in four areas of R&D critical to reflective, diffractive, and refractive focusing. These are: 1) Improvements in the fabrication of x-ray phase zone plates that have already achieved focusing of order 100 nm [6]; 2) the development of economical, high-quality concave aspherical reflecting surfaces [7]; 3) the development of techniques for high-quality, thin-film and multilayer deposition on aspherical surfaces [8]; 4) the development of techniques for high-quality, large-N (i.e., layer-pair) multilayer deposition followed by transverse slicing and shaping to produce transmissive/diffractive optics [9]; 5) the development of inexpensive solid refractive lenses [10]; and 6) the development of gas, liquid [11], or plasma [12] refractive lenses.

B. Short-pulse generation

The baseline LCLS design provides an x-ray pulse of 230 fs, which is two orders of magnitude shorter than those of third-generation storage ring sources. This qualitative improvement in pulse duration provides for unique opportunities in a breadth of scientific disciplines. Still, this unprecedented x-ray pulse length is more than a factor of twenty longer than the short-pulse optical laser available today. Thus, there is a real desire to match this pulse duration with the LCLS, permitting the use of x-rays as a structural probe with atomic resolution on the same time scale.

The primary purpose of the electron bunch compression system in the LCLS is to increase the bunch current so that SASE conditions are achieved. This increase in peak current is accomplished by reducing the electron bunch length from the 10 ps at the gun, down to 230 fs (FWHM) at the exit of the second bunch compressor. The resulting shorter x-ray pulse has the additional benefits of being brighter and more useful for scientific experiments. The possibility of reducing the electron and/or the x-ray pulse length below the 230 fs value chosen in the LCLS design study has been explored as part of the ongoing LCLS R&D phase. It is understood that achieving the reference value presents a considerable challenge, and that the planned initial experiments will have to be compatible with the nominal LCLS design parameters.

In the reference design, the bunch is compressed with a two-stage bunch compression system using magnetic chicanes. Bunch compression is achieved by establishing an energy-position correlation within the bunch and transporting this beam through a bend system (e.g., chicane) with an inherent energy-dependent path length. The first bunch compressor, using a magnetic chicane at 250 MeV, shortens the bunch from 0.7 to 0.3 mm (rms). The second compressor, using a double magnetic chicane design at 4.54 GeV, compresses the bunch to its final nominal rms value of 24 μm (230 fs FWHM). The rationale for the choice of two compressors and the choice of parameters is contained in the LCLS design report. The reference pulse length of 230 fs is derived from the need to obtain peak currents greater than 3.4 kA needed for the SASE FEL process to saturate, given the expected emittance, momentum spread, and undulator length.

The means available to generate photon pulses shorter than the reference design without increased hardware are:

- Stronger magnetic compression of the electron bunch;
- Longitudinal chirping of the electron bunch followed by optical slicing of the photon bunch;
- Longitudinal chirping of the electron bunch followed by optical compression of the photon bunch;

- A combination of the above three methods.

The stronger compression of the electron bunch is achieved by increasing the momentum spread along the bunch, increasing the strength of the magnetic field of the compressors, or a combination of the two. Although conceptually simple, the task is in fact a difficult one, mostly because of the effect of the emission of coherent synchrotron radiation (CSR) that becomes more severe as the bunch gets shorter. On the positive side, it appears that the nominal LCLS design has the flexibility and tuning range to test ideas and conduct the experiments proposed.

Optical compression of the photon bunch is obtained by increasing the longitudinal momentum spread of the electron beam, thereby dispersing the photon beam in energy and providing the basis for recombining sequential subintervals of the photon pulse into a shorter time interval. Similarly to what is done with the electron bunch, this method exploits a difference in the path length, this time of the photons. A very short FEL pulse can also conceptually be achieved by slicing the pulse. It is suggested to do this by spatially dispersing the photon beam energies and letting a small part of the pulse through an energy-selective optic.

No significant modifications to the LCLS design, such as starting with even shorter bunches from the rf photoinjector, are considered. It also appears feasible to mistune the bunch compression so that only a small part of the electron bunch has sufficient phase space density to lase, but this is not considered a reliable technique because the stability of such a method is not well understood.

1. Electron beam manipulations: Possible scenarios for a shorter x-ray pulse

Two scenarios to produce a shorter x-ray pulse are described here. For both cases the compression parameters of the accelerator need to be adjusted. This is done in an operational sense, such that no re-design is required. Only magnet power supplies, gun charge, and rf phases and amplitudes are adjusted.

a. An extremely short electron bunch

It might be possible to adjust the second compressor chicane magnets to a slightly stronger setting in order to fully compress the electron bunch. This is an extreme case where the bunch reaches a full width of just 10 fs while the final energy spread is still just 0.07%. Figure 1 shows the longitudinal phase space in this case, where the gun charge has also been reduced to 0.2 nC.

This case generates an extremely short bunch in the second bunch compressor chicane, and it may be extremely difficult to preserve the transverse phase space density against the effects of CSR. To mitigate these effects, the total bunch charge in this case has been reduced from 1.0 nC to 0.2 nC, and the compression parameters have been reoptimized. The calculations of the CSR effects are extremely subtle in this case and there is presently very limited confidence that, for this extremely short bunch, the effects can be reliably calculated at present. Note the bunch length at the gun is assumed to be significantly shorter due to the low charge. It is difficult to "back-off" on the compression to produce a bunch length of 50 fs, because the bunch continues to display a very narrow, high peak-current area at the head of the distribution (left) in all cases with a total bunch length of <100 fs.

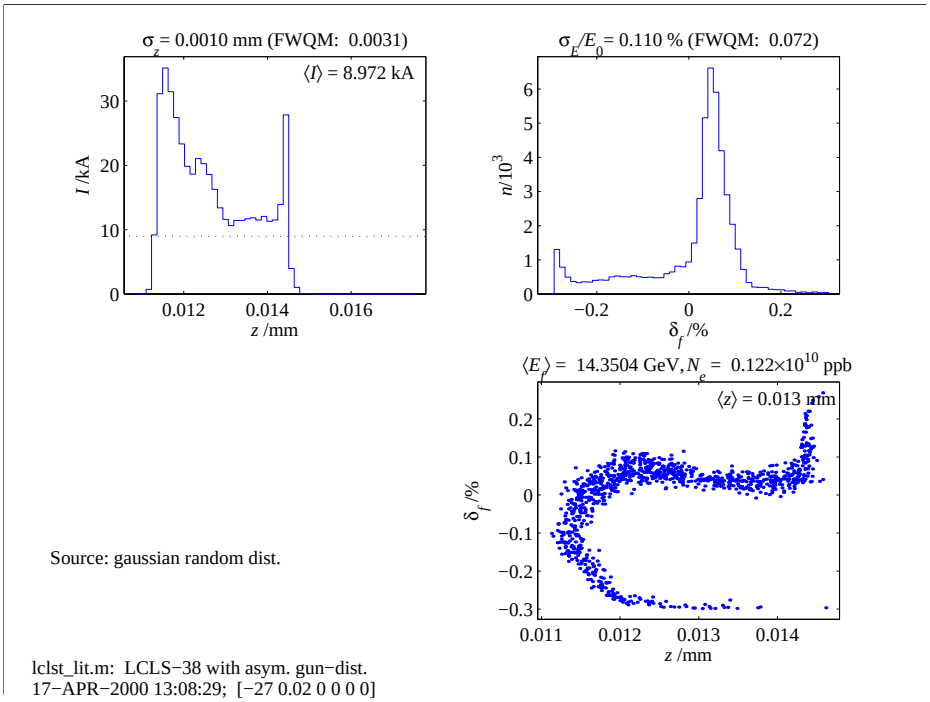

FIG. 1. Case-1: An extremely short electron bunch length produced by a lower bunch charge from the gun and by re-tuning some of the compression parameters.

b. An energy chirp with no change in final e– bunch length

This case considers the possibility of achieving a much larger final correlated energy spread. Excluding a complete re-design of the compression systems, there is only one possibility: "over-compression." Ignoring the emittance growth effects described above, over-compression of the LCLS bunch in the second bunch compressor (BC2) is quite easy. If the nominal BC2 chicane dipole fields are simply increased 9.5%, the bunch will over-compress with a final negative <zδ> correlation immediately after the chicanes. This arrangement produces the same bunch length as does under-compression, yet with a negative <zδ> correlation. The acceleration in the L3-linac to 14 GeV will now generate nearly the same wakefield as before, which will now *add*, rather than cancel, the net <zδ> correlation, making it even more negative. Figure 2 shows the same plots as in Fig. 1, but now calculated for the case of over-compression. In this case, the full-width energy spread is 2% at 14.3 GeV and has a negative, and nearly linear, <zδ> correlation. The rms bunch length is the nominal value of 24 μm. The bunch charge remains at 1 nC. This figure shows that the leading electrons (the bunch head at $z < 0$) are now at higher energy than the trailing electrons. This correlation should generate an accompanying optical chirp that might be used to compress the x-ray pulse to below 50 fs. This level of chirp (~2% FWHM) cannot be generated with a positive <zδ> correlation (i.e., using under-compression).

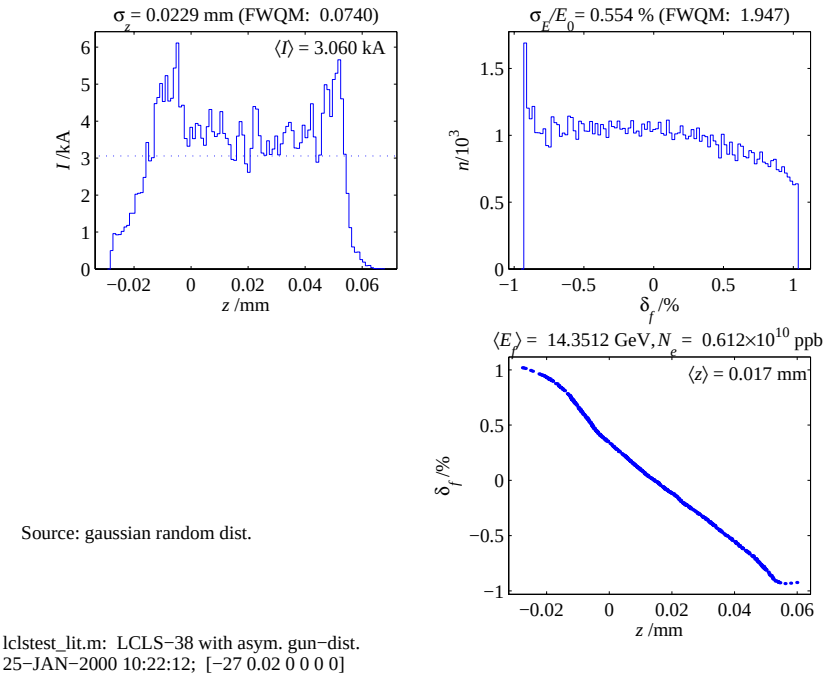

FIG. 2. Same plots as Fig. 1 (at 14 GeV, after the L3-linac and just prior to the undulator), but shown for over-compression. The negative chirp has a full-width energy spread of 2% (bunch-head energy higher than tail) and the rms bunch length, after the DL2-bend system, is 23 μm.

2. Optical techniques using the chirped pulse

a. Pulse slicing

The chirped electron bunch creates a chirped photon pulse. The chirp produced in the photon beam is appropriate for pulse compression concepts where the leading part of the pulse has a higher energy than the trailing part. Most compression schemes using x-ray optics involve dispersive elements and they naturally lead to longer path lengths for lower photon energies.

The chirped photon pulse also affords the opportunity to slice the pulse in energy and thus in time. This is conceptually simple and more easily implemented compared with pulse compression. It requires an x-ray monochromator with a bandpass significantly less than the width of the chirp (2%).

Even in the limit as the resolution approaches zero, the pulse duration remains finite. Thus, the optimal choice of monochromator bandpass is just that corresponding to the zero bandwidth pulse duration, 6 fs.

The best understood x-ray optical components are perfect crystals of which Si is the best example. In general, the dynamical theory of x-ray diffraction exactly describes the performance of perfect crystal Si x-ray optics. Based on this, a myriad of novel x-ray optical components have been fabricated over the last 35 years. One of these designed for use at storage rings is a monolithic two-crystal monochromator where the crystals have been cut asymmetrically (the crystal surfaces are not parallel to the Bragg planes) [13]. The asymmetric cut increases the energy acceptance of the monochromator beyond the value for symmetric Bragg reflection. By adjusting the asymmetry, one can tune the acceptance of, for example, the Si(111) reflection to match that needed to slice the chirped x-ray pulse, yielding a pulse duration of 9 fs.

An alternative to perfect crystal optics is the use of artificial crystals, in particular multilayers. Reflection off a multilayer represents an efficient and flexible means for slicing out a short sub-interval of a longitudinally chirped LCLS radiation pulse [14]. The technique is equivalent to placing an energy aperture into the longitudinal phase space of the radiation. In this regard it operates in the same phase-space domain in which the photon beam is chirped and involves no coupling to either of the transverse phase-space dimensions.

A second advantage is the flexible control of the efficiency, bandwidth, and band shape of the multilayer reflectivity, which, based on theoretical calculations and the presumed continuing development of present-day technological capabilities [15,16], would allow the attainment of sliced pulse lengths of < 10 fs at reflection efficiencies of $> 50\%$.

The development of reliable multilayer pulse slicing optics is expected to be critical to the extension and definition of the scientific capabilities of the LCLS. This is predicated on the central role that the generation of ultrashort pulses is expected to assume in a number of the frontier experiments and applications being proposed for present-day and future generations of SR light sources, including the LCLS [17,18,19]. Two noteworthy examples of such applications are: 1) single-shot imaging of single biological molecules or small molecular clusters; and 2) the study of ultrafast chemical processes. In ongoing design studies of the LCLS x-ray optics and beamline systems, it has consequently been assumed that beamlines fed by reflective multilayer optics — dedicated to ultrashort pulse generation — will feature prominently in the overall R&D capabilities of the LCLS facility.

Raising multilayer deposition technology and optics to the level of reliability and precision required for LCLS applications will involve both theoretical and experimental R&D in a number of critical areas. First, the dynamical theory of multilayer response to LCLS radiation has to be developed to allow the reliable simulation of multilayer response to ultrashort, ultraintense x-ray radiation pulses [20]. Valid models of this interaction first need to be rounded out and completed for the weak-field (linear) regime, and then extended to describe the self-consistent propagation of radiation in the nonlinear domain, encompassing effects such as, e.g., the real-time modulation of optical and lattice constants by the propagating field [21]. Second, the investigation and development of multilayer deposition processes and material systems needs to be extended to researching ultrastable systems (e.g., the disilicides) featuring minimal interfacial roughness and maximal resistance to peak-power radiation damage [22]. Third, multilayers designed and prepared using algorithms and techniques developed in the theoretical and fabrication R&D phases need to be tested for performance over the range of field strengths (weak through nonlinear) anticipated for the LCLS. The major (weak-field) fraction of this R&D phase can be carried out at conventional third-generation storage ring SR sources [23]. Tests at field strengths approaching or exceeding the fields in the raw LCLS beam will require developing ultrastrong x-ray focusing optics and implementing them either on suitable third-generation SR storage ring beamlines, or on special linac-based sources optimized for approximating the parameter space of the LCLS [24,25].

b. Pulse compression

As outlined above, optical pulse compression can be achieved by dispersing successive intervals of a chirped photon pulse along trajectories of different lengths and recombining them within a common space-time volume. A number of schemes have been considered by the LCLS X-Ray Optics R&D Group and other collaborators [26,27], all of which require a minimum of two dispersive elements constituted of, for example, gratings, multilayers, or crystals. Due to the

greater complexity and demands for higher optical efficiency that these schemes require, the necessary R&D will entail further numerical and theoretical studies, coupled to the design, fabrication, and testing of novel high-performance optical components and systems.

C. Production of transform-limited beams

1. Introduction.

Two methods have been proposed and studied to reduce the line width of a SASE-FEL and/or produce transform-limited pulses. One is based on seeding the FEL with a narrow linewidth (transform limited) laser signal at wavelengths longer than x-rays, and then using several stages of harmonic generation to reach 1 Å. The other, referred to as a two-stage FEL, is based on two undulators. The first undulator operates as a SASE-FEL amplifier. It is followed by a monochromator to select a pulse with the desired bandwidth, and this pulse is the seed for the second undulator, similar to one stage of the cascaded harmonic generation. To reduce the large intensity fluctuations at the exit of the monochromator, the second undulator is longer than the saturation length.

2. Coherent hard x-ray production by cascading stages of high-gain harmonic generation

The LCLS baseline design, based on SASE, produces x-rays in the angstrom region, but the radiation does not have full longitudinal coherence. In contrast to this, a recent high-gain harmonic generation (HGHG) proof of principle experiment [28] has demonstrated the possibility of using the HGHG scheme to produce a fully coherent FEL beam. This stimulates our interest in designing an HGHG-based x-ray FEL in the angstrom region.

In the simplest two-undulator HGHG scheme, a coherent seed at a wavelength at a subharmonic of the desired output wavelength interacts with the electron beam in an energy-modulating section (undulator). This energy modulation is then converted into spatial bunching while traversing a dispersive section (a three-dipole chicane). In the second undulator (radiator), which is tuned to a higher harmonic of the seed radiation, the microbunched electron beam first emits coherent radiation and then amplifies it exponentially until saturation is achieved.

Given a commercially available seed laser and the quality of the electron beam, it is not possible to get x-rays with wavelengths of order 1 Å using just two undulators, so some modifications are needed.

i.) We need multiple stages. Each stage converts a longer wavelength to its n^{th} harmonic. In practice, n cannot be too large. In the proposed design we use n = 3, 4, and 5.

ii.) Conceptually the device is composed of two parts, a converter and an amplifier. The converter consists of several stages, which convert the seed light to the design wavelength step by step. Then the amplifier exponentially amplifies the light from the last stage to saturation.

iii.) Except for the amplifier, each stage only converts the light to its n^{th} harmonic and does not operate in the exponential growth regime. Rather it will be the negative gain regime for the modulator in each stage as long as the energy modulation is produced. It will be the coherent radiation regime for the radiator in each stage as long as enough power is produced for modulating the electron beam in the next stage.

iv.) Since the energy of the electron beam should match the corresponding radiation wavelength, we would like to optimize the energy of the electron beam for each stage. That would mean that each stage would use a different beam energy. In reality we are limited by the available electron beam parameters in our design, so only two electron beams are used. One, with lower energy (4.5 GeV), works in the longer wavelength stages and one, with E=14.3 GeV, works in the shorter wavelength stages.

Since we need several stages of HGHG, we need extra components compared with the proof-of-principle experiment [28]. Each stage will consist of one modulator, a dispersion section, and a radiator. The physical process in each stage will be the same as the previous experiment. During the process at each stage, the output laser has disturbed the part of the e-beam that is coincident with it, so in order to achieve the best efficiency, we would like to either shift the laser to a fresh part of the same e-beam or introduce another e-beam for each stage, so that again the laser will interact with a "fresh" bunch, the so-called "fresh bunch technique" [29].

Let us now look at the whole device. We begin with a commercially available laser with a wavelength of 2250 Å and a peak power of P_{in}=180 MW. The converter of the system is separated into two parts. The first part uses an electron beam of 4.5 GeV with two HGHG stages. In the first stage, the 2250 Å light, with a pulse length of order 10 fs, is introduced into the modulator, which is followed by the first dispersive section converting the energy modulation into a spatial modulation. This is in turn followed by the first radiator operating at the fifth harmonic, i.e., 450 Å. This is the seed beam for the second stage. To get a fresh bunch, the fresh bunch technique is used to shift the seed beam with respect to the electron bunch so that a fresh part of the bunch is modulated with the 450 Å seed. Then the same process is repeated in the second stage, which also operates on the fifth harmonic, producing 90 Å at the output of the second radiator. The first part of the system, based on the 4.5 GeV pulse, is now complete.

The 90 Å seed starts the short-wavelength section operating at the full LCLS energy, 14.3 GeV. In the second converter system, there are three HGHG stages that go from 90 Å to 18 Å, then to 4.5 Å, and finally to 1.5 Å. The last element is the amplifier to amplify the 1.5 Å radiation to saturation, about 12 GW.

3. A two-stage FEL

The two-stage FEL scheme [30] uses only one electron bunch. It produces a transform-limited pulse corresponding to the electron beam bunch length. The first stage produces the seed pulse for the second stage. It is thus similar to the HGHG scheme, but simpler in concept and with reduced capabilities. The seed pulse for the second undulator of this method is produced using a monchromator with a resolution slightly narrower than the transform limit of the electron beam placed at the exit of the first undulator, which is a few gain lengths long. Since we select a line width smaller than that of a single spike, the intensity fluctuations at the monochromator exit are as large as 100%. To reduce these fluctuations at the exit of the second undulator, it is longer than that required for SASE-FEL saturation.

4. Scope of LCLS studies for production of transform-limited pulses.

Both ideas discussed above, HGHG and a two-stage FEL, need extensive study and hardware to be carried out. Much of this may be beyond the scope of the initial R&D phase of the LCLS project. However, the LCLS has unique capabilities that can be used, for example, to generate the two electron bunches, one at 4.5 GeV and one at 14 GeV, with the necessary peak current

and emittance that would be required for the cascaded HGHG proposal. Demonstration of these beam properties and beam timing is possible within the LCLS scope. For the two-stage FEL, many aspects can be studied and, since this idea has less ambitious needs, it may be possible to test it completely by proper planning of the undulator design within the LCLS project.

IV. REFERENCES

[1] R. Bonifacio *et al*., Phys. Rev. Lett. **73**, 70 (1994).

[2] S.K. Sinha, AIP Conference Proceedings **521**, 435 (2000).

[3] P. Chen, C. Pellegrini, *Mini-Workshop on High Field, High Intensity Physics with Linac Coherent Light Source (LCLS)*, SLAC, Stanford, CA, July 13, 2000.

[4] R. Tatchyn, J. Arthur, R. Boyce, T. Cremer, A. Fasso, J. Montgomery, V. Vylet, D. Walz, R. Yotam, A.K. Freund, and M.R. Howells, SPIE Proceedings **3154**, 174 (1998).

[5] R. Tatchyn, AIP Conference Proceedings **521**, 471 (2000).

[6] J. Thieme, G. Schmahl, D. Rudolph, and E. Umbach, eds., *Status Report from the 5th International Conference on X-ray Microscopy and Spectromicroscopy*, Wurzburg, August 19-23, 1996, (Springer Verlag, Berlin, 1998).

[7] H. Kinoshita *et al*., SPIE Proceedings **3767**, 164 (1999).

[8] R. Stommer *et al*., Nuovo Cimento D **19**, 465 (1997).

[9] R.M. Bionta, Appl. Phys. Lett. **51**, 725 (1987).

[10] H.R. Beguiristain, M.A. Piestrup, R.H. Pantell, C.K. Gary, J.T. Cremer, and R. Tatchyn, AIP Conference Proceedings **521**, 471 (2000).

[11] R. Tatchyn, in *Proceedings of the Workshop on Scientific Applications of Short Wavelength Coherent Light Sources*, SLAC Report 414; SLAC-PUB 6064, March 1993.

[12] S. Shlyaptsev, in "Workshop on Methods and Instrumentation for X-FEL," DESY, Hamburg, June 26-27, 2000,

[13] K. Kohra *et al*, Nucl. Instrum. Methods **152**, 161 (1978).

[14] R. Tatchyn, in "Workshop on Methods and Instrumentation for X-FEL," DESY, Hamburg, June 26-27, 2000,

[15] D. Boyers, A. Ho, Q. Li , M. Piestrup, M. Rice, and R. Tatchyn, Nucl Instrum. Methods A **346,** 565(1994).

[16] E. Ziegler *et al* SPIE Proceedings **3737**, 386 (1999).

[17] B.H. Wiik *et al* International Workshop on "X-ray Free Electron Laser Applications," (Copies of Transparencies), Sept. 16-17, 1996, DESY, Hamburg, Germany.

[18] I. Lindau and J. Arthur, eds., *Workshop on Scientific Applications of the LCLS*, SLAC, Stanford, CA, October 15-16, 1999.

[19] S.K. Sinha, AIP Conference Proceedings **521**, 435 (2000).

[20] R. Tatchyn, G. Materlik, A. Freund, and J. Arthur, eds., *Proceedings of the SLAC/DESY International Workshop on the Interactions of Intense Sub-Picosecond X-ray Pulses with Matter*, SLAC, Stanford, CA, Jan. 23-24, 1997, SLAC WP-12.

[21] R. Tatchyn, J. Arthur, R. Boyce, T. Cremer, A. Fasso, J. Montgomery, V. Vylet, D. Walz, R. Yotam, A. K. Freund, and M.R. Howells, SPIE Proceedings 3154, **174**(1998).

[22] A. Alberti *et al* J. Vac. Sci. Tech. B **17** (4), 1448(1999).

[23] For example, the APS, the ESRF, SPring-8.

[24] R. Tatchyn, in "Workshop on Methods and Instrumentation for X-FEL," DESY, Hamburg, June 26-27, 2000.

[25] P. Emma and J. Frisch, "Femtosecond x-ray generation in the SLC arc reverse bend," internal SLAC memo, 1999-2000.

[26] V. Bharadwaj, A. Chao, M. Cornacchia, P. Emma, T. Kotseroglou, P. Krejcik, I. Lindau, H.D. Nuhn, G. Stupakov, R. Tatchyn, R. Bionta, A. Toor, and C. Pellegrini, LCLS-TN-00-8.

[27] A.K. Freund, in *Proceedings of the SLAC/DESY International Workshop on the Interactions of Intense Sub-Picosecond X-Ray Pulses with Matter*, R. Tatchyn, G. Materlik, A. Freund, J. Arthur, eds., SLAC, Stanford, CA, Jan. 23-24, 1997, SLAC WP-12.

[28] L.-H. Yu *et al*., Nucl. Instrum. Methods A **445**, 301(1999).

[29] I. Ben-Zvi, K. M. Yang, and L.-H. Yu, Nucl. Instrum. Methods A **318**, 726(1992).

[30] J. Feldhaus *et al*., Optics Comm. **140**, 341 (1997).

Appendix I: Committee Members

Members of the LCLS Scientific Advisory Committee (SAC)

Phil Bucksbaum	Univ. of Michigan
Roger Falcone	Univ. of California, Berkeley
Rick Freeman	Univ. of California, Davis
Andreas Freund	European Synchrotron Radiation Facility
Janos Hajdu	Uppsala Univ.
Jerry Hastings	National Synchrotron Light Source
Richard Lee	Lawrence Livermore National Laboratory
Ingolf Lindau	Stanford Synchrotron Radiation Laboratory
Gerd Materlik	HASYLAB
Simon Mochrie	Univ. of Chicago
Keith Nelson	Massachusetts Institute of Technology
Francesco Sette	European Synchrotron Radiation Facility
Sunil Sinha	Advanced Photon Source
Brian Stephenson	Argonne National Laboratory
Z.X. Shen	Stanford Univ.
Gopal Shenoy	**Advanced Photon Source (Co-Chairman)**
Joachim Stöhr	**Stanford Synchrotron Radiation Laboratory (Chairman)**

Members of the LCLS Technical Advisory Committee (TAC)

Bill Colson	**Naval Postgraduate School (Chairman)**
Dave Attwood	Lawrence Berkeley National Laboratory
Jerry Hastings	National Synchrotron Light Source
Pat O' Shea	Univ. of Maryland
Ross Schlueter	Lawrence Berkeley National Laboratory
Ron Ruth	Stanford Linear Accelerator Center